

---

# Quantitative cell assays and reduction of cell-to-cell variability in defined microenvironments

Alicia Piera Alberola

---



München 2010



---

# Quantitative cell assays and reduction of cell-to-cell variability in defined microenvironments

Alicia Piera Alberola

---

Dissertation  
an der Fakultät für Physik  
der Ludwig-Maximilians-Universität  
München

vorgelegt von  
Alicia Piera Alberola  
aus Jerez de la Frontera

München, November 2010

Erstgutachter: Joachim O.Rädler

Zweitgutachter: Erwin Frey

Tag der mündlichen Prüfung: 21. Januar 2011

“Imagination is more important than knowledge”

Albert Einstein



# Contents

|  |             |
|--|-------------|
| <b>List of Figures</b>   | <b>xi</b>   |
| <b>Zusammenfassung</b>   | <b>xiii</b> |
| <b>Summary</b>   | <b>xv</b>   |
| <b>1 Introduction</b>  | <b>1</b>    |
| <b>2 Fundamental concepts</b>  | <b>5</b>    |
| 2.1 Cellular biomechanics . . . . .  | 5           |
| 2.1.1 Cell-substrate adhesion . . . . .  | 6           |
| 2.1.2 Cell-cell adhesion . . . . .   | 8           |
| 2.1.3 Cell shape . . . . .   | 9           |
| 2.1.4 Portals of entry into the cell . . . . .   | 9           |
| 2.1.5 Cell migration . . . . .   | 10          |
| 2.1.6 Cell behavior in tissues . . . . .   | 10          |
| 2.1.7 Epithelial cell polarisation: symmetry breaking . . . . .                                      | 12          |
| 2.2 Physical models of tissues . . . . .   | 13          |
| 2.2.1 Tissue surface tensions: the differential adhesion hypothesis . . . . .                        | 14          |
| 2.2.2 Cell and tissue shape: interplay of cortical tension and cell-cell adhesion . . . . .          | 15          |
| 2.2.3 Vertex models . . . . .  | 16          |
| <b>3 Towards a defined presentation of nanoparticles to cells</b>                                    | <b>17</b>   |
| 3.1 Motivation . . . . .   | 17          |
| 3.2 Introduction . . . . .   | 18          |
| 3.3 The defined presentation of nanoparticles to cells and their surface controlled uptake . . . . . | 20          |
| 3.3.1 Model system . . . . .   | 20          |
| 3.3.2 Preparation of surfaces with a certain amount of well dispersed NPs . . . . .                  | 20          |
| 3.3.3 Visualization of NP internalization . . . . .  | 21          |
| 3.3.4 Quantification . . . . .   | 25          |
| 3.3.5 Surface dependent uptake . . . . .   | 26          |
| 3.3.6 Time dependent uptake: NP exocytosis . . . . .   | 26          |

|          |  |           |
|----------|--|-----------|
| 3.4      | Determining NP internalization routes and end-location by TEM . . . . .    | 27        |
| 3.4.1    | Internalization routes . . . . .   | 27        |
| 3.4.2    | End-location inside cells . . . . .  | 28        |
| 3.5      | Conclusions . . . . .  | 29        |
| 3.6      | Limitations and solutions . . . . .  | 29        |
| <b>4</b> | <b>Surface controlled gene delivery</b>                                    | <b>33</b> |
| 4.1      | Introduction . . . . .   | 33        |
| 4.2      | Results . . . . .  | 35        |
| 4.2.1    | Protocol optimization . . . . .  | 35        |
| 4.2.2    | Surface dependent reverse transfection . . . . .                           | 36        |
| 4.3      | Conclusions . . . . .  | 36        |
| <b>5</b> | <b>Surface patterning techniques</b>                                       | <b>41</b> |
| 5.1      | Microcontact printing . . . . .  | 41        |
| 5.2      | Microscale plasma-initiated patterning . . . . .                           | 42        |
| 5.2.1    | Plasma induced patterning using a TEM grid as a mask . . . . .             | 42        |
| <b>6</b> | <b>Oligocellular arrays: towards defined mechanical states</b>             | <b>45</b> |
| 6.1      | Cells in confinement arrange into stable packing states . . . . .          | 45        |
| 6.2      | Stable packing states . . . . .  | 48        |
| 6.3      | Edge-induced planar polarity . . . . .                                     | 50        |
| 6.4      | Discussion . . . . .   | 53        |
| <b>7</b> | <b>Oligocellular arrays: a novel approach to study cell mechanics</b>      | <b>55</b> |
| 7.1      | Mechanical equilibrium model of cell packing states . . . . .              | 55        |
| 7.2      | Transitions between equivalent stable cell packings . . . . .              | 60        |
| 7.3      | Conclusions . . . . .  | 60        |
| <b>8</b> | <b>Collective cell migration</b>   | <b>63</b> |
| 8.1      | Introduction . . . . .   | 63        |
| 8.1.1    | Collective cell migration . . . . .  | 63        |
| 8.1.2    | Symmetry breaking in collective cell migration . . . . .                   | 64        |
| 8.2      | Results . . . . .  | 64        |
| 8.2.1    | Collective rotation . . . . .  | 64        |
| 8.2.2    | Symmetry breaking events . . . . .   | 68        |
| 8.2.3    | Planar cell polarity, edges and collective movements . . . . .             | 71        |
| 8.3      | Conclusions . . . . .  | 74        |
| <b>9</b> | <b>Cellular self-organisation in single cell arrays</b>                    | <b>75</b> |
| 9.1      | Introduction . . . . .   | 75        |
| 9.2      | Musical chairs: single cell arrays by cellular self-organization . . . . . | 76        |
| 9.3      | Conclusions and outlook . . . . .  | 79        |



---

|   |            |
|---|------------|
| <b>10 Multifunctional spatially controlled patterning</b>                 | <b>81</b>  |
| 10.1 Plasma induced patterning with backfilling . . . . .                 | 81         |
| 10.2 Multifunctional spatially controlled patterning . . . . .            | 83         |
| <b>11 Conclusions and outlook</b>   | <b>87</b>  |
| <b>A Standard procedures</b>  | <b>91</b>  |
| A.1 Cell culture . . . . .  | 91         |
| A.2 Microscopy . . . . .  | 91         |
| A.3 $\mu$ -slide coating . . . . .  | 92         |
| A.4 Cell nuclei staining . . . . .  | 92         |
| A.5 Experiments with NPs . . . . .  | 92         |
| A.5.1 Nanoparticle characterization . . . . .                             | 92         |
| A.5.2 Preparation of surfaces with a certain amount of well dispersed NPs | 92         |
| A.5.3 NP exposure assay . . . . .   | 93         |
| A.5.4 NP surface dependent uptake . . . . .                               | 93         |
| A.5.5 NP time-dependent uptake . . . . .                                  | 93         |
| A.6 Sample preparation for TEM . . . . .                                  | 93         |
| A.7 Patterning Protocols . . . . .  | 94         |
| A.7.1 Plasma initiated patterning . . . . .                               | 94         |
| A.7.2 PDMS stamp preparation . . . . .                                    | 95         |
| A.7.3 Microcontact printing . . . . .                                     | 95         |
| A.7.4 Backfill with Pluronic <sup>®</sup> F-127 . . . . .                 | 95         |
| A.7.5 Plasma induced patterning with PEG-g-PLL backfill . . . . .         | 96         |
| A.7.6 Cell patterning . . . . .   | 96         |
| A.8 Transfection protocols . . . . .                                      | 96         |
| A.8.1 Complex preparation . . . . .                                       | 96         |
| A.8.2 Reverse transfection in $\mu$ -slides . . . . .                     | 96         |
| A.8.3 Transfection efficiency assessment . . . . .                        | 97         |
| <b>B Calculation of cell packing states</b>                               | <b>99</b>  |
| <b>Bibliography</b>   | <b>103</b> |
| <b>Acknowledgments</b>  | <b>111</b> |
| <b>Curriculum Vitae</b>   | <b>112</b> |



# List of Figures

|      |  |    |
|------|--|----|
| 1.1  | Schematic diagram of the work . . . . .  | 2  |
| 1.2  | Ommatidia in the <i>Drosophila</i> retina . . . . .  | 3  |
| 2.1  | Types of epithelial cells. . . . .   | 11 |
| 2.2  | Types of epithelium. . . . .   | 11 |
| 2.3  | Epithelial polarisation . . . . .  | 12 |
| 2.4  | Schematic of PCP protein asymmetric distribution . . . . .   | 14 |
| 2.5  | Differential adhesion hypothesis . . . . .   | 15 |
| 3.1  | Nanoparticle aggregation . . . . .   | 18 |
| 3.2  | Particle characterisation. . . . .   | 21 |
| 3.3  | Schematic representation of the nanoparticle surface preparation . . . . .                                 | 22 |
| 3.4  | Number of absorbed NP per surface area vs. NP solution concentration. . . . .                              | 23 |
| 3.5  | Z-scan fluorescence imaging of NP uptake . . . . .   | 23 |
| 3.6  | Surface controlled nanoparticle uptake. . . . .  | 24 |
| 3.7  | NPs aggregate inside cells . . . . .   | 25 |
| 3.8  | Surface dependent uptake . . . . .   | 27 |
| 3.9  | Time dependent uptake . . . . .  | 28 |
| 3.10 | Diffusion through the cell membrane . . . . .  | 29 |
| 3.11 | Portals of entry into the cell . . . . .   | 30 |
| 3.12 | End-location of NPs inside cells . . . . .   | 31 |
| 4.1  | FuGENE <sup>®</sup> /pEGFP-N1 complex polydispersity and transfection rates are buffer dependent . . . . . | 34 |
| 4.2  | Reverse transfection with l-PEI/pEGFP-N1 complexes . . . . .   | 36 |
| 4.3  | Reverse transfection with FuGENE <sup>®</sup> /pEGFP-N1 and Huh7 cells . . . . .                           | 37 |
| 4.4  | Reverse transfection with l-PEI/pEGFP-N1 and Huh7 cells . . . . .  | 38 |
| 4.5  | Transfection efficiency dependence on surface modification . . . . .                                       | 38 |
| 4.6  | Transfection efficiency dependence on surface modification . . . . .                                       | 39 |
| 5.1  | Microscale plasma induced patterning ( $\mu$ PIP) . . . . .  | 43 |
| 5.2  | Plasma induced patterning using a TEM grid as a mask . . . . .   | 44 |
| 6.1  | Living under confinement . . . . .   | 46 |

|      |   |     |
|------|---|-----|
| 6.2  | Time evolution . . . . .  | 46  |
| 6.3  | Migration between fields . . . . .  | 47  |
| 6.4  | Relative abundance of homeostatic packing states. . . . .   | 49  |
| 6.5  | Distribution of $\delta$ distances between 3-cell junctions. . . . .  | 50  |
| 6.6  | Nuclear position is independent of patch geometry . . . . .   | 51  |
| 6.7  | Nuclear deformation . . . . .   | 51  |
| 6.8  | Edge induced planar cell polarisation . . . . .   | 52  |
| 7.1  | Mechanical model . . . . .  | 57  |
| 7.2  | Cell anisotropy and energy landscapes of cell packing states in the current standard and extended model . . . . . | 58  |
| 7.3  | Transitions between equivalent stable cell packings . . . . .   | 61  |
| 8.1  | Collective rotation . . . . .   | 66  |
| 8.2  | Marginal cells exhibit leader cell characteristics . . . . .  | 66  |
| 8.3  | Time evolution of collective rotation . . . . .   | 67  |
| 8.4  | Rotation velocity depends on the number of cells per adhesive island . . . . .                                    | 68  |
| 8.5  | Single cell actin polymerization on a circular adhesive island . . . . .  | 69  |
| 8.6  | Single cell migrational behavior on a circular adhesive island . . . . .  | 70  |
| 8.7  | Symmetry breaking by confinement . . . . .  | 72  |
| 8.8  | Velocity and planar polarity vector fields in epithelia . . . . .   | 73  |
| 8.9  | Opposite polarizing signals could be responsible for collective rotation . . . . .                                | 73  |
| 9.1  | Single cell array . . . . .   | 76  |
| 9.2  | Self-organisation of cells on a structured PDMS surface . . . . .   | 77  |
| 9.3  | Self-organisation of cells on a fibronectin printed surface with Pluronic <sup>®</sup> /PLL backfill . . . . .    | 78  |
| 10.1 | Microscale plasma induced patterning with Pluronic <sup>®</sup> F-127 backfill . . . . .                          | 82  |
| 10.2 | Microscale plasma induced patterning with PEG-g-PLL backfill . . . . .  | 84  |
| 10.3 | Ternary substrates . . . . .  | 85  |
| 11.1 | Artificially ordered tissue . . . . .   | 88  |
| 11.2 | Structural role of cell-cell and cell-substrate adhesions . . . . .   | 88  |
| B.1  | Calculation of cell packing states for N=2,3 . . . . .  | 101 |
| B.2  | Calculation of cell packing states for N=4 . . . . .  | 102 |

# Zusammenfassung

Im Rahmen der vorliegenden Doktorarbeit wurden strukturierte Zellumgebungen entwickelt, mit welchen es ermöglicht wird, quantitative Versuche mit geringer Variabilität durchzuführen. Im Speziellen wurden die Aufnahme von Partikeln durch Zellen, Genexpression, Zellmechanik und die Migration von Zellverbänden studiert.

Im ersten Teil dieser Doktorarbeit wurde eine neue Methode etabliert, um die Aufnahme von Nanopartikeln (NP) durch Zellen mit höherer Genauigkeit zu untersuchen. Mit dieser Methode können homogene und reproduzierbare Verteilungen von einzelnen Quantenpunkten auf Oberflächen erreicht werden. Im Gegensatz zu anderen Methoden werden die Quantenpunkte auf die Oberfläche aufgebracht, bevor diese mit Zellen inkubiert wird. Da die Oberfläche als natürliche Referenzebene dient, können NP, die von Zellen aufgenommen wurden, dadurch nachgewiesen werden, dass diese NP sich oberhalb dieser befinden müssen. Es ist zu beobachten, dass nach der Anfangsphase des Versuchs, in welcher die NP lediglich aufgenommen werden, die Zellen auch beginnen die NP wieder auszuscheiden. Es entsteht ein Gleichgewicht zwischen beiden Prozessen, sodass die Gesamtanzahl aufgenommener NP ab einem bestimmten Zeitpunkt um einen konstanten Wert fluktuiert. Die Untersuchungen zur Aufnahme der NP zeigen außerdem eine Abhängigkeit dieser von der Beschichtung der Oberfläche. Mit der gleichen Methode wird die Aufnahme von Gentransferkomplexen untersucht.

Im zweiten Teil der Arbeit wurden kleine Gruppen von Epithelzellen studiert, welche in quadratischen Mikrostrukturen eingeschlossen wurden. Es stellt sich heraus, dass die Zellen sich in stabilen Konfigurationen anordnen, die nach Symmetrie und Anzahl der Zellen klassifiziert und statistisch ausgewertet wurden. Die experimentellen Daten wurden mit theoretischen Modellen in Zusammenarbeit mit Karen Alim aus der Gruppe von Erwin Frey, LMU München, verglichen. Es zeigt sich, dass das existierende Modell erweitert werden muss und neben der Kontraktilität des Zellkortex und der interzelluläre Adhäsion auch die Anisotropie der Zellform zu berücksichtigen ist. Eine wichtige Eigenschaft dieser oligozellularen Arrays ist die reduzierte Anzahl an Freiheitsgraden im System, was die Berücksichtigung von sämtlichen vorkommenden Konfigurationen möglich macht.

In einem weiteren Teil wurde die Dynamik von kleinen Zellgruppen in runden adhäsiven Inseln untersucht. Es stellte sich heraus, dass die Zellen in einem bestimmten Zustand übergehen können, in welchem sie sich kollektiv zu drehen beginnen. Die Winkelgeschwindigkeit bleibt dabei konstant und hängt von der Anzahl der Zellen pro Insel ab; je mehr Zellen sich drehen, desto langsamer ist die Geschwindigkeit. Wechsel in der Drehrichtung

wurden dabei nur selten und meist in Zusammenhang mit einer Zellteilung beobachtet. Der Moment indem die Zellen zu rotieren beginnen, stellt dabei einen Symmetriebruch dar. Ein solcher wurde in drei unterschiedlichen Formen beobachtet: die intrinsische Asymmetrie des kortikalen Aktinzytoskeletts, eine kontakt-induzierte Persistenz in Richtung der Zellmigration und Zellpolarität in der Ebene des Epithels. Diese experimentelle Methode ist von großem Vorteil, da die definierten Randbedingungen und die kleine Anzahl an Zellen es erlauben, das Phänomen der kollektiven Zellmigration besser zu studieren.

Oligozellulare Systeme vereinfachen die Anwendung theoretischer Modelle, wobei die daraus gewonnenen Erkenntnisse dennoch auch in komplexeren Systemen ihre Gültigkeit behalten.

Im Weiteren wurde die zelluläre Selbstorganisation in Zellarrays von einzelnen Zellen untersucht. Neu entwickelte, mikrostrukturierte Substrate, wurden erzeugt, auf denen sich Zellen bevorzugt innerhalb adhäsiver Inseln aufhalten aber auch auf der Oberfläche zwischen diesen migrieren können. Die Migrationseigenschaften der Zellen auf solchen Substraten wurde untersucht.

Schließlich wird eine Methode zur Herstellung mikrostrukturierter, multifunktionaler Substrate beschrieben, welche aus drei verschiedenen Oberflächenbeschichtungen bestehen. Zum Beispiel können damit Geometrien erzeugt werden, die verschiedene Oberflächenbeschichtung am Rand und im Inneren aufweisen.

# Summary

Within this thesis, defined cell microenvironments, which enable quantification and reduce experimental variability, have been developed to study particle internalisation, gene expression, cell mechanics and collective cell migration.

In the first part of the thesis, a novel approach to study nanoparticle (NP) internalization is established. For the first time, the problems of NP aggregation and number density fluctuation are circumvented. Homogeneous and reproducible distributions of single quantum dots are achieved by seeding NP onto solid substrates prior to incubation with cell medium and seeding of cells. This approach enables the detection of internalized NPs because the solid surface represents a natural reference frame. NPs that are taken up by the cells are reliably measured as those being lifted above this reference plane. Time-lapse microscopy reveals that after an initial period of time in which only NP internalization takes place, an equilibrium between NPs entering and leaving cells is established and the effective number of internalized nanoparticles fluctuates around a constant value. The relative internalization rates from surfaces precoated with different extra-cellular molecules were assessed revealing the influence of the surface modification on uptake rates. The same approach has been applied to the uptake of gene delivery particles.

In the second part of this thesis, small groups of epithelial cells confined to adhesive islands are studied. It is found that stable cell packing configurations appear in square adhesive islands. The packing states are classified according to number of cells and symmetry, and their frequency of occurrence is measured. In the next chapter, experimental data are compared to theoretical modeling in collaboration with Karen Alim from the group of Erwin Frey, LMU, Munich. Here, oligocellular arrays unravel new contributions to epithelial cell packing and the current vertex model is extended to account for cell shape anisotropy in addition to cell-cortex contractility and cell-cell adhesion. The dynamic of the system is studied by means of time-lapse microscopy. An important feature of oligocellular arrays is that the reduced degrees of freedom of the system allow for the full assessment of the entire configuration space.

Next, the dynamics of small groups of cells in circular adhesive islands is described. It is found that cells can enter states where they collectively rotate. The constant angular velocity depends on the number of cells per island and decreases with increasing number of cells. Changes in the direction of rotation occur rarely, mostly in correspondence with cell division events and occasionally spontaneously. The onset of collective rotation is a symmetry breaking event. Cellular symmetry breaking is manifested in three experimental

observations: the intrinsic asymmetry the cortical network, a contact-induced persistence in the directionality of cell migration and cell polarization in the plane of the epithelium. This experimental approach is valuable because the defined boundary conditions and the reduced number of cells enable a better characterization of the observed phenomena. Oligocellular tissues make theoretical modeling amenable and the knowledge gained here can help to understand collective cell migration in more elaborated systems such as wound healing assays and morphogenesis.

The process of cellular self-organisation in single cell arrays is also investigated. A novel kind of patterned substrates are developed which provide adhesive islands that are preferred for permanent cell adhesion and repellent areas on which cells can migrate. The migrational behavior of cells in such substrates is studied.

Lastly, a novel fabrication process that allows multifunctional patterns consisting of three different surface functionalizations is described. These ternary substrates open a new field of experimentation. For example, squares with different functionalities at the rim and the interior can be created.



# Chapter 1

## Introduction

A living cell is the basic unit of life even though it is a highly complex system. In a fully developed organism, despite the fact that all cells carry identical genetic codes, cells exhibit well-differentiated phenotypes and are distinguishable in both form and function. In culture, cell behavior can vary greatly from cell to cell within the same population in a culture dish, exhibiting a wide variety of shapes, number of neighbors and stage of the cell cycle. It also has to be taken in account, that cells are not static systems and change their shape, restructure their contact to neighboring cells, and readjust internal composition and structure continuously in response to external stimuli [1]. Shortly, within the same population of cells we encounter a huge variety of cell initial states, what leads to heterogeneous responses at the single cell level. Conventional cell assays measure average responses of large cell populations, implicitly assuming that the average is representative of a typical cell within the population. An excellent counter-example for that is gene expression, where the cell population typically exhibits all-or-none responses. Single cell time-lapse analysis reveals that no individual cell will exhibit the response level predicted by the average population [2], [3]. Instead, because gene expression is an stochastic process [4], cells become activated asynchronously and there are expressing and non expressing cells. While the average population response increases gradually, single cell responses are more abrupt and exhibit a broad distribution of gene expression onset times [2]. Single cell assays are valuable because they enable to quantify the distribution of behaviors amongst a population of individual cells, however they don't allow to study cell-cell interactions and collective phenomena such as epithelial cell packing or cohort migration. Gaining insight into the biophysics of the cell through conventional living cell assays is thus challenging. For this reason, living cell assays have to be improved in two critical aspects; the ability to control the local cell environment and/or the delivery of stimuli, generating uniform initial experimental conditions, and the capability to measure cellular responses [3]. Homogeneous experimental conditions together with defined cell microenvironments would facilitate quantitative measurements, automated image processing and the development of high-throughput screening platforms.

Micropatterning techniques give us control over the local protein environment of the cell and have already been proved successful in maintaining cell populations in specific

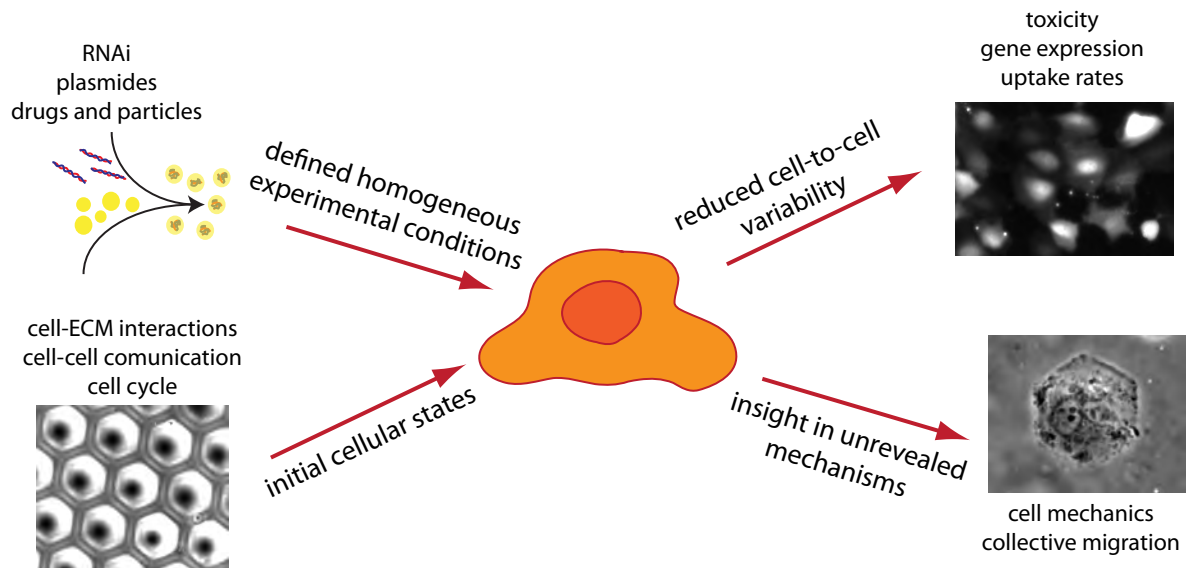


**Figure 1.1: Schematic diagram of the work.**

shapes on predetermined positions [5], [6], and in controlling individual cell behavior, such as switching between apoptosis and growth [7] or determining the direction of cell migration [8]. On top of that, they offer not yet fully appreciated advantages. Micropatterned substrates can be used to impose defined boundary conditions to multicellular systems and to prevent cell extension by confinement, what in turn could be used to synchronize populations of cells by contact inhibition of cell division. Hence, micropatterning techniques are appropriated to define the cellular microenvironment and generate controlled cellular “initial states”.

In nature, there is a small beautiful system which contains very much valuable information about cell behavior. The *Drosophila* compound eye is composed of about 800 unit eyes, called ommatidia, which are arranged in a precise honeycomb-like array as seen in Fig.1.2. Each ommatidium is a precise assembly of 20 cells: four cone cells are surrounded by two primary pigment cells, which are as well surrounded by six secondary and three tertiary pigment cells, and three bristle cells. All ommatidia have exactly the same cell packing, see Fig.1.2, which is indispensable for correct vision. From this system we learn that groups of cells try to minimize the total surface area, similar to soap bubbles [9], as shown in Fig.1.2, and that different types of cells sort out as immiscible liquids would do.

Inspired in this natural system, here, small groups of epithelial cells are confined all together within an adhesive island and their collective behavior is studied. It is shown that imposing constrictions to multicellular systems enables the study of phenomena that do not appear at the single cell level and are too complex to analyze at the full tissue level. The defined boundary conditions and the reduced number of cells enable a better characterization of the observed phenomena.



**Figure 1.2: Ommatidia in the *drosophila* retina.** The precise honeycomb like cell packing in ommatidia contains very much valuable information about epithelial cell mechanics. For example, cone cells behave similar to soap bubbles and adopt a configuration that minimizes the total surface area. Reprinted with permission from Macmillan Publishers Ltd: Nature [9], copyright 2004

This thesis is structured as follows:

The second chapter will first give an introduction to basic cell biology concepts, for those lecturers which are not familiarized with them, and later will compile the experimental and theoretical foundation needed to understand cell behavior in tissues.

In the third chapter the internalization of nanoparticles by cells is studied and an efficient and reproducible strategy of presenting nanoparticles to cells is developed. This approach not only assures uniform and controlled densities of NPs to be presented to the cell, but it also enables uptake quantification. In the next chapter, the knowledge gained here is applied to gene delivery particles.

Chapter 5 begins with a description of standard patterning techniques such as micro-contact printing ( $\mu$ CP) and microscale plasma-initiated patterning ( $\mu$ PIP). Here, the  $\mu$ PIP technique is refined, enabling to create defined cellular microenvironments easily, fast and with high reproducibility. With the introduced improvements, long range patterned surfaces which provide preferred adhesive areas with predetermined sizes and shapes can be created. This patterned substrates will be used in the following chapters to study epithelial cell packing and collective migration.

In chapter 6 epithelial cell packing in square adhesive islands is studied. The fundamental characteristics of the observed packing states and their experimental distribution are elucidated. In the next chapter, theoretical modeling in collaboration with Karen Alim from the group of Erwin Frey, LMU, Munich, is applied in order to explain the experimental distribution of packing states. Here, oligocellular arrays unravel new contributions to epithelial cell packing and the current vertex model is extended.

In chapter 8, preliminary results regarding the collective rotation of small groups of MDCK cells in circular adhesive islands are presented and symmetry breaking events are investigated. The basis for a theoretical framework for modeling collective cell rotation

taking in account biochemical cell coupling is proposed.

In chapter 6 it is revealed that cell confinement is not enough to trigger contact inhibition of cell division. Instead, cells are expelled from overpopulated adhesive islands and are able to migrate to neighboring empty adhesive islands, crawling over the repellent parts of the patterns. This novel substrate property is investigated in chapter 9 with the goal of creating single cell arrays by cellular self-organisation.

During the course of this thesis, the limitations of the patterning techniques presented in chapter 5 become evident and continuous effort was made in order to overcome technical hurdles and develop new patterning approaches. The results of this work are summarized in chapter 10. In this chapter, a fabrication process that allows multifunctional patterns consisting of three different surface functionalizations is described.

In each chapter a detailed introduction to the treated theme is given.

# Chapter 2

## Fundamental concepts

### 2.1 Cellular biomechanics

Cells are the basic units of life and still biologically complex systems: they are soft and wet, and their internal composition and structure changes continuously in response to external stimuli [1]. Here, the *physical* attributes of cells, such as their basic structural elements, and basic cellular processes, such as cell-cell adhesion, cell-substrate adhesion, endocytosis, cell migration and polarization, are briefly described for those lectors which are not familiarized with these concepts.

From the mechanical point of view, the properties of a cell are defined by the cytoskeleton, the plasma membrane and the volume occupied by the cell.

Membranes are found throughout the cell, enclosing the nucleus, individual organelles and the cell itself. They are dynamic, fluid and inhomogeneous lipid bilayers containing a variety of specialized proteins. The plasma membrane is the interface between cells and their environment, but it is not only a physical barrier, uptake of nutrients, cell-substrate adhesion and all communication among cells occurs through this interface. It creates a barrier for selective transport of substances, what permits the cell to maintain cytosolic constituents and conditions, as optimum ph level, different from those in the surrounding environment and stable despite variations in this environment. The plasma membrane is so important that loss of membrane integrity is related to cell death.

The cytoskeleton is an elaborated network of protein filaments that extends throughout the cytoplasm, and it is the primary source of mechanical strength inside cells [1]. It gives the cell form, allows it to move, helps organize cellular contents, to anchor cells to its substrate and neighbors, and speeds the transport of materials within certain types of cells. It is composed of three types of protein filaments:

- intermediate filaments have great tensile strength and bear the mechanical stress that occurs when cells are stretched. They typically surround the nucleus and extend out to the cell periphery, where they are indirectly connected to the extracellular matrix and neighbor cells through hemidesmosomes and desmosomes.

- microtubules are long and relatively stiff hollow tubes of protein. They serve as structural components within cells and are involved in many cellular processes including mitosis, cytokinesis, and vesicular transport. They grow out from the centrosome extending towards the periphery of the cell and show structural polarity.
- the actin cytoskeleton consists of functionally different subsets of actin filament arrays that contribute to cell migration, shape changes, adhesion, and uptake of extracellular and plasma membrane components. Although actin filaments are distributed throughout the cell, actin is concentrated in a layer just beneath the plasma membrane, called cell cortex, that reinforces it. Actin filaments in the cortex are crosslinked by actin-binding proteins where myosin motors generate contractility. Polymerization and depolymerization of cortical actin contributes to the extension of cell protrusions and cell locomotion. The actin cytoskeleton is connected to the extracellular matrix and neighbor cells through integrins and adherent junctions respectively.

### 2.1.1 Cell-substrate adhesion

Upon contact to a medium containing serum, the bare surface of a material is rapidly (usually in seconds) covered with adhesion proteins that are absorbed from it. The chemistry of the underlying substrate, particularly wettability and surface charge, controls the nature of the adherent protein layer, which gives the substrate its biological identity. Normally, these proteins arrive to the surface much faster than cells do. Cell adhesion to this protein layer is mediated by receptors in the cell membrane, most integrins, and is a dynamic process, where cell-surface and matrix-associated molecules interact with each other in a spatially and temporally regulated manner. In vivo, these interactions play a major role in tissue formation and cellular migration [10].

To understand the cell-substrate interaction it is necessary to learn about the extracellular materials that form the cell's substrate.

#### The extracellular matrix

The extracellular matrix (ECM) is very complex and consists of a large number of highly specialized macromolecules. These macromolecules are found in essentially all tissues and are fundamental for our normal growth and health. ECM molecules have biological activities that range from structural support to the regulation of transcription activity. It is not a mere scaffold between cells but rather an information-rich supra-molecular structure that provide cells with signals that regulate cell growth, differentiation, and apoptosis. Cells read the barcode-like signals written in the matrix with a variety of cell surface receptors and determine whether they should grow or differentiate. Any attempt to make a sophisticated, functional surface for biointeractions must take into account the highly developed ability of biological systems to recognize specially designed features on the molecular scale [11].

Some of the most important components of the ECM are:

- Collagen comprises a family of fibrous proteins that impart structure and rigidity to a tissue, being responsible for tensile tissue strength. It is the most common protein in the body. There exist nearly 20 different types, which can be classified in fibrillar, the most abundant, and non fibrillar collagens. Some examples of them are:
  - collagen type I forms large structural fibre bundles in tendons, ligaments and other tissues exposed to mechanical load
  - collagen type IV forms x shapes complexes that associate together to create highly interconnected fibrous network, it's abundant in the basement membrane
  - collagen type VI widely distributed throughout the ECM and help cells to form attachments to the surrounding matrix.
- As the name indicates, elastin gives elasticity and resilience to tissue as, unlike collagen, it can be stretched. It is present in the walls of arteries, lungs, skin, hearth valves and intervertebral disks.
- Proteoglycans are long chained polysaccharides called glycosaminoglycan (GAGs) that are covalently bound to proteins. They are highly hydrophilic and therefore can absorb and retain large amounts of water. The most common proteoglycans are heparan sulfate, found in the basal lamina, chondroitin sulfate and dermatan sulfate.
- Hyaluran is a free GAG, not bound to protein, but that can associate non-covalently to ECM proteins. Its large size and strong negative charge allow it to bind a large amount of water, forming a viscous gel. This component keeps a tissue hydrated, provide resilience and lubricates.
- Adhesion proteins permit cells attachment to and movement within the ECM. The most important are:
  - laminin is a key component of the basement membrane and binds to collagen IV and other matrix components, and cell surface integrins.
  - fibronectin posses specific binding domains for collagen, cell surface integrins and heparin sulfate. It is ubiquitous, the all purpose glue of the ECM, and plays a crucial role guiding and promoting cell migration during embryonic development and wound healing.

## Integrins

As mentioned before, cell-substrate attachments are mostly mediated by integrins, in form of focal adhesions and hemidesmosomes. Integrins receive this name because they “integrate” the function of the cell with the outside world, this is the ECM. Formation of focal

adhesion depends on the cell substrate and it is promoted by ECM adhesion proteins attached to it. Integrins are transmembrane proteins that exist in cells as heterodimers of two distinct polypeptides called  $\alpha$ - and  $\beta$ -integrin. In focal adhesions, one domain of the integrin molecule is exposed on the cell surface, and binds for example to fibronectin, while the cytoplasmic domain forms an attachment site for actin filaments [1]. In this way, the cytoskeleton becomes mechanically linked to the ECM, and the integrin molecule can transmit stress from the matrix to the cytoskeleton. Focal adhesion formation requires the side-by-side association of integrin molecules to form a cluster in the membrane, signaling molecules, and mechanical tension. Focal adhesions are dynamic structures which assemble, disperse and recycle during cell migration. They transmit force or tension to maintain strong attachment to the ECM and act as signaling centers regulating many intracellular pathways of different cell functions. Since integrins act as the “feet” of a migrating cell by supporting adhesion to the ECM or other cells and by linking via adapters with actin filaments on the inside of the cell, they naturally constitute a major family of migration-promoting receptors [12]. In hemidesmosomes, as told at the beginning of this section, integrins link intermediate filaments to the matrix. For a more detailed description on integrin functions see [13].

### Cell adhesion to surfaces

Putting it all together, cell adhesion to surfaces comprises a cascade of five effects:

- absorption of serum proteins from the medium to the surface,
- approach of cells to the surface and initial cell attachment,
- cell spreading,
- organization of actin cytoskeleton
- and formation of focal adhesions.

#### 2.1.2 Cell-cell adhesion

Epithelial cell adhesion is initiated with the formation of apical adherens junctions, which are composed of cadherin adhesion molecules interacting in a dynamic way with the cortical actin cytoskeleton.

Cells usually establish the initial contact via membrane protrusions, such as filopodia and lamellipodia. These first physical contacts are then stabilized by classic cadherins, which stop diffusing freely in the membrane and become immobilized, presumably by anchoring to actin. Homophilic ligation of cadherins triggers actin cytoskeleton rearrangement, expanding the surface of contact, which matures into a full adherens junction, and stabilizing it [14].

Other types of cell-cell junctions are:



- tight junctions create a seal between adjacent cells to limit the diffusion of ions and small molecules
- gap junctions have the opposite role than tight junctions, providing channels for the exchange of small molecules between cells
- desmosomes are also formed by cadherins but they are linked to the intermediate filaments

### 2.1.3 Cell shape

Animal cells, in the absence of forces from other cells and the substrate, present a spherical shape. This shape is primarily dictated by the forces generated in the actomyosin cortex, which prevent cytoplasmic expansion. Current physical models for shape and shape change of isolated cells assume the cytoplasm to be a viscoelastic material. Shape change is driven by polymerization and contraction of the cortex, and is usually assumed to occur without local or global changes in cytoplasmic volume [15].

Cell anchoring and spreading on a surface involve cell shape deformation. As focal adhesions are formed, the cytoskeleton is connected at these discrete points to the ECM and the cell acquire a flattened shape. Adherent cells have been proposed to be tensegrity structures. Tensegrity is a form of tensile architecture that uses tension and compression in a combination that yields strength and resilience beyond the sum of their components. In cells, microtubules act as struts while contractile microfilaments provide tension, acting like stretched rubber bands that compress the microtubules and pull on the extracellular matrix through adhesion points [16], [17], [18], [19].

### 2.1.4 Portals of entry into the cell

Endocytosis encompasses several diverse mechanisms by which cells internalize macromolecules and particles into transport vesicles derived from the plasma membrane[20]. Two sets of endosomes can be distinguished; early endosomes, just beneath the plasma membrane and late endosomes, near the nucleus. Uptake mechanisms fall into two broad categories:

- phagocytosis, which acts for the uptake of large particles and is restricted to specialized cells,
- pinocytosis, which can be carried out by all cells using at least four mechanisms: macropinocytosis (particles up to  $1\mu\text{m}$ ), clathrin-mediated endocytosis ( $\approx 120\text{nm}$ ), caveolin-mediated endocytosis ( $\approx 60\text{ nm}$ ) and clathrin and caveolin independent endocytosis ( $\approx 90\text{nm}$ ) [21], [20].

### 2.1.5 Cell migration

Cell migration plays an essential role in a wide variety of biological phenomena as immune response, wound healing, tissue maintenance, and morphogenesis, as well as pathological events including vascular disease, chronic inflammatory diseases and tumor metastasis.

Cell migration fundamentally polarized process, in which the dynamic assembly and disassembly of focal adhesions plays a central role. It is a cyclical process that starts with cell polarization, which implies a clear distinction between the cell front and its rear, followed by the formation of a protrusion in the direction of movement. Next, integrins bind to the ECM ligands, forming adhesion sites that serve as traction points for migration and also stabilize the protrusion via structural connections to actin filaments. Finally, the rear edge of the cell contracts toward the nucleus and the adhesion receptors are released from the cytoskeleton, detaching the cell from the previous attachment sites [12].

It is clear that both, the establishment of strong and weak adhesion, inhibit migration. Strong adhesion hinders rear release while weak adhesion does not support traction. Thus, cell migration is fastest at optimum adhesion strength: strong enough to support traction but weak enough to allow rapid detachment of the rear of the cell.

### 2.1.6 Cell behavior in tissues

A tissue can be considered as a building, where form and stability are determined through a dynamic equilibrium of physical forces [22]. In this building, cells are bricks and the extracellular matrix is a flexible armature that provides stability. An enormous difference between buildings and tissues is that the firsts are constituted by rigid substructures while in a tissue the elemental components, cells, are soft and able to change their shape and internal structure.

Animal tissues are diverse, in osseous tissue the extracellular matrix is abundant and mineralized, what makes the tissue very rigid and resistant against traction and compression, and direct attachments between cells, which are sparsely distributed within the matrix, are relatively rare. In epithelial tissue, cells are tightly bound together, through epithelial cell-cell junctions, into sheets called epithelia. The extracellular matrix is exiguous, forming a thin layer, called basement membrane, underlying the epithelium [23]. In the following, we will talk about epithelial cell sheets, that cover internal and external body surfaces.

There are various types of epithelia, shown in Fig.2.2, which are classified according to cellular morphology and the number of cell layers. In a simple epithelium the cells form a single layer and are all attached to the basement membrane. A stratified epithelium consists of multiple layers of cells in which only the basal layer is attached to the basement membrane. Simple epithelia are typically classified based on the morphology of the component cells: squamous (flat), cuboidal, and columnar, see Fig.2.1. Columnar cells can have cilia or microvilli. The name of a stratified epithelium is determined from the shape of the apical layer of cells. The shape of the nucleus usually corresponds to the cell form and helps to identify the type of epithelium.

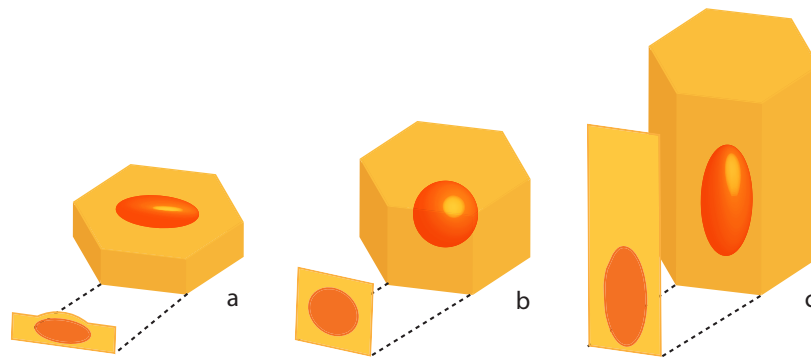


**Figure 2.1: Types of epithelial cells.** Schematic representation of a) squamous b) cuboidal and c) columnar cells

Simple cuboidal epithelium (Fig.2.2 a) consists of boxy (cuboidal) cells, that are isometric in vertical section and polygonal when sectioned horizontally [24], see Fig.2.1 b. Each cell has a spherical nucleus in the centre. Cuboidal epithelium is commonly found in secretive or absorptive tissue.

Simple squamous epithelium (Fig.2.2 b) consists of a single, very thin layer flattened (squamous) polygonal cells that fit closely together, providing a smooth, low-friction surface over which fluids can move easily. Squamous cells tend to have horizontally flattened, elliptical nuclei, as sketched in Fig.2.1 a. Classically, squamous epithelia are found lining surfaces utilizing simple passive diffusion such as the alveolar epithelium in the lungs.

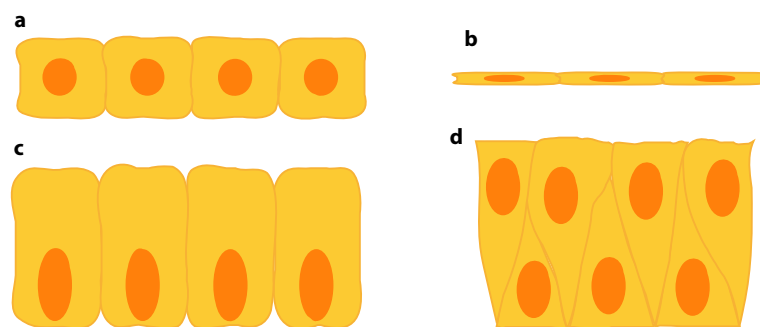


**Figure 2.2: Types of epithelium.** a) simple squamous b) simple cuboidal c) simple columnar d) pseudostratified

Simple columnar epithelium (Fig.2.2 c) consists of a single layer of tall (columnar) cells. They have height to width ratios significantly greater than one, and like cuboidal cells, are polygonal when sectioned horizontally, see Fig.2.1 c. Simple columnar epithelium is usually involved in active specialized secretion and/or absorption of material across the single cell layer, or, if ciliated, in movement along the surface. Their nuclei are elongated and are usually located near the basement membrane. Some columnar cells are specialized for sensory reception such as in the nose, ears and the taste buds of the tongue.

There is another variety of epithelium, called pseudostratified epithelium and depicted in Fig.2.2 e, where the cell nuclei are positioned in different layers, suggesting a stratified epithelia, but in reality is composed of a single cell layer since all cells are in contact with basement membrane.

In this work, two cuboidal epithelium cell lines, human hepatocarcinoma cells, Huh 7, and Madin-Darbey canine kidney cells, MDCK, were used.

### 2.1.7 Epithelial cell polarisation: symmetry breaking

A fundamental feature of epithelial cells is that they have polarity in terms of their morphology and orientation. Together with apico-basal polarity, most epithelia are also polarized in a second axis, in the plane of the epithelium. This phenomenon is known as planar cell polarity or tissue polarity. Planar polarity coordinates cell behavior across the epithelium and is clearly visible in the epidermis of animals. For example, the scales, bristles, and hairs of insects are typically aligned along the major body axis [25].

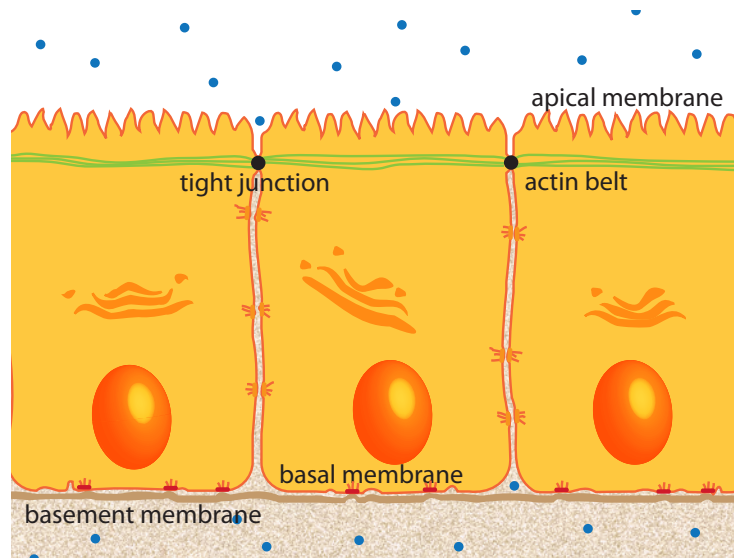


**Figure 2.3: Epithelial polarisation** is triggered by an asymmetric distribution of cell-cell and cell-substrate adhesion points.

#### Apico-basal polarity

Apico-basal polarity is triggered by an asymmetric distribution of external cues, in terms of cell-cell and cell-substrate adhesion points, that generates asymmetries within the plasma membrane. As we mentioned before, epithelial sheets line the cavities and surfaces of all structures throughout the body, this means that the upper side of the cell faces the free surface, or lumen, the bottom side faces the basal lamina and contains cell-substrate adhesion points, and the lateral sides are in contact with adjacent cells, and contain cell-cell

adhesion points, see Fig.2.3. This spatial polarity implies the organization of the plasma membrane into structurally and functionally distinct domains: the part of the plasma membrane facing the lumen is called apical domain, the part facing the basal lamina is called basal domain, and the rest is the lateral domain.

Polarized epithelial cells are characterized by [26]:

- proteins and lipids in the plasma membrane are distributed in three distinct surface domains: apical, lateral and basal.
- the apical and lateral surface domains are separated by tight junctions, which form barriers to intercellular diffusion of ions and macromolecules.
- cell adhesion molecules form cohesive cell-cell interactions and a highly-developed junctional complex consisting of tight junctions, desmosomes and gap junctions.
- cytoplasmic organelles and cytoskeleton are polarized distributed within the cell.

It is important to point out that both processes, lateral cell-cell adhesion and cell-substrate adhesions on one side of the cells, are necessary for successful epithelial cell polarisation [27], [28]. Cell-cell adhesion establishes a "landmark" on the cell surface, which defines a domain of the plasma membrane that is different from the rest of the plasma membrane not in contact with another cell, while the plasma membrane assumes apical character wherever no adhesive interactions take place.

### Planar cell polarity

Planar cell polarity (PCP) is a property of multicellular tissues that demonstrates a coordination of cell behavior across a two-dimensional sheet, orthogonal to the axis of apical-basal polarity. This global property of tissue structure requires the establishment of asymmetry within cells and the alignment of these asymmetries in cells located dozens or hundreds of cells apart [29]. The spatial information that organizes planar polarity is transmitted locally from one cell to the next in form of an asymmetric cortical distribution of core PCP proteins [30]. These proteins "attract" each other across cell boundaries, while each locally inhibits the presence of the others within a cell [31], as depicted in Fig.2.4. Input from neighboring cells can influence the behavior of individual cells as well as the orientation of groups of cells that respond as a unit to directional cues [29]. PCP is also involved in cell migration during morphogenesis, in processes such as the elongation of the body axis or collective rotation in ommatidia [29], [30].

## 2.2 Physical models of tissues

In this section, simple models which describe tissues as physical systems are presented.

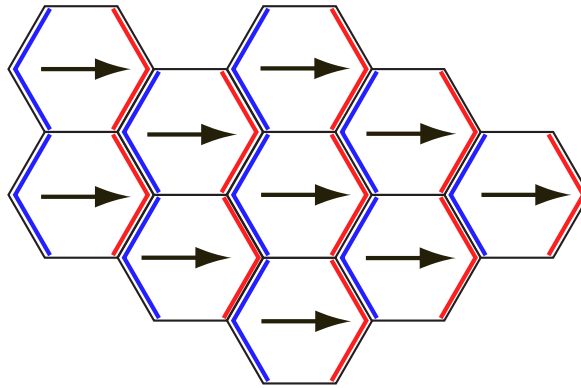


**Figure 2.4: Schematic of PCP protein asymmetric distribution.** The spatial information that organizes planar polarity is transmitted locally from one cell to the next in form of an asymmetric cortical distribution of core PCP proteins. These proteins “attract” each other across cell boundaries, while each locally inhibits the presence of the others within a cell. The asymmetric distribution of PCP proteins introduces a directionality in the cell, illustrated with arrows. Adapted from [31].

### 2.2.1 Tissue surface tensions: the differential adhesion hypothesis

In the first half of the last century, during his tenure as professor in the university of Munich, Johannes Holtfreter disaggregated cells of a neurula-stage embryo, mixed them together randomly and observed their extensive capacity to sort out, to selectively adhere, and to reconstitute well-organized tissues similar to those of the intact embryo. Together with Townes [32], he came to the conclusion that the transformation of a single fertilized egg in a patterned body was due to *tissue affinity*. These observations could not be completely explained until in 1964 Steinberg proposed the differential adhesion hypothesis (DAH). The hearth of this hypothesis is that cell aggregates show striking similarities with fluids and soap bubbles, as proposed by Thompson in his book “*On growth and form*” [33]. First, cells tend to aggregate in clusters in which the surface area of contact with the surrounding environment is minimized. Second, different cell populations can become sorted into two phases like immiscible fluids, maximizing the binding energy. The DAH thus proposes that, since they are composed of motile cohesive subunits, tissues can be treated as newtonian liquids at long time scales. A noteworthy difference between cells and liquid molecules is that cells show active locomotion instead of brownian motion. By analogy to liquids, it is possible to define a tissue surface tensions that would determine the mutual interaction of the tissues. The DAH further proposes that tissue interfacial tensions increase linearly with the expression level of adhesion molecules, such as cadherins, on the cell surface [34], and that differences in intercellular adhesion guide tissue segregation, mutual envelopment and the sorting of embryonic tissues [35]. The implications of the DAH can be summarized as follows:

- the minimal surface configuration of a tissue is equivalent to a state of adhesion

maximization. Comparably to a liquid it is achieved by rounding up to a sphere.

- a heterogeneous mixture of cells will sort out according to the relative surface tensions of the constituent cells. The cell population possessing a higher surface tension will form a compact sphere that will be surrounded by the less cohesive cell group.

Cell sorting of cells according to the differences in cellular cadherin expression of cells is illustrated Fig.2.5.

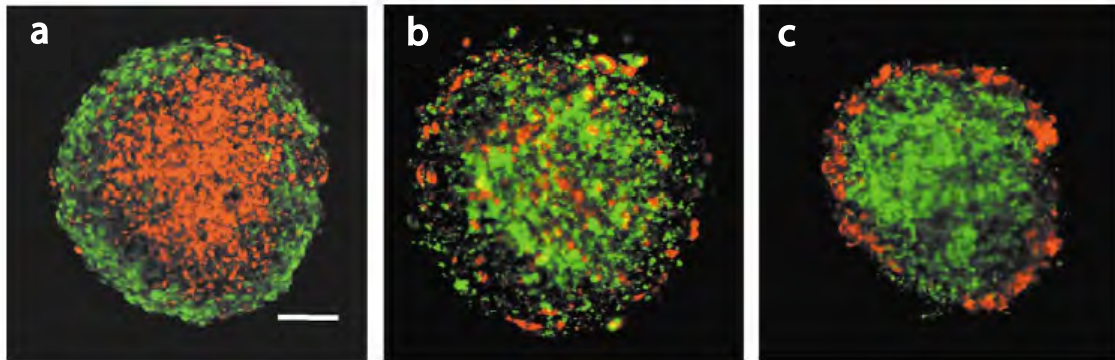


**Figure 2.5: Differential adhesion hypothesis.** L cells expressing P-cadherin (red) or E-cadherin (green) sort out only when they differ in cadherin expression level. **a.** Cells expressing P-cadherin at a higher level form stronger cell-cell contacts and become surrounded by E-cadherin expressing cells. **b.** Cells expressing the same levels of P-cadherin and E-cadherin do not sort out. **c.** Cells expressing P-cadherin segregate externally, surrounding cells expressing E-cadherin at a higher level. Reprinted from [36], Copyright 2003, with permission from Elsevier.

### 2.2.2 Cell and tissue shape: interplay of cortical tension and cell-cell adhesion

Minimizing total surface area is, however, not enough to explain cell packing in ommatidia [37]. As explained in section 2.1.3, the shape of isolated cells is primarily dictated by cortical tension and, thus, cortical tension is an important ingredient of cell surface tension. To a first approximation, cadherin and the cortical tension have opposite contributions to interfacial tension; while adhesion interactions tend to increase the surface of contacts between apposed cells, cortical tension due to the formation of a contractile acto-myosin network at the zone of contact reduces the contact surface. Yet, adhesion and cortical tension are not independent because both are supported by actin filaments [38]. As showed by Käfer et al. [37], it is necessary to take in account the effect of the cortical cytoskeleton to completely explain ommatidia topology and geometry.

### 2.2.3 Vertex models

Mathematical modeling approaches have recently been applied to explain the properties and structure of epithelial tissue [37], [39], [40], [41], [42]. Vertex models are based in two hypothesis:

- since actin cortex and cell junctions are mostly restricted to a region  $1\mu$  thick just below the apical membrane, it is considered that the basal region of the cells responds passively to cell deformation, occurring in the plain of adherens junctions, and has a minor mechanical role [42].
- cells are subjects to the laws of thermodynamic, and their tendency is to adopt the most stable, lowest energy configuration [40]

Making this two assumptions, cell networks can be considered as two-dimensional sheets defined by two-dimensional polygons representing cells, straight lines representing cell walls, and vertex points representing cell wall junctions. Such a model describes the forces that act to displace vertices and obtains cell packing states, considered to be stable and stationary network configurations, by minimizing a potential energy function.

Current models define the homeostatic tissue state to be determined by the interplay of cortical actin contractile forces, contact favoring adhesion forces and elastic forces. Regulation of these balancing forces determines cell packing geometry and drives large scale reordering of cells within tissues during development.

As described by [37], any stable and stationary configuration of the network corresponds to a local minimum of the following energy function:

$$E = \sum_{i=1}^N \left\{ \epsilon(A_i - A^0)^2 + \kappa P_i^2 - \alpha \sum_{j \in \nu(i)} L_{i,j} \right\} \quad (2.1)$$

The first term takes in account cell elasticity by a elastic coefficient  $\epsilon$ . Any deviation from the cell area  $A_i$  with respect to the preferred cell area  $A^0$  increases the energy of the system. The preferred area is determined by cell height and volume and, thus, the height of the cell is indirectly considered in this term.

The second term describes the contractility of the cell perimeter  $P_i$  in terms of the contractility coefficient  $\kappa$ . As we described before, the cortical tension generated in the actin-myosin ring acts to minimize cell perimeter.

Adhesion between cells tends to extend their contact length  $L_{i,j}$ . This is contemplated through the adhesion coefficient  $\alpha$  in the third term.



# Chapter 3

## Towards a defined presentation of nanoparticles to cells

In this chapter, an original approach to study NP-cell interactions is established: NPs are immobilized onto surfaces prior to cell exposure and cells are seeded on top of the NP layer. This proceeding separates particle preparation on the surface from incubation in cell medium, preventing NP aggregation and allowing well-defined particle number densities to be presented to the cells. Besides, the surface on which NPs initially lay provides a reference that enables internalization assessment and quantification. In addition, NP internalization routes and end-locations inside cells have been studied with transmission electron microscopy (TEM). This approach has been developed for one type of NPs, but it can be optimized for screening all kinds of particles with different sizes, shapes, and physicochemical properties, and improved to allow accurate quantification. The results presented in this chapter have been published in [43].

### 3.1 Motivation

Understanding the interactions between nanoparticles (NPs) and cells, in particular NP uptake, is a very important task for assessing nanotoxicity and can help to gain a better understanding of cellular uptake mechanisms, which are a key aspect in developing efficient gene and drug delivery systems[44]. However, the small size and the colloidal nature of NPs cause major experimental hurdles. Most nanotoxicity studies handle NP dispersions as molecular solutions, even though they immediately destabilize when mixed with an electrolyte rich solution such as cell growth medium. NPs coagulate and precipitate onto the cells and real particle size and exposure concentration remain undetermined. This phenomenon can have dramatic consequences for cells, as we observe when trying to study NP internalization of 4nm gold particles with TEM (see Fig.3.1), and lead to distorted results in nanotoxicity assays.

When incubated with cells, NPs attach everywhere on the uneven cell surface. In a first approximation, it can be considered that all particles that contact the cell surface

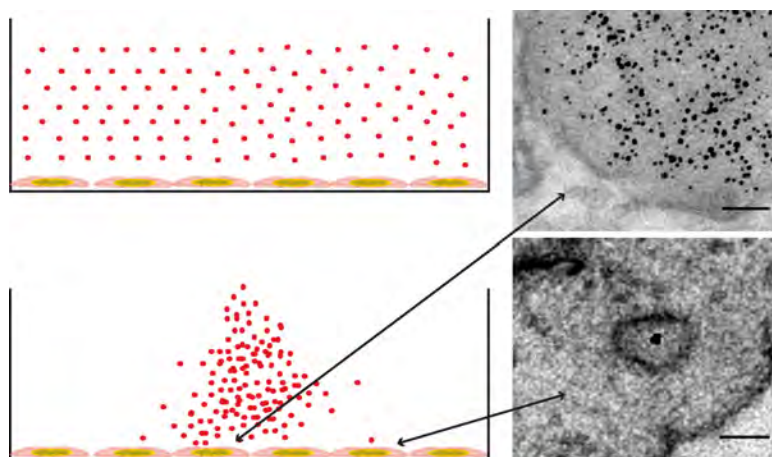


**Figure 3.1: Nanoparticle aggregation.** When colloidal nanoparticles come in contact with cell medium they collapse and coagulate, forming macroscopic aggregates. Immediate consequences of that are that not all cells in a culture are exposed to the same amount of nanoparticles, as can be seen in TEM micrographs, and that some cells become buried under macroscopic aggregates. Scale bars correspond to 50 nm.

will be internalized if the interaction time is long enough. This approximation may be adequate for long incubation times, however, the number of internalized particles will be highly overestimated for short incubation times and, for this reason, it is necessary to discriminate NPs just sitting on the cell membrane from those which have just been internalized. When it comes to this point, NP size arises as an inconvenient, since NP sizes fall well below of the optical resolution limit of conventional microscopes. For this reason, accurate quantification of taken up NPs still remains a challenge.

Assays which take in account the colloidal character of NPs need to be developed. Only such an assay can guarantee that all cells in the culture are exposed to the same amount of NPs, assuring reproducibility, and provide truthful results regarding NP toxicity, as well as the influence that NP size has on it and on uptake rates.

## 3.2 Introduction

During the last decades, it turned out that not only the chemical composition of a material determines its physicochemical properties. Surface and quantum mechanical effects cause nanomaterials to behave differently than bulk materials [45]. For example, a cube with an edge length of 1 cm presents 6 cm<sup>2</sup> surface area, while one cubic centimeter of closely packed hard spheres with a diameter of 6 nm, have a total surface area of 740 m<sup>2</sup> and thus present approximately 10000 fold enhanced chemical reactivity. The most popular example of quantum induced properties is the fact that the band gap of a semiconductor nanocrystal depends not only on the material but also on the particle size, the smaller the size of the crystal, the larger the band gap. This is because the confinement of the electrons in all

three spatial directions results in a quantized energy spectrum. Another result of quantum confinement effect is the appearance of magnetic moments in NPs of materials that are non-magnetic in bulk, such as gold, platinum, or palladium. These exceptional properties have triggered a rapid development of nanotechnology and the commercial use of NPs has increased dramatically, we found them in food products, sunscreens, toothpastes, skin care products, antibacterial silver coatings and paints. Although humans have always been exposed to nanomaterials in form of dust storms, volcanic ash or combustion products, and industrial nanoparticles constitute a tiny but significant pollution source [46], this rapid development of nanotechnology has raised concerns about potential toxicity and long term environmental issues [47], [48].

Up to date there are numerous studies that investigate the toxicity of prototype NPs such as  $\text{TiO}_3$  [49],  $\text{C60}$  [50], quantum dots [51], carbon nanotubes [52] and gold [53], [54]. It has been established that toxic effects are related to the ability of NPs to catalyze the production of reactive oxygen species [47], [28] and to bind irreversibly to membranes or DNA [55]. This causes interference at multiple levels of cellular metabolism, signaling and genetic alterations. All studies, so far, point towards a majority of intracellular rather than extracellular, interferences making the question of how NPs enter the cells is of utmost importance. Despite its significance, the uptake and internalization of nanoscale particles into cells is not completely understood [21]. Due to their small size, a priori, all uptake mechanisms (described in section 2.1.4) could be involved in the internalization process. Receptor-mediated internalization of NPs has been shown to be strongly size-dependent, with optimal uptake for NPs with a radius of around 25 nm [56], [57], [58], [59].

Important aspects that can influence NP toxicity are NP size, charge, surface modification and core material. Nevertheless, as explained in section 2.1.1, cells do not interact directly with a surface but with the protein layer which adsorbs to it. This means that, unless the surface modification of NPs is protein repellent, proteins will associate with NPs, leading to a protein “corona”, and it is this protein “corona” who gives NPs their biological identity [60]. Different surface modifications can lead to different amount and composition of the protein “corona”, but it is important to keep in mind, that it is this protein “corona” with which cells interact. The adsorption of proteins on NPs, not only changes their biological activity but it can lead to NP aggregation.

NPs in solution form stable colloidal systems. That means dispersions where the NPs are finely distributed in a medium and they resist flocculation and aggregation, and exhibit a long shelf-life. This depends upon the balance of the repulsive and attractive forces that exist between NPs as they approach one another. If all the NPs have a mutual repulsion then the dispersion will remain stable. However, these repulsive electrostatic forces are screened if, for example, charged polymers or ions are present in the solution, as happens in biological fluids, resulting in NP coagulation and sedimentary deposition onto the cells.

Let’s think carefully about the consequences of NP aggregation and sedimentation. First and trivial, when NPs aggregate they just stop being NPs and start to be large NP networks. The influence that particle size has on NP toxicity can thus not be studied. Second, when NPs sediment, cells become a NP dose that is much higher than pretended, as cells interact at once with all NPs present in solution, while not all cells in the culture

interact with the same amount of NPs, as can be seen in Fig.3.1. Thus, an important aspect of NP toxicity, in contrast to molecular toxicity, is the fact that the preparation and way of administration of the NPs plays a crucial role. The importance of NP characterization before conducting experiments for in vitro toxicity assessments has been emphasized in several recent reports [60], [61], [62], [63]. For such assays, NPs should be prepared as a monodisperse and stable colloidal dispersion.

### 3.3 The defined presentation of nanoparticles to cells and their surface controlled uptake

In this section, a novel approach to study NP internalization is proposed: NPs are immobilized onto surfaces prior to cell exposure and cells are seeded on top of the NP layer. In this way, the problem of NP aggregation and number density fluctuation is circumvented, as NPs are substantially separated on the surface preceding cell medium exposure. Moreover, using microfluidic channels and low salt buffer solutions, homogeneous and reproducible distributions of single quantum dots on surfaces are achieved. In addition, since the solid surface represents a natural reference frame ( $z=0$ ), NPs that are taken up by the cells can be defined as those being lifted above the reference plane ( $z > 0$ ), resulting in reliable detection of internalized NPs, as opposed to NP deposition on top of the cells.

#### 3.3.1 Model system

CdSe/ZnS quantum dots were chosen as solid model NPs. Fundamentally, these particles have a CdSe core which has been coated with a ZnS shell, in order to improve its optical properties, and are made water soluble by means of a polymer coating, in this case with a COOH terminal group. Due to their high quantum yield, great photostability [64], and the fact that the photoluminescence intensity of a single QD fluctuates with time, a phenomenon called blinking [65], it is possible to identify single particles even if they are well below the microscope optical resolution limit.

Quantum dot size was characterized by means of fluorescence correlation spectroscopy and transmission electron microscopy (TEM). Figure 3.2 shows the autocorrelation curve measured for QDs in water solution. They are not aggregated and their hydrodynamic ratio is  $r_h=(14,9\pm 0,4)\text{nm}$ , consistent with the core size measured with TEM,  $r_c=(4,8\pm 0,5)\text{nm}$ , and an extra polymer shell.

#### 3.3.2 Preparation of surfaces with a certain amount of well dispersed NPs

In order to achieve homogeneous and controlled particle densities on a solid surface, microfluidic channels and low salt buffer solution were used. Uniform distributions of NPs (Fig.3.3 b) and cells (Fig.3.3 c) at the bottom of a microfluidic channel are possible because

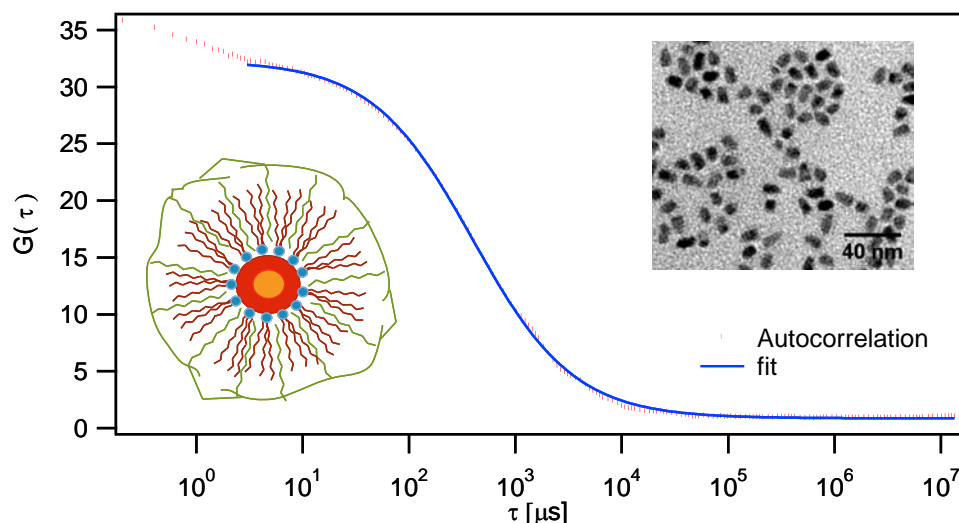


**Figure 3.2: Particle characterisation.** NP hydrodynamic radius and agglomeration states were studied with FCS. The autocorrelation curve is shown. The hydrodynamic radius for the QDs in water is found to be  $r_h = (14,9 \pm 0,4) \text{ nm}$ . NP core size and shape were determined with TEM. NPs are monodispersed, oval and have a mean size  $r_c = (4,8 \pm 0,5) \text{ nm}$ .

sedimentation occurs undisturbed by meniscus effects. Fig.3.3 a depicts the principle of NP preparation. To obtain a homogeneous distribution of single NPs, a very thin solution of NPs is filled in the channel. NP sedimentation time and concentration in solution can be combined to achieve distinct well-defined number densities of NPs at the surface, as shown in Figures 3.3 d,e and f. In fact, for a certain incubation time, the number of immobilized NPs/mm<sup>2</sup> is directly proportional to the initial concentration as seen in Fig.3.4.

Once the particles are on the surface, the solution is exchanged and cells are seeded followed by homogeneous spreading as shown in Fig.3.3 c. Note that NPs at the surface are not aggregated and remain in place after medium exchange, causing cells to receive a controlled, uniform and reproducible exposure to NPs.

With this simple setup the problem of nanoparticle aggregation, and subsequent undetermined exposure dose and experimental variability all over the cell culture, is circumvented. In addition, in the next section, it will be evidenced that it is possible to assess NP internalization by means of z-scan fluorescence microscopy.

### 3.3.3 Visualization of NP internalization

As depicted in Fig.3.5, the solid surface represents a natural reference frame ( $z=0$ ) where initially all NPs lay. Single QDs can be identified because of their blinking properties. NPs that are taken up by the cells, leave the reference surface and move upwards into the cell. Consequently, it is possible to define taken up particles as those being lifted above the reference plane ( $z > 0$ ). Starting from this surface, NP uptake can be studied monitoring

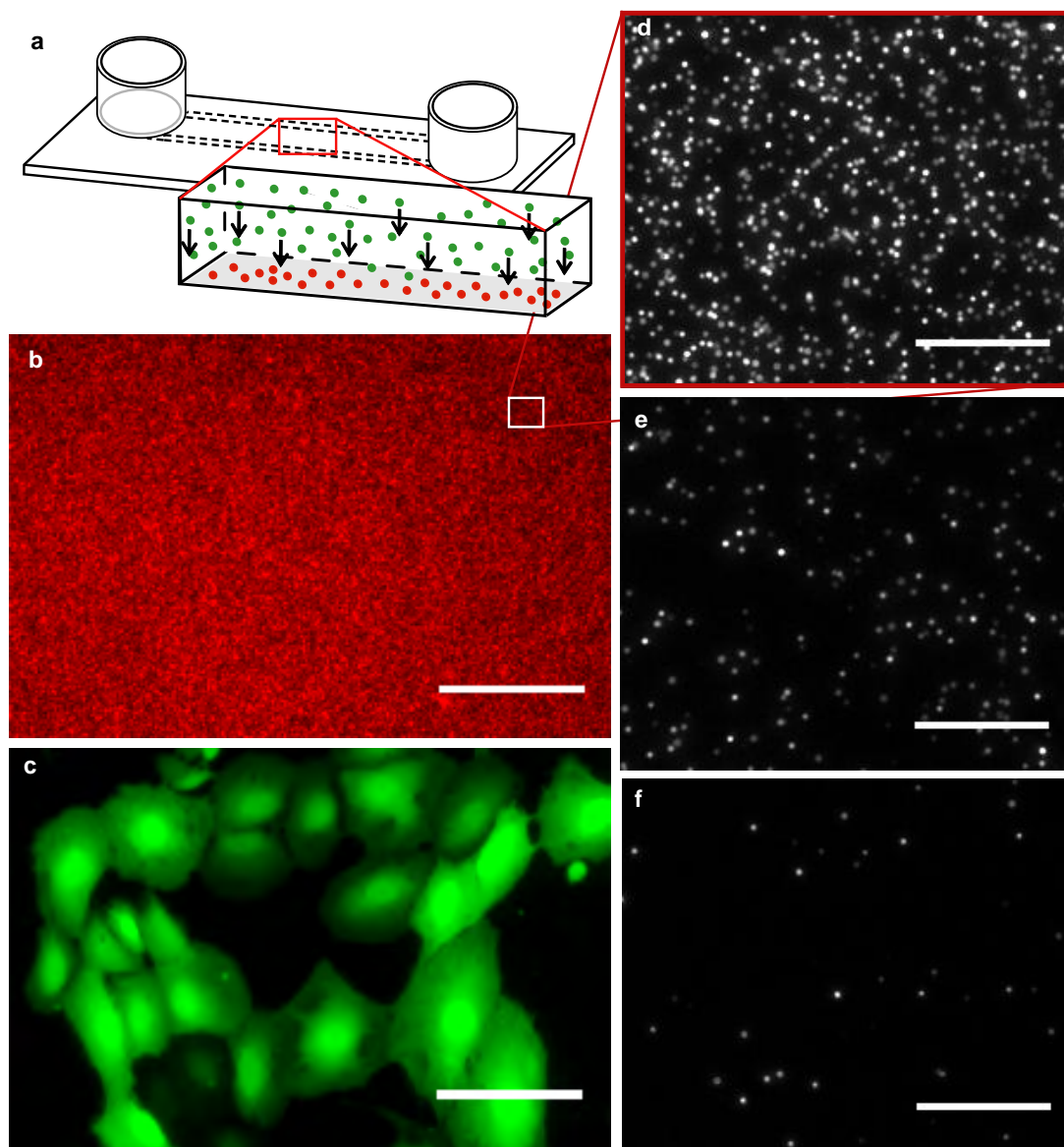


**Figure 3.3: Schematic representation of the nanoparticle surface preparation.** **a** Particles are injected and sedimented inside a  $\mu$ -channel in order to avoid meniscus effects. **b,c** Homogeneous distributions of NP (b) and cells (c) are achieved all along the channel. Scale bars correspond to  $50 \mu\text{m}$ . **d,f,e** NP surface density with varying nanoparticle concentration in solution (d)  $12,5 \text{ pM}$ , (e)  $25 \text{ pM}$  and (f)  $100 \text{ pM}$ . Scale bars correspond to  $5 \mu\text{m}$ .

**Figure 3.4: The number of adsorbed NP per surface area vs. the NP solution concentration.** For low concentrations and fixed incubation time we observe a linear dependence.

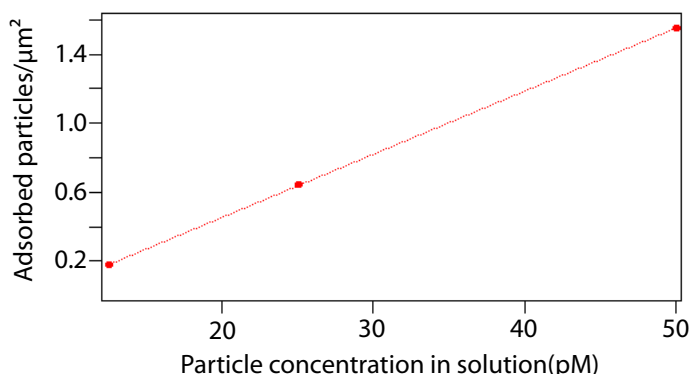
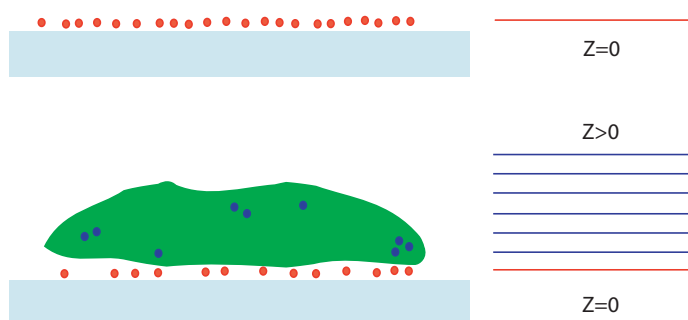


**Figure 3.5: Z-scan fluorescence imaging of NP uptake.** Initially NPs lay on the substrate surface ( $z=0$ ). NPs taken up are identified by their location above the reference plane ( $z>0$ ).



the position of NPs in a stack of z-scans.

Experimentally, first of all, the reference surface containing the NPs has to be identified. Then, starting from this surface,  $z=0$ , fluorescent micrographs with increasing  $z$ ,  $\Delta z = 0.5\mu\text{m}$ , are acquired, covering the whole height of the cell,  $z \approx 8\mu\text{m}$ . This distance between z-planes was taken because, even if it is enormous in comparison with the NP size, it represents a good compromise between taking on all internalized particles and skipping multiple counts due to out-of-plane fluorescence.

For image analysis an intensity threshold is established, so that out-of-plane fluorescence is blended, and z-scans are projected in the  $z$  plane using the ImageJ Grouped ZProjector plugin. The projected image is cross-checked with each single image to assure that two different particles with the same XY position but different Z were not projected on the same spot. Whenever this happened, the aforesaid particles were counted separately, as explained in the next section.

In Fig.3.6 a the fluorescent micrograph shows a cell in green, NPs on the surface in red and internalized NPs, in the range  $2\mu\text{m} < z < 8\mu\text{m}$ , in blue. In Fig.3.6 b and c, NPs at the surface (red) and internalized NPs (blue), along with the outlines of the nuclear and cytoplasmic membranes of a cell (black) can be seen. From this example, two conclusions can be extracted, first it is immediately evident that the blue spots are much larger than the red spots, indicating NP aggregation and formation of clusters inside cells, and second we find internalized particles entering the nucleus.

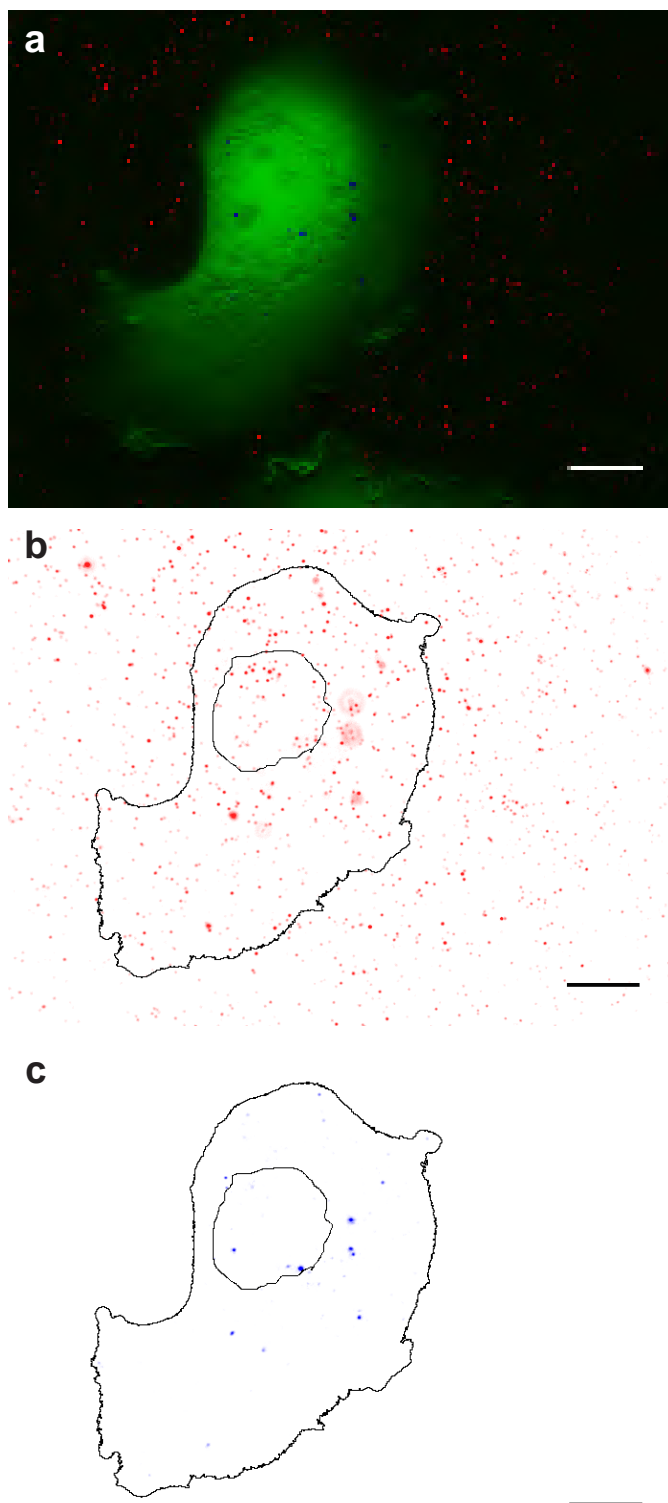
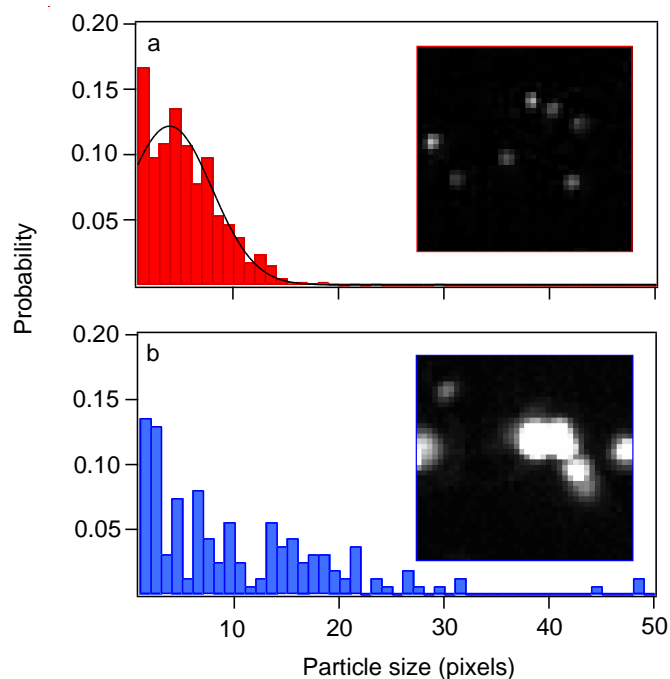


**Figure 3.6: Surface controlled nanoparticle uptake.** Fluorescence micrographs showing: **a** *Green*: GFP-expressing BEAS-2B cells. *Red*: QDs absorbed to the surface  $z=0$ . *Blue*: taken-up NPs (projection of image planes  $2 \mu\text{m} < z < 8 \mu\text{m}$ ). **b** *Red*: QDs absorbed to the surface *Black*: cell contour **c** *Blue*: internalized QDs *Black*: cell contour. Scale bars correspond to  $5 \mu\text{m}$



**Figure 3.7: NPs aggregate inside cells.** **a** Size distribution of absorbed NPs on the surface show a normal distribution of sizes (see fitted line). **b** Size distribution of NPs and aggregates inside the cell. Insets show representative fluorescence images for demonstration.



### 3.3.4 Quantification

Before uptake, all NPs are deposited on the reference surface and show clear spatial separation, as can be seen in Figures 3.3 d,e and f, and 3.6 b, and single QDs can be identified because of their blinking properties. The typical diffraction limited image of a QD is a 3x3 pixel area where the central pixel presents the highest intensity, see the inset in Fig.3.7 a. In this figure, the frequency of NP sizes on the surface is shown, exhibiting a normal distribution. After internalization, NPs form clusters inside cells, as seen from a larger image area in the inset in Fig.3.7 b, and mostly do not blink, due to the presence of multiple QDs in one spot. Since QDs are well below the optical resolution limit of the microscope, it is not possible to directly infer the number of NPs in a cluster.

However, it is possible to make an estimation of the number of NPs per cluster in terms of the fluorescent area of the cluster and the mean NP area. For this task, the following procedure was used:

- a threshold was chosen for the reference surface image, so that the maximal number of NPs is considered
- the resulting image was binarized
- the Particle Analysis plugin from ImageJ was applied, excluding spots bigger than 15 pixels
- the mean area size value of a particle on the reference surface was extracted from the obtained distribution of sizes

- the number of NPs in a cluster is then estimated dividing the total fluorescent area of the cluster by the mean NP area size.

It has to be pointed out, that this number does not represent the exact number of QDs in the cluster and it is only an approximation. A method to accurately quantify the number of QDs per cluster is suggested in section 3.6. For particles that do not blink, the number of taken up NPs can be quantified by counting the number of NPs that disappear from the surface after a certain incubation time. For QDs it was not possible to use this approach because the number of taken up particles is very small and in the range of QD blinking. That means that the number of particles which are in the dark state at a certain time is comparable to the number of taken up particles and it is not possible to determine how many particles leave the surface.

### 3.3.5 Surface dependent uptake

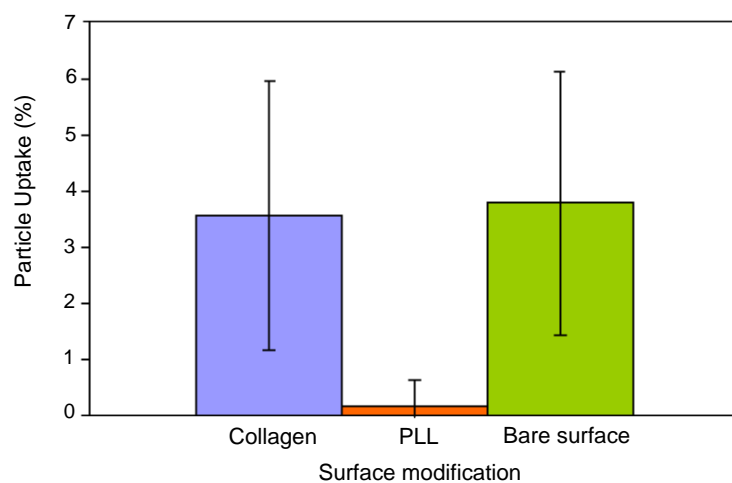
To investigate how the modification of the surface affects NP internalization, surfaces were coated with collagen or poly-l-lysine (PLL) prior to NP immobilization. Figure 3.8 shows the percentage of NPs taken up as a function of the surface functionalization of the microchannel. NP internalization rates show a clear dependence on the surface coating: on collagen 30 out of 900 particles were taken up; on bare surfaces, uptake is at 35 out of 900, while a PLL coating suppresses uptake almost completely (1 particle of 900). Improved NP internalization could be explained in terms of enhanced cell adhesion to the substrate or weaker NP-substrate interactions. None of these effects are expected to happen in the case of collagen, since it neither possesses specific cell adhesion sites nor more negative charge than the bare surface. In the case of PLL, enhanced adhesion is neither expected but uptake suppression has an easy explanation in terms of the electrostatic attraction between the NPs and the surface. NPs are carboxyl-terminated and thus negatively charged in aqueous solution. Collagen- and plasma-treated surfaces are slightly negatively-charged under physiological conditions, while PLL has a strong positive charge. The adherence of carboxyl QDs on PLL surfaces is hence expected to be stronger than on collagen- or plasma-treated surfaces.

Consequently, cellular uptake of NPs can be considered as being controlled by a competition between NP-surface attraction and NP-cell interaction. This assay also proves that surface-mediated uptake involves cellular activity since surface forces and gravity obviously act against uptake.

### 3.3.6 Time dependent uptake: NP exocytosis

Following the internalized NP-cluster count over a longer period of time reveals remarkable fluctuations, which must be attributed to biological activity rather than to image processing inaccuracies. Fig.3.9 shows a time course that clearly indicates a stable increase in NP clusters within the first 5h, after which the cluster count starts to oscillate. While an increase in NP number can be attributed to pure NP uptake from the surface, the reason

**Figure 3.8: Surface dependent uptake.** The percentage of internalized NPs with respect to the number of available NPs in  $z=0$  is represented. NP uptake from surfaces involves cellular activity and can be hindered if the strength of the adhesion between NPs and the surface is high enough.



for the loss of NP clusters is less obvious. Following the total fluorescent area and the total number of fluorescent clusters inside the cell, we can distinguish cluster fusion from cluster loss. During cluster fusion, the total area remains constant and the number of clusters diminishes, while in cluster loss, both observables decrease simultaneously. For this case, we consider exocytosis of NPs as the most plausible explanation. NPs have already been observed leaving cells [59] and exocytosis/endocytosis equilibrium can explain previously reported cell-population averaged saturation curves for NP uptake [57].

## 3.4 Determining NP internalization routes and end-location by TEM

Complementary to the surface-controlled uptake experiments, NP internalization routes and end-location inside cells were studied with TEM. In this case, the reverse approach could not be applied due to experimental impediments. Sample preparation for TEM requires cell cultivation on smooth porous membranes which are not suitable to achieve uniform distributions of NPs on their surface. For these experiments, gold nanoparticles with the same size and surface modification as the QDs were used. The NP-cell interaction is expected to be equivalent for all NPs with the same size and surface modification, independently of the core material. Sample preparation is described in A.6

### 3.4.1 Internalization routes

At the beginning of this chapter it was mentioned that, due to their small size, NPs are expected to enter cells through all endocytotic mechanisms and even to freely diffuse across the plasma membrane. Actually, without any further surface modifications, NPs should be able to enter the cell only via non receptor mediated endocytosis routes such as macropinocytosis. Experimentally it was found that, in effect, several portals of entry

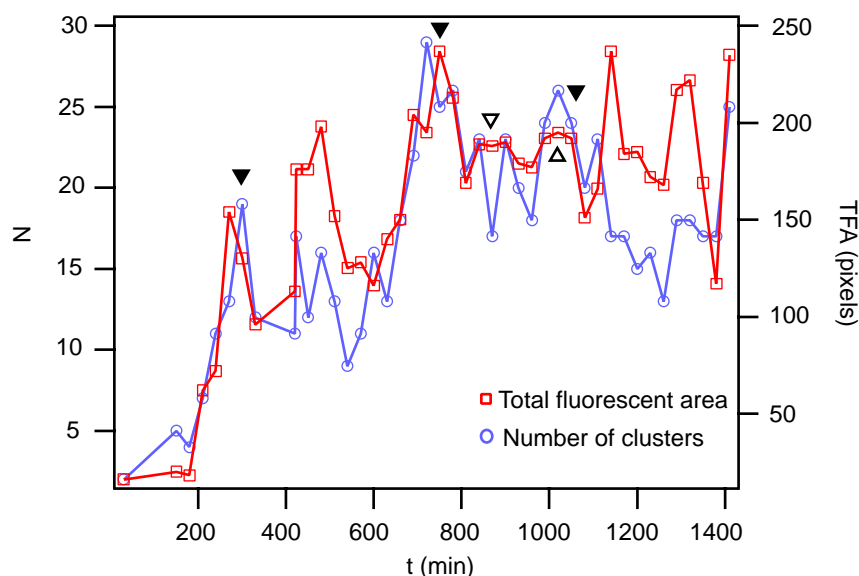


**Figure 3.9: Time dependent uptake.** During the first five hours we observe pure uptake of NPs from the cell surface, with the number of NP clusters and total fluorescent area increasing continuously. Oscillations after this time point can be explained as equilibrium between particles entering and leaving cells (endocytosis/exocytosis). When the number of NP clusters diminishes and the total fluorescent area remains constant (▼) we have cluster fusion, in contrast, when both diminish at a time (△) we have exocytosis.

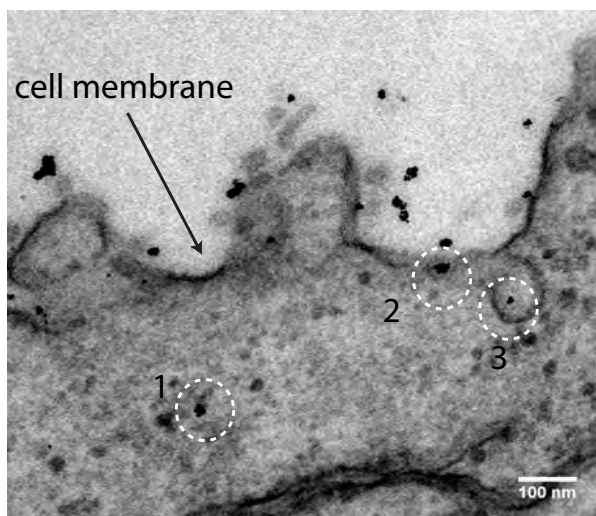
are used. In some cases, NPs that were not trapped in endosomes were observed in immediate proximity of the plasma membrane, indicating possible passive diffusion across this membrane, as shown in Fig.3.10.

Figure 3.11 a depicts the portals of entry into the cells. Figures 3.11 b and c show gold NPs entering the cell via macropinocytosis, figures 3.11 d and e show entry through clathrin and caveolae mediated endocytosis respectively, and figure 3.11 e shows clathrin and caveolin independent endocytosis.

### 3.4.2 End-location inside cells

Once inside cells particles were found trapped in endosomes, mostly free in the cytoplasm, and less frequently forming small clusters free inside the cell nucleus. The histogram in Fig.3.12 a shows the frequency of occurrence of the distinct en-locations inside cells. More than 60% of the particles are found free, without being involved with any membrane, in the cytoplasm, as represented in Fig.3.12 d. Around 20% of the NPs are found trapped in endosomes, see Fig.3.12 b, and 15% are found forming clusters inside the cell nucleus, as shown in Fig.3.12 c. This confirms the results obtained in section 3.3.3 which indicated that NPs without any specific surface modification are able to translocate into the cell

**Figure 3.10: Diffusion through the cell membrane.** This picture shows free NPs inside the cytoplasm (1), NPs that seem to diffuse into the cell (2) and NPs trapped in endosomes (3).



nucleus

## 3.5 Conclusions

In this chapter it has been shown that surface-controlled NP uptake is an efficient and quantifiable approach to study NP-cell interactions, particularly NP uptake. Major advantages of this novel approach are the separation of NP preparation from cell incubation, which prevents NP aggregation in cell medium while allowing well-defined NP number densities presented to the cells, and the establishment of a reference surface, that allows to discern NP internalization. Hence, the reverse uptake assay improves on an important aspect for a standardized toxicity assessment. Making use of this approach made possible to evidence that NPs aggregate after internalization, forming cluster inside cells and that the presence of extra-cellular components at the surface affects cell behavior and thus NP uptake. The fact that some surface coatings hinder NP internalization suggests that this assay could be employed to test the safety of NP coatings in fridges and clothes. In sections 3.3.3 and 3.4.2 it was revealed that NPs, without any for this purpose intended surface modification, are able to translocate into the cell nucleus and can thus interact with DNA. This suggests the possibility of employing NPs as gene carrier vehicles. It was also shown, that NPs are able to enter and exit cells, but there is always a remaining part of them inside them. This observation arises concerns about possible toxicity due to bioaccumulation and related long term adverse effects.

## 3.6 Limitations and solutions

In this chapter, it has been demonstrated that the surface-controlled uptake approach presents important advantages with respect to the conventional manner of studying NP-

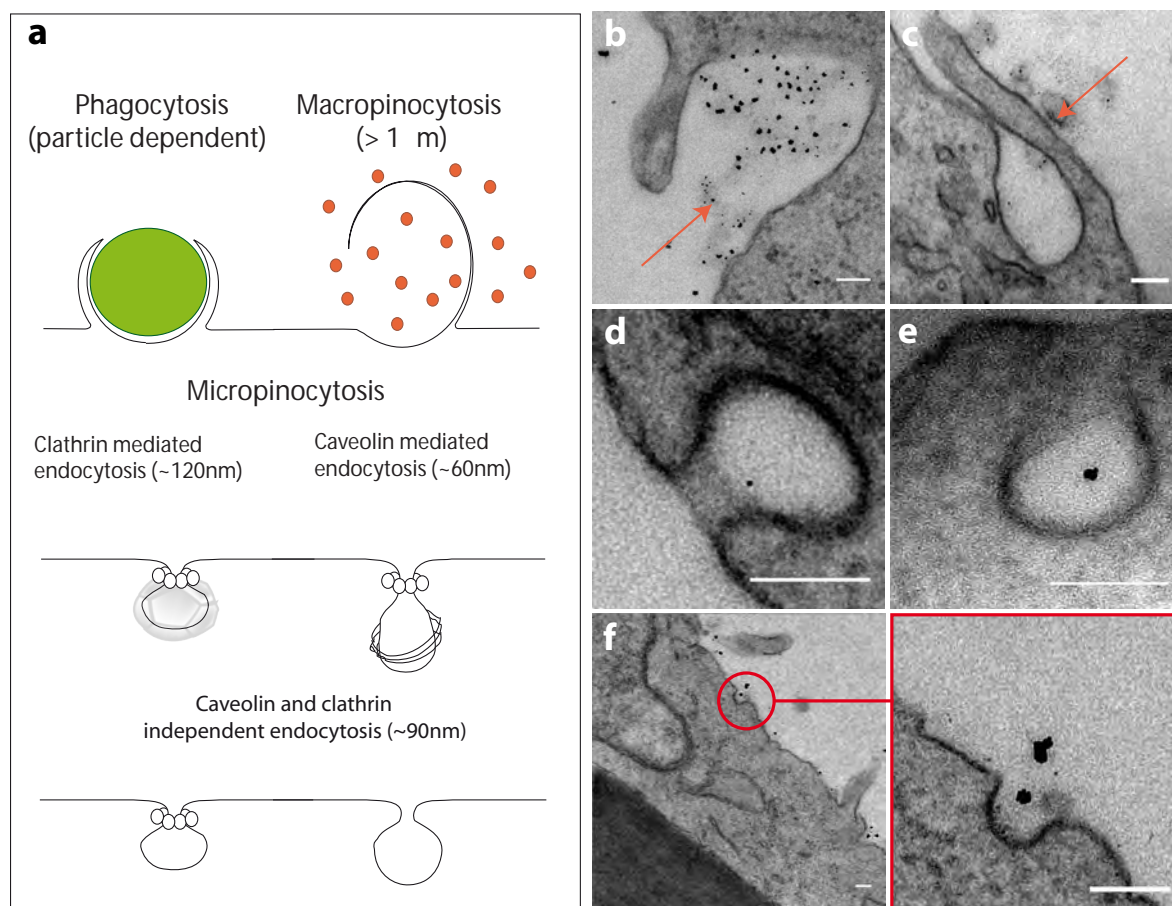


**Figure 3.11: Portals of entry into the cell.** Scale bars correspond to 100 nm.

cell interactions. However, it showed up that QD accurate quantification still remains a challenge. Nevertheless, it is possible to localize single fluorescence point sources with a precision several times greater than the resolution limit of the microscope by means of superresolution microscopy. Promising superresolution techniques in this case are independent component analysis (ICA) [66] and superresolution optical fluctuation imaging (SOFI) [67]. Both techniques are intrinsically similar to fluorescence correlations spectroscopy (FCS), but instead of analyzing the fluctuations of the signal caused by emitters that move in and out of the confocal volume, they analyze the intensity fluctuations of the signal produced by emitters that are spatially fixed but switch between different emission states. Both techniques require non-gaussian emitters that exhibit two different emission states and are mutually independent. QDs are ideal candidates because of their blinking behavior. Since these blinking processes can be assumed to be statistically independent for each emitter, information about each individual fluorophore is encoded in the form of its temporal intensity fluctuations. Both techniques have been successfully applied to separate emitters and localize single QDs immobilized on glass slides [66], [67], and actually

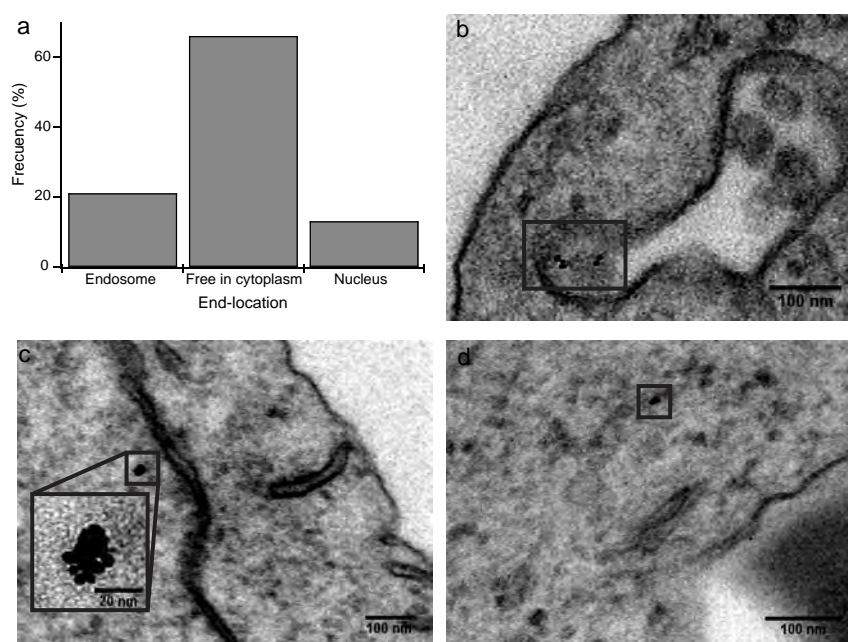


**Figure 3.12: End-location of NPs inside cells.**

SOFI has been employed to generate superresolution images of cells labeled with QDs. All these indicates that both techniques could be easily exploited to quantify the number of internalized QDs in living or fixed cells.





# Chapter 4

## Surface controlled gene delivery

In the last chapter, the surface-controlled NP uptake assay was introduced and it was shown that it offers several advantages with respect to traditional approaches. In this chapter, this method is applied to gene delivery complexes. The process of introducing nucleic acids into eukaryotic cells by non-viral methods is defined as transfection. For a transfection experiment to be successful, gene delivery particles not only have to be taken up by the cells, they have to escape from the endosomes, travel all the way to the nucleus, DNA and transfection reagent have to dissociate and the DNA has to be incorporated in the chromosomes, so that the cells start to synthesize the protein of interest. The whole process is inherently noisy, and thus cell transfection assays are very sensitive to variations in experimental conditions and cell state. There are two classes of noise, intrinsic noise, due to stochastic events during the process of gene expression, and extrinsic noise, due to differences between cells, either in their local environment or in the concentration or activity of any factor that affects gene expression [68]. Extrinsic noise is the primary source of variability in gene expression. This kind of noise can be reduced if uniform and controlled experimental conditions are provided. As it happens with nanoparticles, gene delivery complexes are not stable in cell medium. The consequence of complex aggregation is that cells in the same culture are exposed to different amounts of plasmid-DNA. Here, the surface-controlled approach is applied in order to generate homogeneous and reproducible distributions of gene delivery complexes.

### 4.1 Introduction

The method of reverse transfection was first published by Ziauddin and Sabatini [69] as a microarray-based assay for high throughput screening. In contrast to normal forward transfection, where the DNA of interest is in solution and given together with transfection chemicals on top of cells, in the reverse transfection a solution containing gelatin and the DNA of interest is spotted on a glass surface that later is dried. The transfection reagent is added directly in the samples or alternatively in an additional incubation step interposed before transfection. This microarray of spotted constructs is then covered with a layer of

adherent cells, resulting in the transfection of only cells growing on top of the DNA spots and thus expression of specific proteins in spatially distinctive groups of cells

The advantages of reverse transfection against conventional transfection are:

- the addition and attachment of target cells to the DNA-loaded surface can lead to higher probability of cell-DNA contact, potentially leading to higher transfection efficiencies
- smaller amounts of vectors are needed, what reduces cytotoxic effects
- it is suitable for high-throughput research. One single slide can contain a set of hundreds of different samples, which are all transfected at the same time and under the same conditions

In this chapter, the surface-controlled approach developed in the last chapter for NPs is applied to gene delivery complexes, which are absorbed on a surface in a controlled way. Later, the cells are seeded onto them. In principle, it is very similar to the lipid-DNA method introduced by Ziauddin and Sabatini, but the transfection complexes are not mixed with gelatin and then spotted on a glass surface. Instead, the complexes are absorbed on the surface making use of closed channeled chambers, what avoids the meniscus effect and renders homogeneous distributions of particles and cells. Thus surface-controlled transfection experiments occur under a more uniform environment than reverse transfection and direct transfection experiments, achieving the same conditions for all cells in the experiment. In addition, in the surface controlled transfection experiments, complex preparation is completely separated from cell incubation, what means that transfection complexes can be handled with the adequate buffer for a longer time.

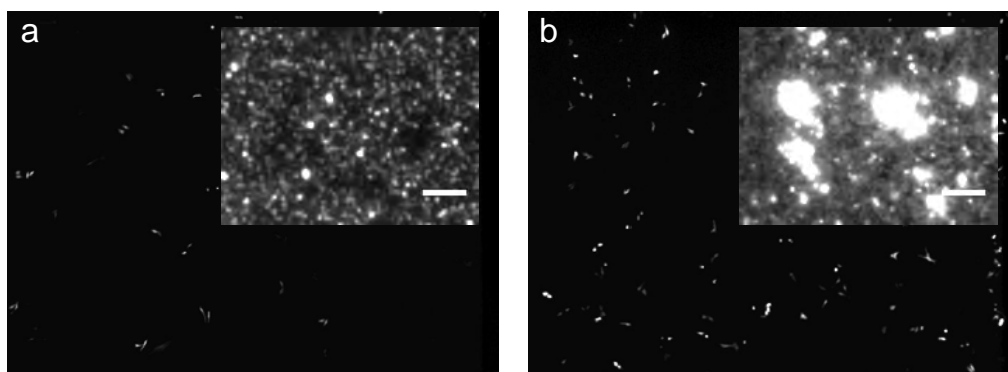


**Figure 4.1: FuGENE<sup>®</sup>/pEGFP-N1 complex polydispersity and transfection rates are buffer dependent.** Fluorescence micrographs showing EGFP expressing cells after transfection and insets showing Cy5-pEGFP labeled complexes. Complexes formed in water (**a**) present significant less polydispersity and transfection efficiency than the same complexes formed in cell growth medium (**b**)

## 4.2 Results

Gene delivery experiments are very sensitive and there is a wide range of factors, such as amount of DNA, transfect reagent/DNA ratio, incubation time, and buffers, which have to be optimized for different cell lines. When using the reverse transfection method, the optimization is even more elaborate, since as we saw in the last chapter, the characteristics of the substrate and the interactions between transfection complexes and this substrate play an important role in particle delivery from it. In all experiments, pEGFP-N1, a plasmid that encodes a red-shifted variant of wild-type GFP and which has been optimized for brighter fluorescence and higher expression in mammalian cells, was used as reporter gene for transfection rate analysis. Transfection efficiency is defined as:

$$\% Transfection = \frac{\text{number of fluorescent cells}}{\text{total number of cells}} \quad (4.1)$$

The experiments were repeated at least two times and the mean efficiency values are shown.

### 4.2.1 Protocol optimization

In this section, reverse transfection protocols for different transfection reagents, FuGENE<sup>®</sup> and l-PEI, and cell lines, Beas 2B and Huh 7, are optimized in order to achieve maximal transfection efficiency.

The first task was to determine which buffer is better suited for reverse transfection for both FuGENE<sup>®</sup> and l-PEI. For both transfection reagents, cell medium rendered higher transfection rates in direct transfection. As can be seen in Fig.4.1, cell medium showed the best results in reverse transfection for FuGENE<sup>®</sup>, even if the complexes showed higher polydispersity.

l-PEI/pEGFP-N1 complexes were made in cell medium, water, HBG and HBS buffer. Which buffer is used for particle formation has a dramatic effect in this case. Only complexes that have been made in HBS buffer are able to reverse transfect cells. When using HBS buffer, transfection complexes can be observed on the surface, as can be seen in Figure 4.2. However, when using medium, water or HBG for forming the complexes those were not visible on the surface and efficient transfection didn't take place.

In figure 4.3 the results of a serie of optimization experiments for reverse transfection with FuGENE<sup>®</sup>:pEGFP-N1 and Huh7 cells are shown. The graphs have to be carefully interpreted since they can lead to erroneous conclusions. The percentage of transfected cells has to be weighted with the total number of adherent cells, since, for example, high FuGENE<sup>®</sup>:pEGFP-N1 ratios can be toxic for the cells, resulting in few adherent cells which are transfected and thus apparently render high efficiency. The major number of transfected cells for the major number of adherent cells (less toxicity) was achieved with a FuGENE<sup>®</sup>:pEGFP-N1 ratio of 9:2 and 400 ngr of pEGFP-N1 per well. The incubation time of the complexes prior to absorption to the substrate has no clear influence in transfection rates. For Beas-2B cells, a ratio of 4:2 rendered higher transfection efficiency.

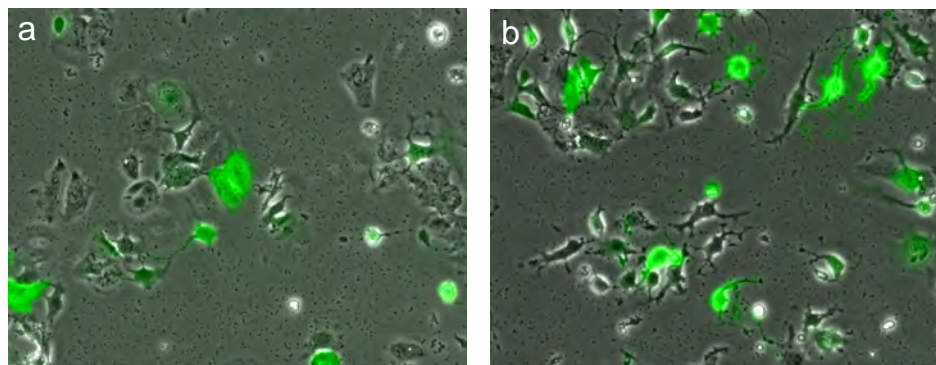


**Figure 4.2: Reverse transfection with l-PEI/pEGFP-N1 complexes.** Successful transfection is only achieved using HBS buffer for complex formation. The gene delivery complexes are observed on the substrate as small black points. **a** 48h. **b** 72h.

Figure 4.4 shows the results obtained for experiments with l-PEI/pEGFP-N1 complexes after 48h of incubation. A N/P ratio of 12 seems to render higher efficiency but the number of impaired cells is very high. For this reason, the ratio N/P=10 was chosen as the best, representing the balance between high transfection rates and low toxicity.

### 4.2.2 Surface dependent reverse transfection

In analogy to the NP surface controlled approach, optimized reverse transfection experiments were performed on surfaces with different coatings.

For FuGENE®:pEGFP-N1 complexes PLL and fibronectin were used as surface modifications. Figure 4.5 shows the transfection rates for three different experiments performed under identical conditions in different days. A fibronectin coating improves transfection efficiency in all cases and a PLL coating reduces it. The fact that the relative behavior between substrates is conserved from experiment to experiment, indicates that the influence of the substrate in successful gene expression is very robust. The absolute transfection efficiency remains variable, indicating that there are still some sources of noise which are not completely controlled.

In the case of l-PEI:pEGFP-N1 complexes, fibronectin and gelatin surface coatings were used. In this case, only one experiment, shown in Fig.4.6, was performed and thus the results are not meaningful. The fibronectin coating seems to slightly reduce the amount of transfected cells, however it reduced the toxicity notably since cells looked healthier in the pictures. Surprisingly, the gelatin coating reduces dramatically the amount of transfection.

## 4.3 Conclusions

In this chapter, the surface-controlled approach was applied and tested in an inherently noisy and thus sensitive system. After optimization and in experiments that assure homo-

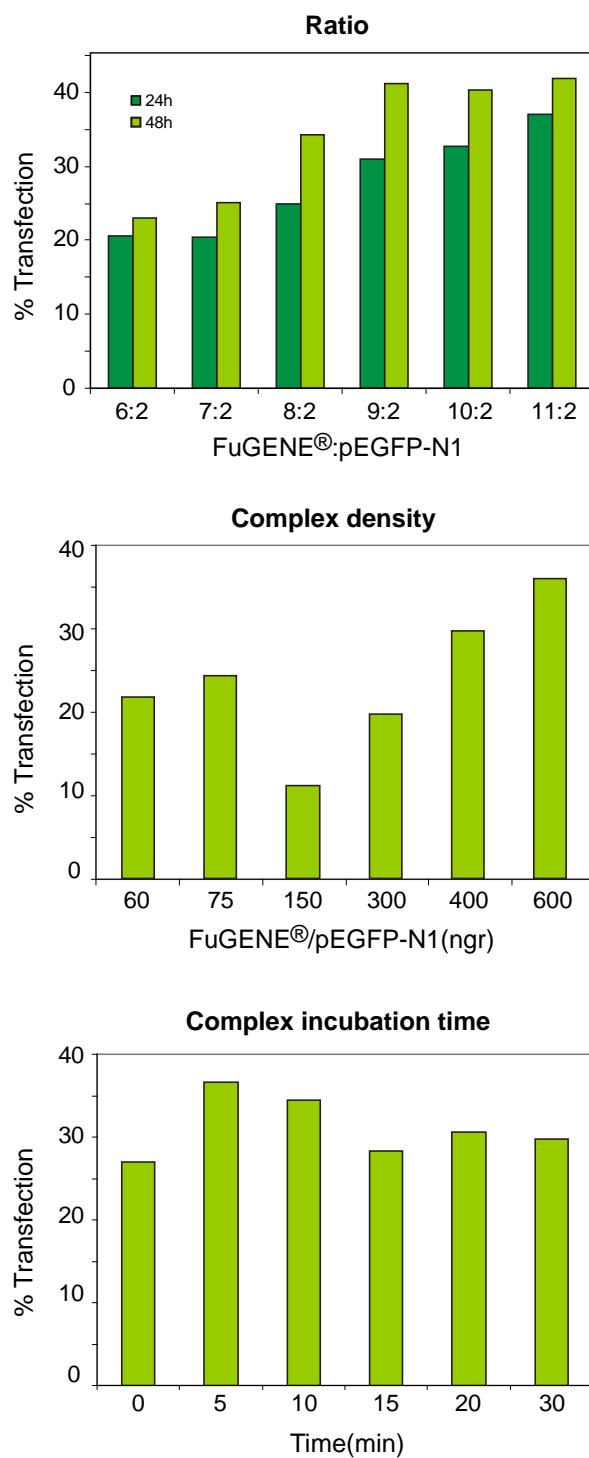


**Figure 4.3: Reverse transfection with FuGENE<sup>®</sup>/pEGFP-N1 and Huh7 cells.** Graphs showing the influence of FuGENE<sup>®</sup>:pEGFP-N1 ratio, complex density, and incubation time on transfection efficiency.

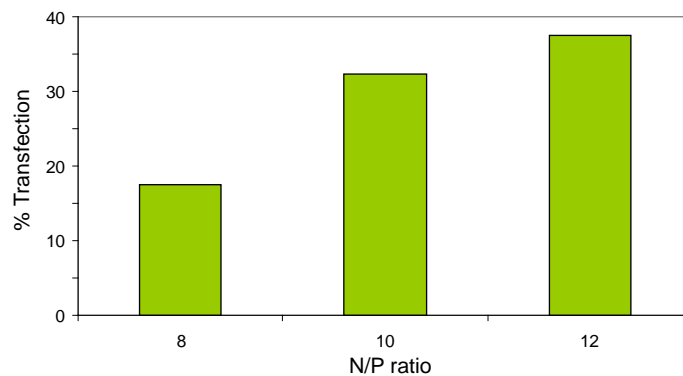


**Figure 4.4: Reverse transfection with l-PEI/pEGFP-N1 and Huh7 cells.** Graph showing the dependence of transfection efficiency with the N/P ratio. A N/P ratio of 10 supposes the balance between maximal transfection and major number of adherent cells (lowest toxicity).

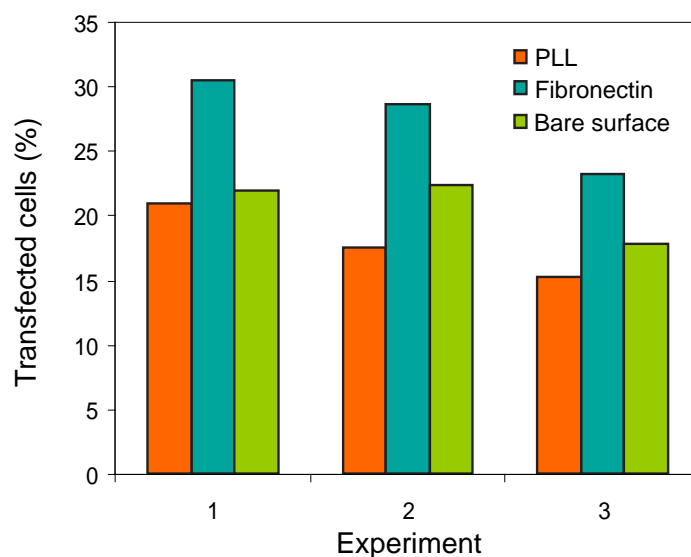


**Figure 4.5: Transfection efficiency dependence on surface modification.** Beas-2B cells were transfected with FuGENE<sup>®</sup>/pEGFP-N1 (4:2) on bare, PLL and Fn coated surfaces. The influence of the surface modification is very robust and thus the relative behavior is conserved from experiment to experiment.

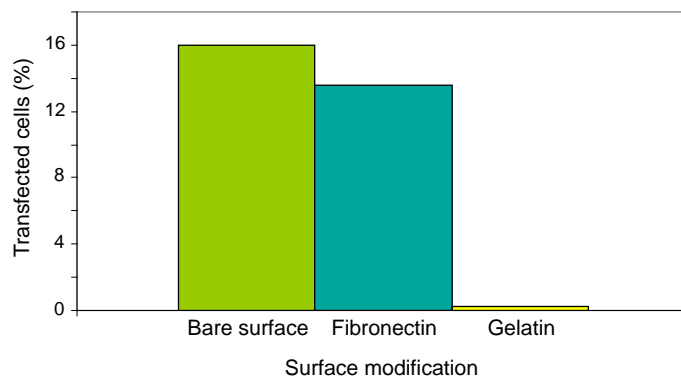


**Figure 4.6: Transfection efficiency dependence on surface modification.** Huh 7 cells were transfected with l-PEI/pEGFP-N1 (N/P=10) on bare, Fn and gelatin coated surfaces. The experiment was performed only once and thus the results are not representative. The gelatin coating deteriorates the gene transfer process notably.

geneous conditions all over the cell population, transfection efficiencies were never higher than 40%.

As in the case of NPs, it appears that the characteristics of the surfaces on which cells grow, determined by the layer of proteins absorbed to it, have a great influence in the outcome of the experiment. In future experiments it should be determined if the different transfection efficiencies obtained for different surface modifications are only due to a reduction/enhancement in complex internalization rates, in analogy to what happens with NPs, or the are other underlying mechanisms.

In this chapter, it becomes evident that complementary to efficiency measurements, cell viability assays have to be performed in order to find out the optimal experimental conditions representing the balance between maximal efficiency and lower toxicity.





# Chapter 5

## Surface patterning techniques

In this chapter, the patterning approaches needed to fabricate the structured substrates used in the following four chapters are described. During the course of this thesis, the limitations of these techniques became evident and continuous efforts were made in order to overcome technical impediments and improve the patterned substrates. However, for the experiments presented in the next chapters only the spatial confinement of cells to defined geometries is needed and the techniques presented here are sufficient. In chapter 10, new patterning approaches which enable better control over pattern geometries and surface modifications are developed.

### 5.1 Microcontact printing

Microcontact printing ( $\mu$ CP) was introduced by Kumar et. al. [70] at the Withesides lab in 1993 and is one of the first and maybe the most important technique used to pattern surfaces and engineer the cellular microenvironment. The working principle is very easy, an elastomeric stamp is formed from a solid template called master. Molecules are immobilized onto this stamp by inking techniques and are subsequently transferred to a substrate by printing. With this simple procedure surfaces with almost any desired geometrical patterns can be created with high precision,  $\approx 1\mu\text{m}$ . For living cell assays, the “empty space” between the patterned regions is generally backfilled with a second molecular system. This backfill is used to passivate those background areas to ensure that the cells adhere only on the patterns [71].

In order to successfully structure a surface, the physico-chemical properties of both surface and ink have to be taken in account. Following the principle “*similis similibus solvuntur*” hydrophobic surfaces are better suited for hydrophobic inks and hydrophilic surfaces are better suited for hydrophilic ones. Proteins, in general, absorb better and irreversibly to hydrophobic substrates, and polymers and other charged molecules, such as DNA and PLL, absorb to surfaces with opposite electrical charge. DNA can also be absorbed onto hydrophobic surfaces by means of the hydrophobic effect, but single stranded DNA is better suited for that [72]. Cells would also preferentially adhere onto hydrophilic

surfaces avoiding hydrophobic ones.

In the case of microcontact printing, the characteristics of the stamp, the surface, and the ink have to be chosen so that the ink absorbs to the stamp, but still the substrate is preferred to the stamp for adhesion. After a serie of experiments, the best results for fibronectin printing were obtained with slightly hydrophilized PDMS substrate, hydrophylized stamps and a Pluronic<sup>®</sup> F-127 backfill (for detailed protocols see appendix ??).

If simple,  $\mu$ CP protocols for cell patterning are tedious, since first the protein of interest has to be absorbed onto the stamp, then transferred to the surface, and last the free areas have to be backfilled with some protein repellent cell molecule, such as PEG, to prevent cell adhesion. Other critical parameters are the pressure applied to the stamp, then to much pressure would distort the pattern, and that the stamp has to be retired very carefully from the surface, since sliding or further contact would lead again to distorted pattern features or unintended double patterning. Given the handicaps of  $\mu$ CP, and especially since all of them, proteins, polymers, and cells can be selectively absorbed to a surface by means of differential wettability or charge, plasma induced patterning was mostly used to structure the surfaces in this work.

## 5.2 Microscale plasma-initiated patterning

The microscale plasma-initiated patterning ( $\mu$ PIP) method was introduced by Langowski [73] in 2005. This novel technique enables to easily create biomolecular micropatterns of varying complexity on several types of hydrophobic polymer substrates. Figure 5.1 depicts the principles of  $\mu$ PIP. A PDMS stamp is used as a mask to preferentially expose or protect areas of an underlying polymer substrate from oxygen plasma. After plasma treatment, the protected regions of the substrate remain hydrophobic while the plasma-exposed areas become hydrophilic. When the substrate is immersed in a biomolecular ink, molecules preferentially absorb to the hydrophilic or hydrophobic substrate regions, depending on the ink characteristics. It is important to point out that in order to create the hydrophilic areas, the plasma has to be in direct contact with the surface, and because of that only patterns of alternative hydrophobic and hydrophilic lines or squares with varying hydrophilicity can be created. Probably for this reason, in spite of its simplicity this method is rarely applied.

### 5.2.1 Plasma induced patterning using a TEM grid as a mask

As mentioned above, the principal disadvantage of  $\mu$ PIP is the given limitation in pattern geometries. To overcome this handicap, the easiest answer is to use stencils instead of PDMS stamps. Hsieh et al. [74] reported an adaptation of the  $\mu$ PIP method using TEM grids as masks. In this way, hydrophilic/hydrophobic patterns are created on a PDMS substrate. Surprisingly, the areas protected by the grid are proclaimed to become hydrophilic while the exposed areas remain hydrophobic. Again, the inconvenient of this method is that only patterns of lines can be created.

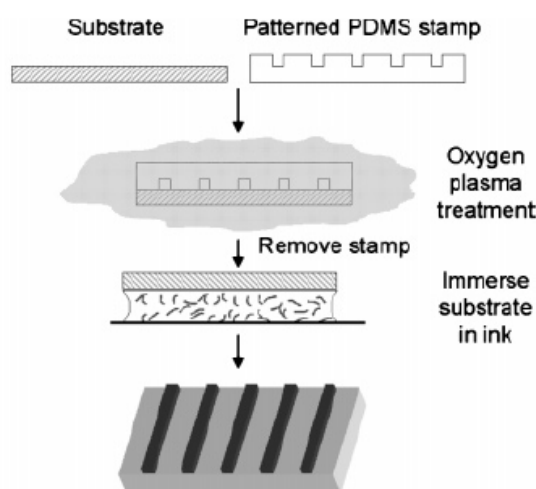


**Figure 5.1: Illustration of microscale plasma induced patterning ( $\mu$ PIP).** A substrate is selectively exposed to oxygen plasma using a patterned PDMS stamp as protective mask. After plasma treatment, the substrate is exposed to a biomolecular ink which adsorb selectively to the hydrophilic parts of the pattern. Reprinted from [73], Copyright 2005, with permission from the American Chemical Society .

Here, a further modification of  $\mu$ PIP method is introduced, resulting in patterned surfaces in which the areas exposed to the oxygen plasma become hydrophilic and areas protected by the grid remain hydrophobic. This method is explained in detail (A.7.1). Figure 5.2 illustrates the working principle of this method. A critical factor for the good performance in this technique is the extent of contact between the grid and PDMS surface, since lack of contact would render protected areas hydrophilic. Exposing the grids to water vapor prior to surface positioning revealed very useful for achieving complete contact. An added advantage of  $\mu$ PIP is that the patterned hydrophilic/hydrophobic surface is at the same time a negatively/neutral patterned surface, that can be exploited for the selective absorption of positively charged polymers and molecules.

Using TEM grids as masks supposes an important improvement since with them it is possible to create hydrophilic islands of different geometries (squares, circles, hexagons, and lines) and it enables creating long range sharply defined micro-patterned surfaces rapid and efficiently. A major inconvenient of the protocol introduced here is that the pattern features, such as hole size and distances between holes, are limited by the finite existence of commercial available grids.

At this point, the patterned hydrophilic/hydrophobic surfaces can be used to directly pattern cells on them, since as mentioned above they will selectively attach onto the hydrophilic islands, as shown in chapter 6. Another inconvenient of this technique is however that the cell surface onto which cell attach can not yet be further modified, and cell adhesion occurs on an undefined surface. The patterned surfaces can also be employed for selective absorption of proteins onto the hydrophobic areas of the pattern. These protein

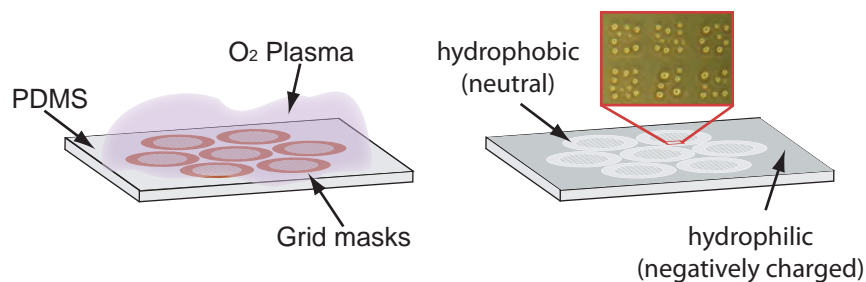


**Figure 5.2: Plasma induced patterning.** In this case, a TEM grid is used as protective mask to selectively expose a PDMS substrate to an oxygen plasma, creating hydrophilic/hydrophobic patterns of desired geometries. Inset shows selective water vapor deposition onto the hydrophilic parts of the pattern.

modified surfaces can however not be used to create patterns of cells, since the cells would attach on both protein coated and hydrophilic areas of the pattern.

Along this work, much effort has been put into overcoming technical hurdles and developing new patterning approaches which are presented in chapter 10.

## Chapter 6

# Oligocellular arrays: towards defined mechanical states

In vitro cell culture is performed either on ensembles of thousands of cells seeded on a relatively large flat substrate or in single cell arrays. Beyond single cell and full tissue level, systems constituted by few cells under defined boundary conditions are good candidates as assays with reduced cell-to-cell variability and maintained cell-cell communication. This chapter institutes the novel concept of oligocellular arrays, which are micron-sized adhesion patches inhabited by few cells under defined boundary conditions. Experiments on Huh 7 cells growing in square adhesive islands with  $\ell \approx 57\mu\text{m}$  are presented. These cells relax into homeostatic packing states, which distribution is observed with high reproducibility. This work was made in collaboration with Karen Alim from the group of Erwin Frey, LMU, Munich.

### 6.1 Cells in confinement arrange into stable packing states

Here, experiments on Huh 7 cells growing on structured thin PDMS films are described. By means of plasma induced patterning (see chapter 5), hydrophilic squares which provide preferred adhesion areas for cell growth are created and the natural characteristics of PDMS are exploited to inhibit cell adhesion in between, see Fig.5.2. When cells are seeded onto the micro-structured surface, they are found to distribute and spread onto the adhesive square patches. Figure 6.1 shows a typical overview of cell populations living in confinement. The number of cells per adhesive area,  $N$ , is random due to the stochastic nature of the sedimentation process (see also chapter 9) and depends on the total cell concentration. The adhesive islands can be thus populated by one, two, three or four cells and, although the size of the adhesive islands was tuned to house no more than four cells,  $\ell \approx 57\mu\text{m}$ , in some cases one island is found to be occupied by up to seven cells.

A single cell per square tries to wet and fill the entire square. However, it will be successful only if it posses enough mass. This may occur when cells are close to cell division.

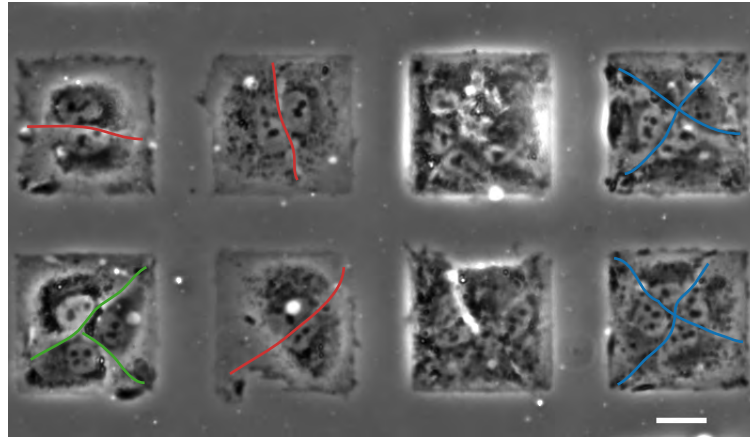


**Figure 6.1: Living under confinement.** Cells are found to distribute and spread onto the adhesive areas. The number of cells per adhesive area,  $N$ , is random due to the stochastic nature of the sedimentation process.

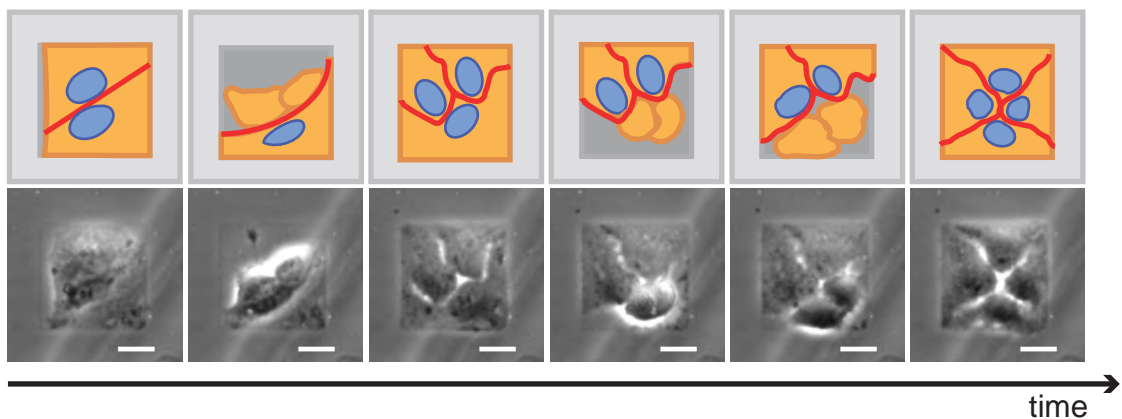


**Figure 6.2: Time evolution.** Cells arrive to the adhesive patch, spread, relax and are able to divide. After cell division, cells reorganize and relax into a new cell arrangement.

In the competitive situation with more than one cell per square, cells are found to arrange themselves into configurations with the total adhesive area being equally shared between cells. We call this configurations *stable packing states*, because they are long lasting compared to the time of cell division and stable state formation. Obviously, with proceeding time, cells will divide, what supposes the most evident perturbation responsible for loss of stable cell packing. When cells divide increase their mass and therefore their need of growth area, what results in increased pressure over the neighbor cells, who are pushed towards the rims of the squares, as can be seen in Fig.6.2. This figure also shows that, after cell division, cells rearrange and relax into new packing states of higher cell number. This cycle continues until the patches become overpopulated and, as revealed by time-lapse microscopy, cells are expelled from the adhesion "islands". Expelled cells are able to crawl over the hydrophobic parts of the patterns and migrate to neighboring empty adhesive islands, as shown in Fig.6.3. Unfortunately, cell confinement *per se* is not enough to trigger contact inhibition of cell division.

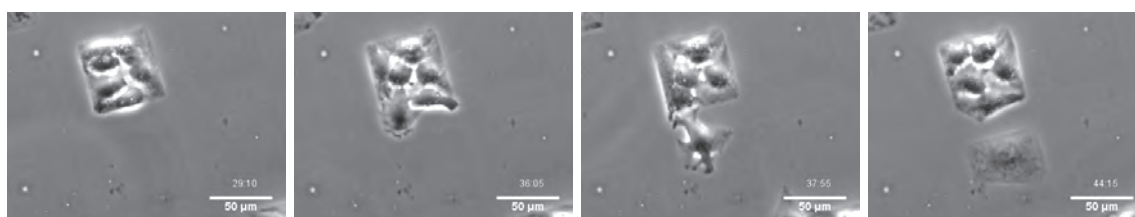


**Figure 6.3: Migration between fields.** Cell confinement into adhesive islands is not enough to promote contact inhibition of cell division. Cells keep dividing until the adhesive islands become overpopulated. Superfluous cells are expelled from the adhesive islands and migrate towards empty patches crawling over the hydrophobic parts of the pattern.

It has to be pointed out that, not all cells are simultaneously in stable packing states, as can be seen in Fig.6.1, since, as just explained, stable packing is affected by cell division. However, the emergence of relaxed packing states after cell division is found consistently over the entire assay and is a reproducible hallmark of the cell array described here. Notice that increasing number of habitants per island increases the probability of cell division and shortens the duration of stable packing states.

## 6.2 Stable packing states

As explained in the last section, cells relax into homeostatic packing states, which distribution is observed with high reproducibility. In the fluorescence micrographs in Fig.6.4, the most prominent packing states are shown. Considering what we said in this section and observing these micrographs, we can conclude that all stable packing states share the following features:

- they are long lasting compared to the scale of cellular processes, as cell division, and stable state formation.
- constituting cells share the available adhesive area equally
- cells show spatial polarisation, evidenced by nuclei displacement towards the centre of the square (and not in the centre of the cells) and polymerized actin at the opposite side, with actin fibers parallel to the rims of the square.
- in some cases nuclei are strongly deformed, as can be seen in Fig.6.7

According to number of cells and symmetry, the stable packing states are categorized in classes as represented in Fig.6.4. Within each class, packing states are sorted from minimal cell perimeter ( $p_{min}$ ), to maximal cell-cell contact ( $c_{max}$ ), as indicated by the arrows.

There is only one possible arrangement for two cells, which lay side-by-side, dividing the square into two congruent areas with the same area and perimeter, marked in light green in Fig.6.4. We denote this class  $2^{II}$ . As can be observed in Fig.6.4 a, the orientation of the cell-cell contact line relative to the square can vary from 0 to 45°. In fact, a broad distribution of angles around a mean value of  $\langle \vartheta \rangle = (21 \pm 13)^\circ$  is experimentally founded. This distribution is represented in the histogram in Fig.6.4 a, where each column comprehends nine degrees.

Three cells face a geometric problem, since it is not possible to divide a square into three congruent parts, sharing the same area, perimeter, and length of contact lines to the neighbors. For this reason, they are obliged to arrange into states non congruent in cell-cell contact, marked in dark green in Fig.6.4 b. There are three possible classes of arrangements,  $3^{II}$ ,  $3^T$  and  $3^Y$ , named according to the shape of the cell-cell contact lines. Fig.6.4 b shows the frequency of occurrence of each class. Surprisingly the  $3^{II}$  states are very rarely observed. In addition we find that there is only one  $3^Y$  state, while for the classes  $3^{II}$  and  $3^T$  the orientation of the cell contact lines relative to the edges of the adhesion square can vary from minimal cell perimeter to maximal cell-cell contact.

Clearly, four cells could arrange into two different classes  $4^{II}$ , with states non congruent in cell-cell contact, and  $4^X$ . However, experimentally, the  $4^{II}$  class is never observed, and the  $4^X$  class appears in a distorted form,  $4_\delta^X$ , where the symmetry is broken because cells avoid the formation of four cells junctions. In this class, cells adopt states where two three cell junctions are separated by a small distance  $\delta$ . By introducing this  $\delta$  distance, symmetry is broken because, arranged in this way, two cells have only two neighbors while the other two have three. The length  $\delta$  of the contact line with the additional third neighbor is short compared to the square length. The experiments show indeed a rather sharp distribution



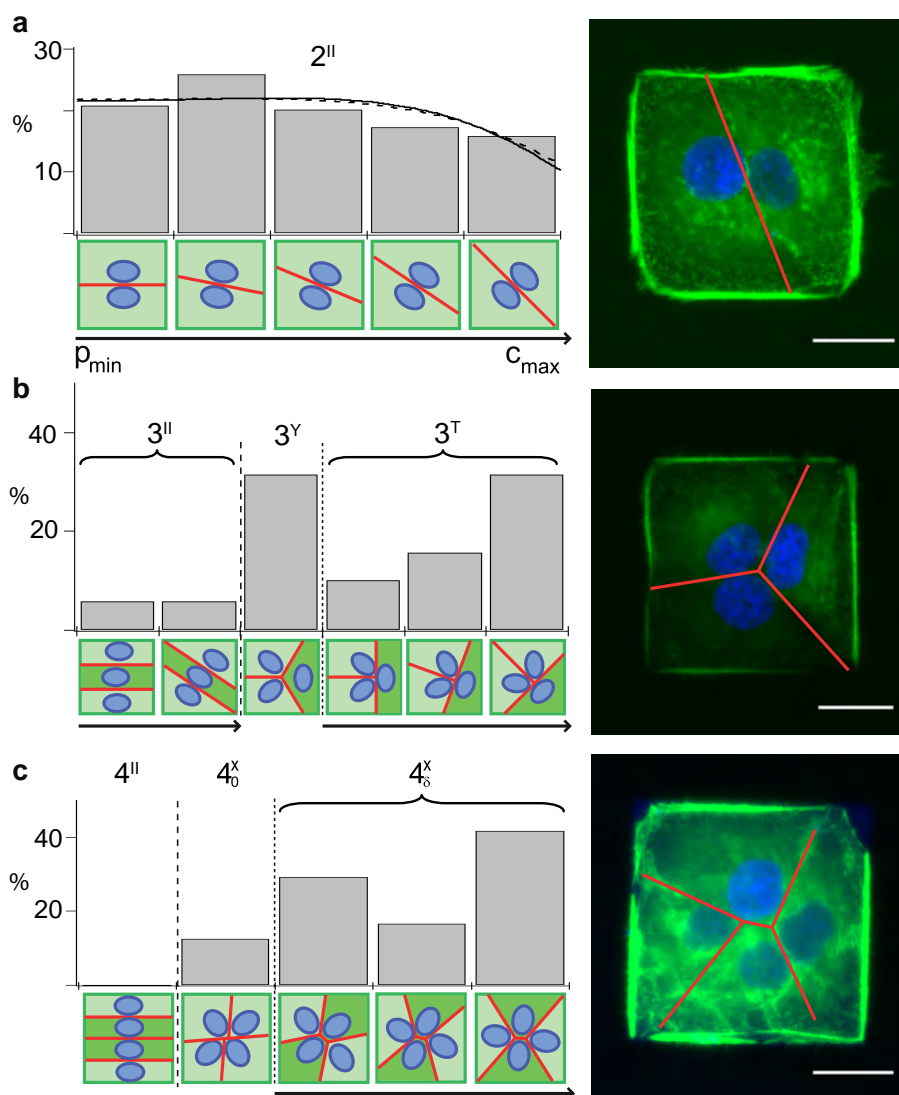
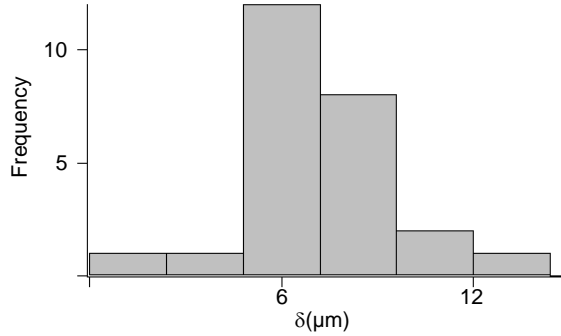


Figure 6.4: Relative abundance of packing states classified by number of cells and symmetry.

of  $\delta$  centered on  $\langle\delta\rangle=(0.12\pm 0.04)\mu\text{m}$ , as can be seen in Fig.6.5. The rare arrangements where the length  $\delta$  is below the resolution limit and could not be estimated are grouped into a class denoted  $4_0^X$ .



**Figure 6.5: Distribution of  $\delta$  distances between 3-cell junctions.** Experimentally, the symmetry of four cell arrangements is broken, since cells avoid the formation of four cells junctions. Instead, cells adopt packing states where two three cell junctions are separated by a small distance  $\delta$ . The experimental distribution of  $\delta$  is very sharp.

### 6.3 Edge-induced planar polarity

As it was mentioned in the last section, an important feature of stable packing states is the asymmetric distribution of cell components, which is a common feature for all packing states. In this section, this spatial polarisation of cells, is discussed in more detail. In order to investigate internal cell organisation, Huh 7 cells expressing GFP-actin were used and cell nuclei were labeled with DAPI.

Among the dense network of actin fibers throughout individual cells, actin stress fibers are pronounced along the edges of the squares. Also cell-cell contact lines show distinct diffuse actin density, which can be attributed to the actin cortex where actin is not polymerized. While a roundish nucleus is placed in the cell centre for a single cell per square, it is always off-centered towards cell-cell contact lines for several cells per square, as observed in the fluorescence micrographs in Fig.6.4 and in Figures 6.6 and 6.7. Nuclei position is independent of cell shape. For example, in the diagonal oriented state of the  $3^T$  class, see Fig.6.7 b, the nucleus is in all cases off-centered towards cell-cell contact lines, being in the corner of a triangular cell in one case and along the edge of a triangular cell in the neighboring cell. Nucleus position is also independent of the geometry of the adhesive patch. Fig.6.6 shows square, circular and hexagonal islands. In all cases, nuclei are displaced towards the cell-cell contact lines, often acquiring their shape.

Nuclei often exhibit a deformed shape, assimilating a form that seems to be dictated by the contour of cell-cell contact lines and reflects cellular shape, as typical for epithelial cells. Deformed nuclei acquire an elongated shape for  $N=2$ , a heart-like shape for  $N=3$  and a triangular shape for  $N=4$ , as can be seen in Figures 6.7 and 6.8.

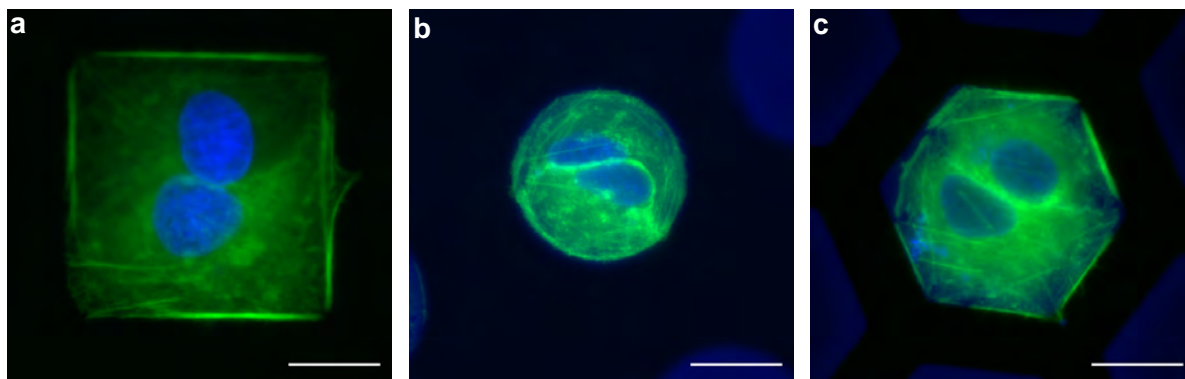


**Figure 6.6: Nuclear position is independent of patch geometry.** Fluorescence micrographs show that on square **a**, circle **b** or hexagon **c**, nuclei are always off-centered towards cell-cell contact lines. In green the actin cytoskeleton of gene modified Huh 7 cells can be seen. The cell nucleus has been stained with DAPI (blue). Scale bars correspond to 20  $\mu\text{m}$ .

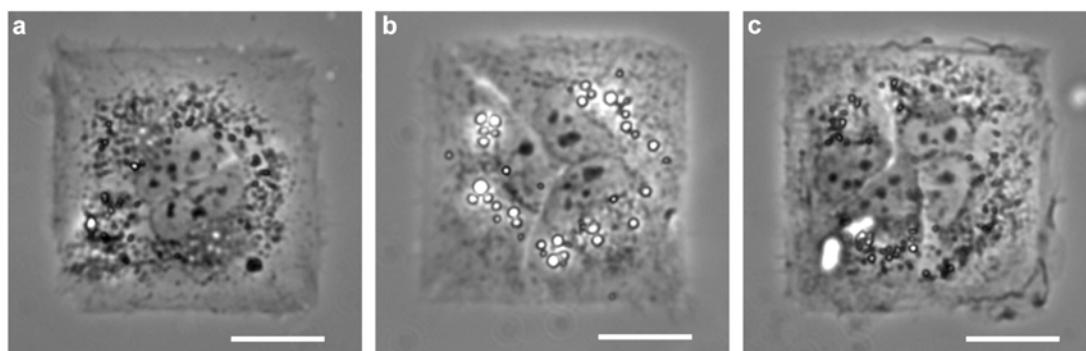


**Figure 6.7: Nuclear deformation.** Phase contrast micrographs showing nuclei deformation following the distribution of cell-cell contact lines for two **a**, three **a** and four cells **c** on a square adhesive patch. Scale bars correspond to 20  $\mu\text{m}$ .

To understand internal structure in packing states we have to remember that apico-basal polarisation is an essential property of epithelial cells, for more details see section 2.1.7, which is triggered by an asymmetric distribution of cell-substrate and cell-cell adhesion points. By creating adhesive islands, we are imposing artificial edges to the cells and creating a lateral surface in the cell, that is different from the other lateral surfaces, due to the absence of cell-cell contacts. The presence of this extra free surface seems to trigger cell polarisation in the plane of the epithelium. Figure 6.8 shows the analogy with apico-basal epithelial polarity.

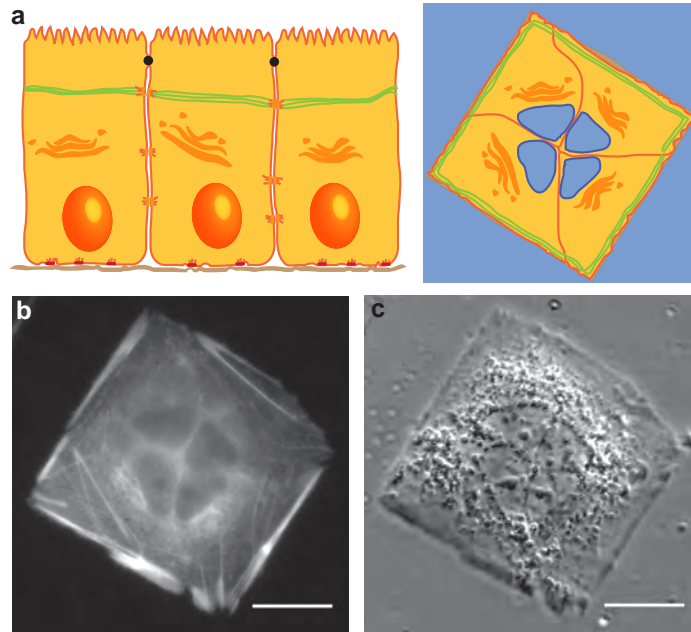


**Figure 6.8: Edge induced planar cell polarisation.** **a.** In analogy to apico-basal polarity, the existence of free edges triggers polarization in the plane of the epithelium. Apico-basal polarity is triggered by an asymmetric distribution of cell-substrate and cell-cell adhesion points. The imposed artificial environment in oligocellular arrays introduces an asymmetry in the distribution of adhesion sites, which triggers polarity in the plane. In both cases, the adhesion free edge is reinforced with actin cables and the nucleus is displaced in the opposite direction. In epithelial cells the shape of the nucleus typically reflects the shape of the cell, as illustrated here. Phase contrast **b** and fluorescence **c** micrographs show the polarized distribution of actin and nuclei in a  $4_0^X$  cell arrangement. Scale bars correspond to  $20 \mu\text{m}$ .

In natural conditions, there is a typical situation in which epithelial cells will encounter an extra free surface: namely a wound. This edge-induced cell polarisation is likely part of the tissue response to wounding and has been already observed in cells along the free boundary of the culture in typical wound healing assays. In fact, a high polarised shape seems to be a prerequisite for the formation of “leader” cells [75].

## 6.4 Discussion

In this chapter, it has been shown that cells in oligocellular arrays relax into stable packing states. The packing state distribution is highly reproducible what suggests to apply theoretical modeling in order to explain the various geometric outcomes as a function of the number of cells  $N$  per square and gain access to mechanisms governing tissue mechanics, what will be done in chapter 7.

Oligocellular packing states exhibit remarkable distinct polarization of the constituent cells. Cell nuclei are off-centered towards neighboring cells and often are even deformed to assimilate the shape of the cell-cell contact line. Recent studies [76], [77], [78] report nucleus position adverse to high focal adhesion density and close to cell-cell contacts. Remarkably all oligocellular arrangements observed here are indeed oriented from cell-cell adhesion sites towards the boundaries of the adhesive patch. This aspect renders oligocellular arrays distinct from locally isotropic polygonal tissue structures and possibly allows to study epithelial planar polarization in more detail. Since polarity is intrinsic to a migrating cell [12] and a hallmark of leader cells [79], oligocellular arrays could represent a useful tool to gain new insights in epithelial collective cell migration, as will be shown in chapter 8.

Oligocellular arrays represent an important advance towards more physiological assays but still with reduced cell-to-cell variability. In oligocellular arrays cell-cell interactions are conserved, permitting cell to interact with the neighbors and the study of epithelial collective phenomena, while simultaneously, the reduced number of cells and the defined boundary conditions impart uniformity and order in the system. Each packing state is constituted by  $N$  cells which present the same area and intracellular distribution, such as nucleus position and actin cytoskeleton organisation. Moreover, an oligocellular array constituted by two cells represents a two near identical cell system with conserved cell-cell interactions. The simultaneous presence of different packing states in an assay should not represent a major problem, since each square can be considered as an independent experiment and packing states of interest can be analyzed separately. Hence, oligocellular arrays may be the basis for standardized toxicity and gene transfer assays with reduced cell-to-cell variability.

The patterned surface presented here exhibits a novel property, if well adhesive islands are preferred for permanent adhesion cells can still migrate over the repellent parts of the pattern. This property invites to study cellular self-organisation into single cell arrays and suggests to look after further surface modifications accomplishing the properties described here. This aspect of oligocellular arrays will be explored in chapter 9.



# Chapter 7

## Oligocellular arrays: a novel approach to study cell mechanics

The fact that cells on the square adhesion sites form reproducible, characteristic and highly symmetric packing states invites to employ oligocellular arrays to study tissue mechanics and to compare the experimental distribution of packing states with the results of theoretical modeling. Theoretical calculations were made by Karen Alim from the group of Erwin Frey, LMU, Munich. A vertex model in which cell packing geometries correspond to stable and stationary network configurations is used for theoretical modeling. Vertex models were introduced in section 2.2.3.

### 7.1 Mechanical equilibrium model of cell packing states

In the following, the current standard vertex model, discussed in chapter 2.2.3, will be applied in order to explain the observed packing states. Since for a certain number of cells all cells present the same area, the model can be simplified introducing the constraint  $A_i = \ell^2/N = \text{const}$ , being  $\ell$  the side length of the adhesive area and  $N$  the number of cells. Homeostatic packing states are then dictated only by the interplay of cell-cell adhesion and cell cortex contractility and described by the minimum of the energy function:

$$E = \sum_{i \in \text{cells}}^N \left\{ \kappa P_i^2 - \alpha \sum_{j \in \nu(i)} L_{i,j} \right\}, \text{ with } A_i = \ell^2/N = \text{const}. \quad (7.1)$$

where  $\kappa$  denotes the cell cortex contractility,  $P$  is the perimeter of the cell,  $\alpha$  stands for cell-cell adhesion, and  $L$  is the length of the cell-cell contact line, as depicted for  $N=2$  in Fig.7.1 a.

Notice that membrane undulations have been neglected and fluctuations are incorporated in the effective parameters  $\alpha$  and  $\kappa$ .

Next, the predictions of this energy function for states with straight cell boundaries are discussed:

Two cell arrangements are described by just a single parameter, the angle  $\vartheta$  between the horizontal axis through the square's centre and the contact line between the two cells, pictured in Fig.7.1 b. Obviously,  $\vartheta = 0, \pm\frac{\pi}{2}, \pi$  is the stable configuration for dominating contractility, as it minimizes the perimeter, while  $\vartheta = \pm\frac{\pi}{4}, \pm\frac{3\pi}{4}$  is the solution for prevailing cell-cell adhesion, because it maximizes the length of the contact line. In general the competition between both contributions is given by the ratio  $\alpha/\ell\kappa$  and the energy minimization leads to a stable configuration with:

$$\cos \vartheta = \frac{1}{\frac{1}{2} \frac{\alpha}{\kappa\ell} - 2} \quad (7.2)$$

Hence, the characteristic angle in cell packing states is directly related to the ratio of cell-cell adhesion and cell contractility strength. The experimental angle distribution for two cells yielded  $\langle\vartheta\rangle=(21\pm 13)^\circ$  and therefore a ratio  $\alpha/\ell\kappa = 6.14$ .

The experiments showed a broad distribution of angles, therefore we argue that the relative probability of finding two distinct packing states with mechanical energy  $E_{S_1}$  and  $E_{S_2}$  is given by:

$$P(E_{S_1})/P(E_{S_2}) \propto e^{-\beta(E_{S_1}-E_{S_2})} \quad (7.3)$$

in analogy to Boltzmann distributed states in statistical physics with an effective inverse temperature  $\beta$ . This approach will prove useful as it allows to rationalize the relative abundance of observed cell packing states, shown in Figure 6.4.

Fitting the experimental angle distribution with this function yields  $\alpha/\ell\kappa = 6.08$  and an effective temperature scale  $\beta = 6.0\kappa^{-1}\ell^{-2}$ . The theoretical distribution function is represented by the solid black line in Fig.6.4 a.

As explained in section 6.2, three cells arrange into three classes of non-congruent packing states:  $3^{II}$ ,  $3^Y$ , and  $3^T$ . Using the value of the parameter  $\alpha/\kappa$  obtained from the case  $N = 2$  for calculating the energies of these states, the  $3^{II}$  state renders 10% lower total energy than the  $3^T$  and hence the mechanical model predicts parallel ordering to be more probable than T-shaped, in contradiction with experimental observations. The assumption that cell states are only governed by cell-cell contact and contractility seems to be too restrictive to describe the prevalence of T-shaped states.

A fundamental difference between the classes  $3^{II}$  and  $3^T$  is the aspect ratio of the individual cells, which are very elongated in the  $3^{II}$  state and rather roundish in the  $3^T$  state, see Fig.7.1 c. This and the fact that Huh 7 cells are cuboidal epithelium cells and thus they natural phenotype should be isometric in vertical section, as depicted in Fig.2.1 b, suggests that the current standard model should be extended to account for cell anisotropy. Defining the size-independent anisotropy of an individual cell as the normalized variance of the eigenvalues  $\lambda_{1,2}$  of the second moment of area, the standard model is extended by an additional term proportional to cell anisotropy with elastic constant  $\epsilon$ :



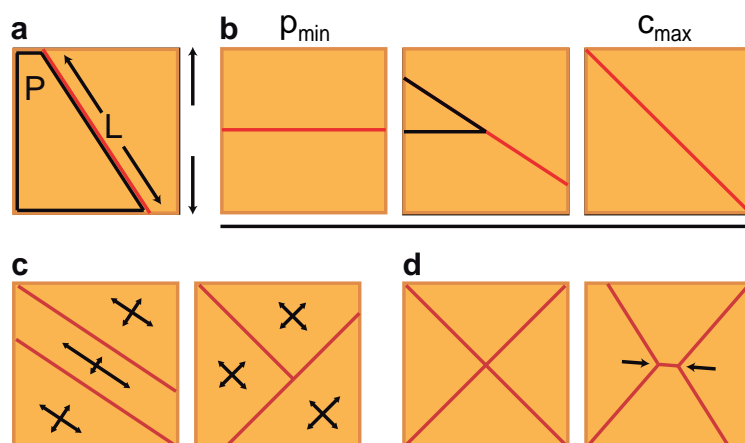


**Figure 7.1: Mechanical model.** **a.** The geometry of a cell packing is described by each cell's perimeter  $P$  and the cell-cell contact line  $L$ . Both measure the contributing mechanical forces. While cell cortex contractility promotes small perimeters  $P$  the opposing cell-cell adhesion favors large cell-cell contact  $L$ . **b.** In the symmetric cell packing of two cells on a square a single angle  $\vartheta$  gives the competition between minimal perimeter caused by cell cortex contractility and maximal cell-cell contact line favored by cell-cell adhesion. The resulting angle depends on the ratio of both contributions only. **c.** While in the  $3^{II}$  class cells are highly elongated they are rather roundish in the  $3^T$  class. Only additional elastic forces that counteract cell anisotropy are able to explain the dominance of the  $3^T$  class consistently. **d.** Four cells on a square arrange asymmetrically with two 3-cell junctions separated a distance  $\delta$  apart. The graphics for  $N=3,4$  cells depict the maximal contact state only.

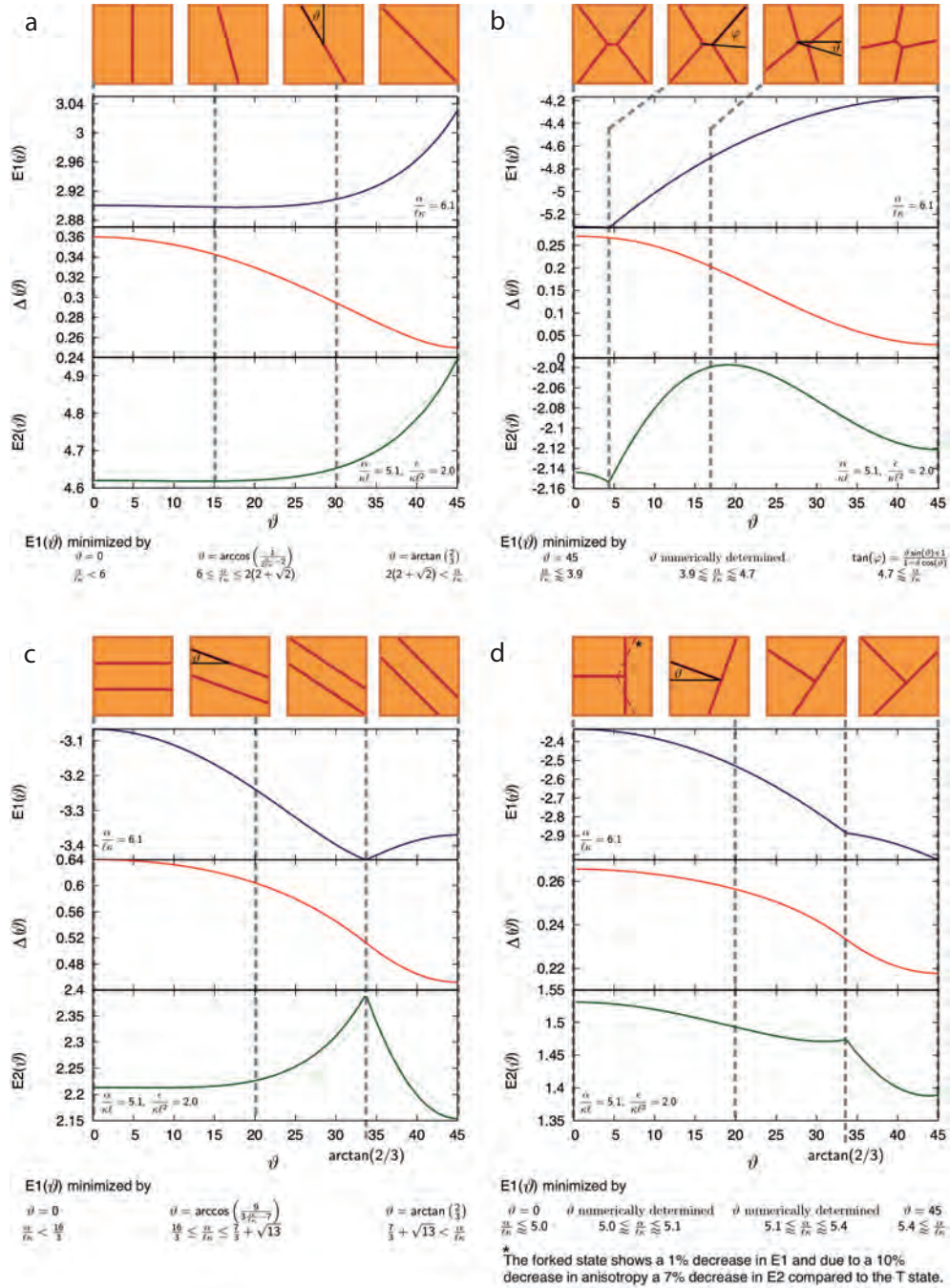


**Figure 7.2: Cell anisotropy and energy landscapes of cell packing states in the current standard and extended model.** These graphs show the energy landscape as a function of the angle  $\vartheta$  predicted by the current standard model,  $E1(\vartheta)$ , and the extended model,  $E2(\vartheta)$ , as well as the contribution of the anisotropy term,  $\Delta(\vartheta)$ , for the classes  $2^{II}$ ,  $4^X$ ,  $3^{II}$  and  $3^T$ . Note that although the qualitative behavior of the anisotropy is similar in all cases, the scale is strongly different.

$$E = \sum_{i \in \text{cells}}^N \left\{ \kappa P_i^2 - \alpha \sum_{j \in \nu(i)} L_{i,j} + \frac{\epsilon}{N} \left( \frac{\lambda_{i,1} - \lambda_{i,2}}{\lambda_{i,1} + \lambda_{i,2}} \right)^2 \right\}, \text{ with } A_i = \ell^2/N = \text{const.} \quad (7.4)$$

The eigenvalues of the second moment of area,  $\lambda_{1,2}$ , are calculated in Appendix B.

Notice that while positives  $\epsilon$  favors cell isotropy, negative  $\epsilon$  promotes an elongated cell shape.

In order to obtain the mechanical parameters for the extended model, the distribution of  $2^{II}$  states is fitted again this time using Eq.7.4. The fitted distribution yields  $\alpha/\ell\kappa = 5.10$ ,  $\beta = 2.1\kappa^{-1}\ell^{-2}$  and  $\epsilon/\ell^2\kappa = 2.0$ . and is represented by the dashed black line 6.4. A considerable small positive  $\epsilon$  renders parallel ordering less probable than T-shaped one, in agreement with experiments. In addition, inside the  $3^T$  class, the energy values predict increasing probability of the packing states with increasing angle, in agreement with observations. Besides qualitative predictions, the model enables quantitative statements, for example predicting  $\sum P(E_{3II})/\sum P(E_{3T}) = 0.2$  and  $P(E_{3Y})/P(E_{3T_{\vartheta=45^\circ}}) = 1$ , in agreement with the experimental distribution of states.

Turning to an arrangement of  $N = 4$  cells, the validity of the extended model may now be further tested. Remember, that as explained in section 6.2, the  $4^{II}$  states are not observed experimentally, and four cells typically arrange in a distorted  $4^X$  class, the  $4_\delta^X$ , where two 3-cell junctions are separated by a small distance  $\delta$ . Experimentally, a bimodal distribution of  $4_\delta^X$  states, with peaks centered around states with maximal cell-cell contact and states with minimal perimeter is observed, see Fig.6.4 c. The current standard model predicts parallel ordering  $4^{II}$  as the most stable configuration, and between the  $4_\delta^X$  states, as shown in Fig.7.2 b, this model predicts a *single stable state*, characterized by maximal cell-cell contact, for the measured  $\alpha/\kappa\ell$ , as most probable. Thus, the current standard model is not able to explain experimental findings. In contrast, the anisotropy term strongly disfavors the  $4^{II}$  states, in agreement with experiments, and the extended model correctly captures a bimodal distribution, since as can be seen in Fig.7.2 b, it energetically favors both configurations, those with maximal cell-cell contact and those with minimal cell perimeter, because both of them exhibit lower cell anisotropy.

Remarkably, the strongly peaked distribution of  $\delta$  distances centered around  $\langle \delta \rangle = 0.12\ell$  can neither be explained with the current standard model nor with the extended model. Both models energetically support a 4-cell junction instead of the observed two 3-cell junctions. This suggests that the mechanical model is not yet complete and further factors need to be incorporated. One intriguing hypothesis is to consider the statistical weight of states, directly related to their statistical entropy, which would clearly favor two 3-cell junctions over the singular state of a 4-cell junction.

## 7.2 Transitions between equivalent stable cell packings

In the last section, the stationary distribution of packing states according to a mechanical energy landscape was described. This section is focused in the dynamics of the two cell system. As outlined in section 6.2, a broad distribution of angles  $\vartheta$  was found experimentally, which allowed the introduction of a statistical weight in section 7.1. Due to the rotational symmetry of the adhesion patch, and the mirror symmetry of the two cells, the energy function has eight equivalent minima, according to eight degenerate stable packing states per patch. Time lapse microscopy revealed fluctuations between equivalent  $2^{II}$  states, see Fig.7.3 a, where a 18h time lapse movie of a two cell arrangement is shown. In Fig.7.3 b the time course of the cell contact angle, for five different two cell systems is represented, showing fluctuation around the mean angle and, in some cases, transitions between equivalent states passing the corners of the adhesion patch. Fig.7.3 c shows the distribution of angles over time, exhibiting a distinct maximum in each quadrant, which corresponds to the mean angle extracted from the  $2^{II}$  packing ensemble shown in Fig.6.4 a and discussed in the sections 6.2 and 7.1. The red line shows the predictions of the extended model. The predicted probability of states matches experimental findings, only states with contact lines extending from corner to corner,  $\vartheta = 45^\circ$ , occur more often than predicted. The fitted time distribution yields  $\alpha/\ell\kappa = 5.12$ ,  $\beta = 10.1\kappa^{-1}\ell^{-2}$  and  $\epsilon/\ell^2\kappa = 2.0$ . Remarkably, the ratios  $\alpha/\ell\kappa$  and  $\epsilon/\ell^2\kappa$  agree with the previous considerations derived from the ensemble distribution in section 7.1. However, the effective temperatures in the ensemble and time average differ. As both averages cover different scales in time, the difference might well reflect distinct stochastic dynamics of the underlying cytoskeletal network.

## 7.3 Conclusions

The observation of distinct classes of highly regular homeostatic cell arrangements suggested to employ the current model of cell mechanics in tissues. This model could not explain the characteristic distribution of cell packing states for two, three, and four cells on a square adhesion patch and was thus extended. An important feature of oligocellular arrays is that the reduced degrees of freedom of the system allow for the full assessment of the entire configuration space.

The case of two cells is charming because it is characterized by the contact angle as the single and easily quantifiable observable that serves to gauge parameters in a mechanical model. While the case of two cells is still well described by the current vertex model [37], [39], [40], [41], [42] the arrangement of three cells on a square is more evolved and adopts more complex cell arrangements. Here, the enhanced abundance of T-states could not be explained consistently within the current vertex model. The model was, hence, extended by introducing an elastic cell anisotropy term. This extended model captures correctly the abundance of the three cell fork state and the bimodal distribution of four cell states.

Another important aspect of the oligocellular array is that all homeostatic states in the different packing classes are subject to considerable fluctuations. The experimental

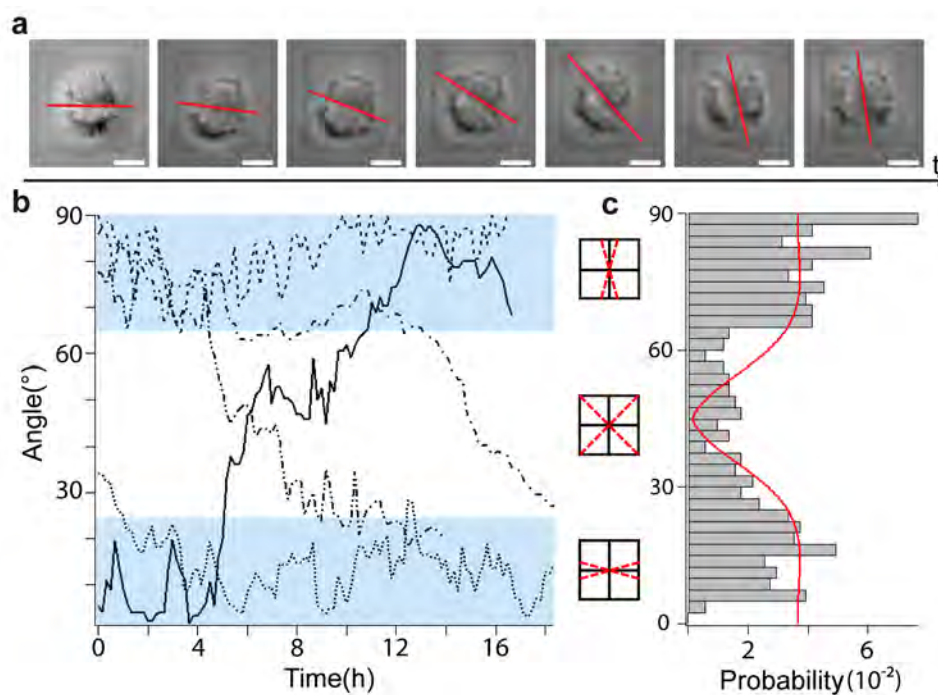


**Figure 7.3: Transitions between equivalent stable cell packings.** Over the course of time cell arrangements fluctuate around their stable state and also undergo transitions to mutually equal stable states related by mirror symmetry along the diagonal of the square, as shown by the time line of phase contrast micrographs **a** and by angle tracking in **b**. The rotational and mirror symmetry of two cells on a square allows for in total eight equivalent stable cell packing states. Following the time line of the angle the cell-cell contact line encloses with the horizontal axis enables the quantification of angle distributions **c**. The observed distribution is in agreement with our extended model predictions, fit shown in red. Scale bars correspond to  $20 \mu\text{m}$ .

distribution of states was fitted in analogy to the Boltzmann distribution and well captured. This yields an "effective temperature" as a measure for the strength of fluctuations. For living cells the effective temperature can be attributed to stochastic dynamics of the cytoskeleton mainly caused by the underlying activity of molecular motors. The modeling approach suggests the intriguing hypothesis that these stochastic fluctuations are strong enough to counteract the elastic forces, thus rendering 4-cell junctions non-existent. However, the fact that internal cell structure could determine the distance between 3-cell junctions can not be excluded. Probable candidates are elastic forces due to the presence of cell nuclei in the proximity of cell contact lines.

# Chapter 8

## Collective cell migration

*In general, an epithelium will not tolerate a free edge.*

H. W. Rand, 1915 ([80])

In this chapter, experiments on Madin-Darby canine kidney (MDCK) cells on  $75\mu\text{m}$  diameter circular islands are described. Because of their reliably epithelial character, MDCK cells are one of the most extensively used cell lines in epithelial cell biology and a major model system for studying numerous epithelial functions. Surprisingly, MDCK cells seeded onto circular adhesive islands do not relax into stable packing states, after a time, they spontaneously start to rotate around the geometric center of the cell system in a coordinated manner. The onset of coordinated cell rotation is a symmetry breaking event. In this chapter, preliminary results regarding collective rotation are presented and symmetry breaking events are investigated. The basis for a theoretical framework for modeling collective cell rotation is proposed.

### 8.1 Introduction

#### 8.1.1 Collective cell migration

During morphogenesis, tumor metastasis and wound healing, cells move together and coordinately change their shape [81], [82]. These cells maintain strong cell–cell adhesion and so the mechanic of these movements displays properties different from those of individual cells. Wound healing assays show that the existence of a free boundary triggers a shape transformation in a subset of cells that become highly motile “leaders”. As seal, leading cells are intrinsically bipolar, as their front faces the tissue substrate while their rear region remains engaged with neighboring cells [79]. Once leader cells are formed, they begin moving outward, normal to the free boundary at a generally constant velocity. Behind the front of cells, submarginal cells respond by moving collectively in complex patterns that resemble the dynamics of a sheared viscous fluid, including the formation of vortices with a diameter around  $100\ \mu\text{m}$  [75](see Fig.8.8). For a long time, the origin of the global

motion, whether it is coordinated by ‘leader’ cells pulling on cells behind or by internal pressure due to cell proliferation and active migration of submarginal cells that would expand cell sheets outwards, remained an open question. Recent studies [81], [83] revealed that the force generation necessary for wound closure is distributed from the wound edge to a distance of at least several cell widths parting from this edge. Moreover, submarginal cells were found to extend ‘cryptic’ lamellipodia basally under cells in front of them and crawl actively against the substratum while maintaining cell-cell contacts and apico-basal polarity [83]. These results suggest the possibility that cells can sense their location in a cell sheet and respond accordingly without being directly adjacent to the sheet edge. Two possible explanations for *positional sensing* are that submarginal cells may be able to generate force and initiate migration by sensing a lowered resistance to movement in one direction, or that the presence of a free edge itself generates signals that submarginal cells also receive. These two ideas are not mutually exclusive, and cells in a sheet may be coupled both mechanically and chemically in terms of motility [81].

MDCK cells seeded in oligocellular arrays exhibit coordinated cell rotation and thus can be employed to study collective cell movements under defined geometries. The patterned substrate imposes artificially defined edges to small groups of cells which can be considered as artificial wounds. The reduced degrees of freedom of the system and its defined geometry allow to better characterize the collective motion of the cells and may help to better understand collective cell migration during wound healing and morphogenesis.

### 8.1.2 Symmetry breaking in collective cell migration

Individual cells on a two-dimensional substrate intrinsically move in a random walk-like fashion. For the emergence of collective cell migration, the isotropy of random walk motility has to be broken and this involves at least a symmetry breaking event [84], [85]. Spontaneous symmetry breaking has already been observed in form of the coordinated rotation of pairs of endothelial cells spatially constrained to an adhesive island. Theoretical modeling showed that three minimal requirements are sufficient for collective rotation to occur:

- spatial constraint of migration
- a long persistence time of the random walk
- physical contact between cells(coupling)

## 8.2 Results

### 8.2.1 Collective rotation

Here, the collective motion of few cells confined in isotropic circular adhesive islands,  $\phi = 75\mu\text{m}$  is investigated. Qualitative and quantitative aspects of the collective movement are described. The objective is to answer simple questions such as:



- does the collective rotation starts immediately after cell spreading?
- there are changes in the direction of rotation? If yes, when do they occur?
- do the rotating cells exhibit any special characteristics?
- is there a preferred direction of rotation?
- is the rotation velocity constant?
- is the rotation velocity dependent on the number of cells per island?

To answer these questions MDCK cells were monitored with time-lapse microscopy during periods of time up to 75h. Experiments show that after a initial period of randomness of around 24h, MDCK cells spontaneously start to rotate around the geometric center of the cell system in a coordinated manner. Rotation can be clockwise and anticlockwise, and also changes in the direction of rotation can occur, as depicted in Figure 8.1. These changes are generally triggered by cell division but occasionally occur spontaneously and, apparently, without external disturbance. Spontaneous changes in the direction of rotation are generally preceded by a brief period of stillness. Huge lamellipodia, with a dimension of several cell lengths, are observed to spread in the direction of rotation surrounding the cell ensemble.

In Figure 8.2, an ensemble of four cells, constituted three marginal cells and a sub-marginal cell, can be observed. Marginal cells exhibit highly polarized shape and well developed lamellipodia, which are typical characteristics of leader cells [81], [75]. Time-lapse microscopy reveals that for effective rotation in one direction, the lamellipodia of all marginal cells have to extend simultaneously in this direction. For better visualization, on the right picture spreading lamellipodia have been marked in black and the direction of spreading is indicated by arrows.

In order to obtain quantitative statements, the position of the migrating cells relative to its initial position was tracked. Figure 8.3 shows the time evolution of three MDCK cells on a  $\phi = 75\mu m$  adhesive island. Taking the middle point of the adhesive island as reference, the angle comprehended by the imaginary line that joints this point with the cell nucleus relative to its initial position is represented. Figure 8.3 a shows the number of turns against the time and Fig.8.3 b shows the same curves but the data have been redimensioned to one turn for better visualization of the coordinated movement. In both graphs, the time intervals in which cells divide have been marked in gray and changes in the direction of rotation are indicated by arrows. In Fig.8.3 b it can be seen that initially cells move in the same direction but still show some randomness. After 24h cells start to rotate coordinately, with the same angular velocity and eventually changing the direction of rotation simultaneously, as reflected by the parallel straight trajectories. Three changes in the direction of rotation, indicated by arrows, can be clearly identified, two of them are triggered by cell division and one occurs without external disturbance.

From a total of 191 observed adhesive islands where rotation arose, 31% rotated anticlockwise, 54% clockwise and only 15% exhibited changes in the direction of rotation.

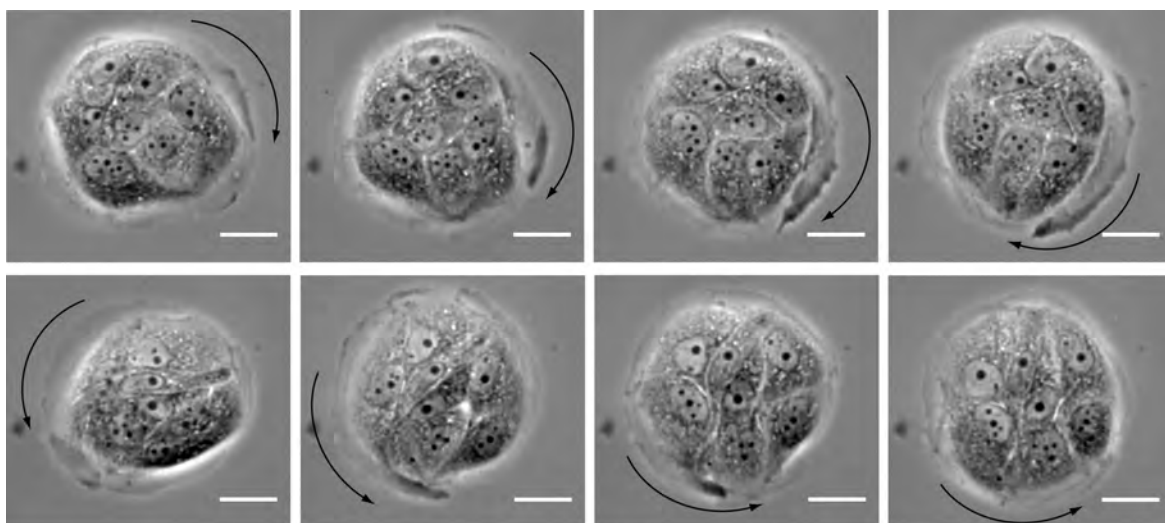


**Figure 8.1: Collective rotation.** Time-lapse microscopy reveals that after a initial period of randomness, MDCK cells spontaneously start to rotate around the geometric center of the cell system in a coordinated manner. The phase contrast micrographs show the collective rotation of an ensemble of seven cells on a  $\phi = 75\mu m$  adhesive island. In the upper row, the cell ensemble rotates clockwise. The same ensemble rotates anticlockwise in the bottom row. The change in the direction of rotation is preceded by a brief period of stillness. Huge lamellipodia, with a dimension of several cell lengths, are observed to spread in the direction of rotation during coordinated movement.

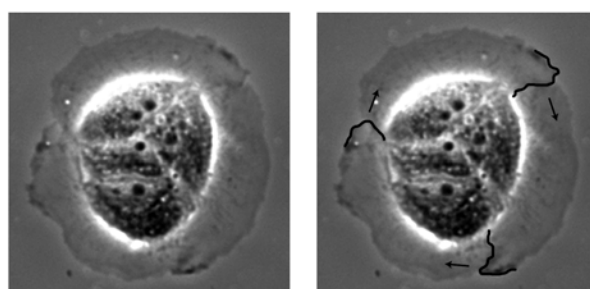


**Figure 8.2: Marginal cells exhibit leader cell characteristics.** In these micrographs, three marginal cells and a submarginal cell are observed. Marginal cells exhibit highly polarized shapes and well developed lamellipodia. For effective cell rotation all lamellipodia have to extend together in the same direction. Spreading lamellipodia have been marked in black and the direction of spreading is indicated by arrows.

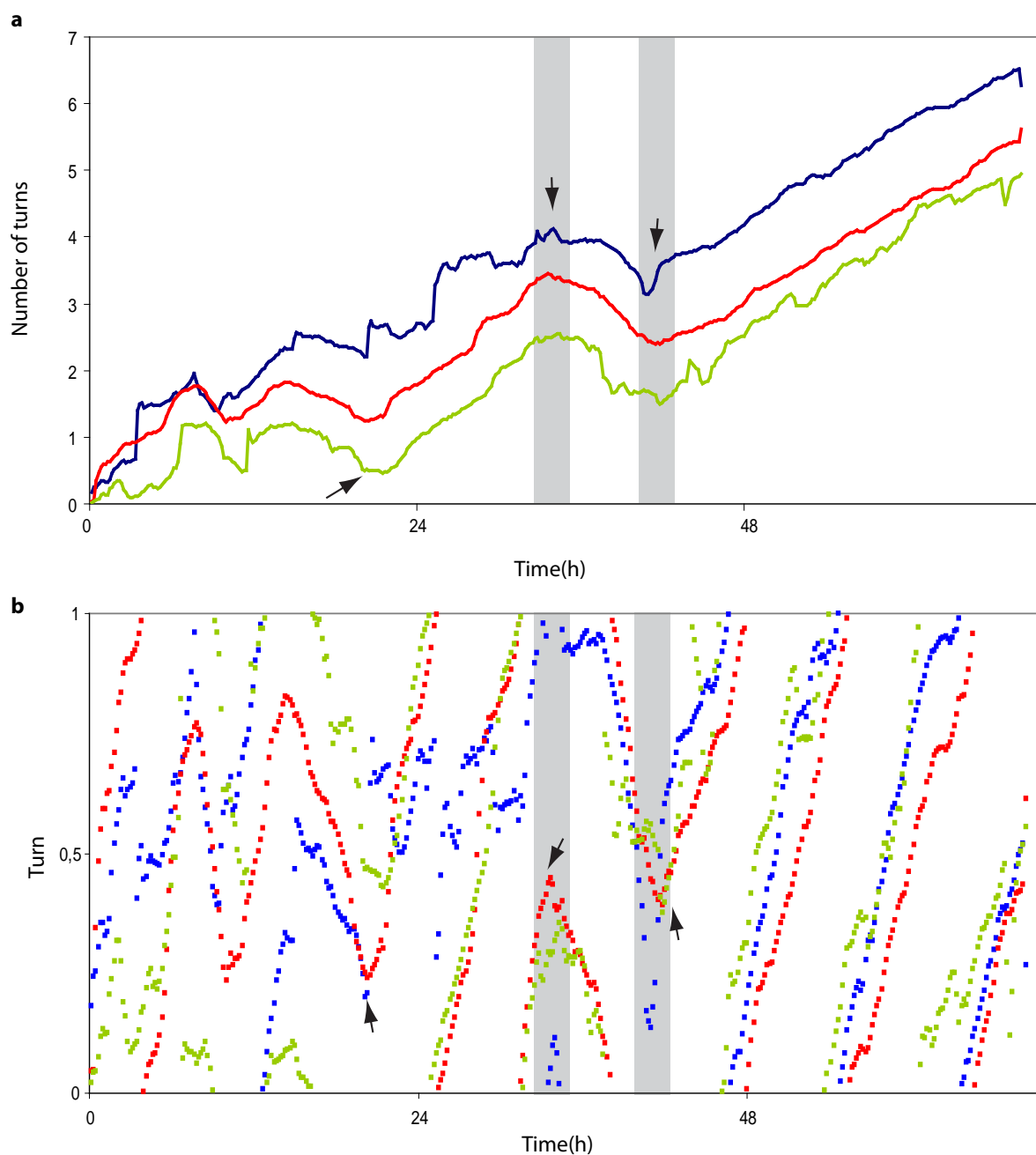


**Figure 8.3: Time evolution of collective rotation.** The time evolution of three MDCK cells on a  $\phi = 75\mu m$  adhesive island is shown. **a** shows the number of turns against the time and Fig.8.3 **b** shows the same curves but the data have been redimensioned to one turn for better visualization. The time intervals in which cells divide have been colored in gray. After a initial period of randomness coordinated cell rotation appears.

This corroborates the fact that the coordinated migration is very robust. The velocity of rotation seems to depend on the number of cells per adhesive island. In figure 8.4, the trajectory of one cell belonging to a group of two cells is compared to the trajectory of a cell pertaining to a six cell group during one turn of coordinated rotation. Fitting the trajectories to straight lines renders a constant average velocity of  $1.5^\circ/\text{minute}$  for the two cell system and  $0.7^\circ/\text{minute}$  for the six cell system. Both velocities are well below the  $3\text{--}6^\circ/\text{minute}$  observed for endothelial cells by Huang et al. [84].

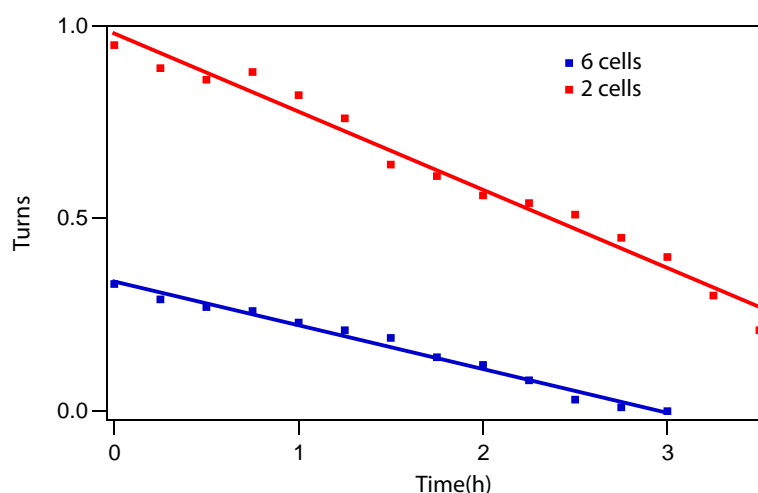


**Figure 8.4: Rotation velocity depends on the number of cells per adhesive island.** A two cell system shows a constant average velocity of  $1.5^\circ/\text{minute}$ . The six cell is heavier and cells rotate with half this velocity.

### 8.2.2 Symmetry breaking events

In this section, the symmetry breaking events are investigated by means of time-lapse microscopy. The behavior of single cells on circular adhesive islands of different sizes is studied.

#### Intrinsic symmetry breaking

A motile cell, which initially has a more or less round shape, can lose its symmetry spontaneously even in a homogeneous environment and start moving in random directions. This involves an intrinsic symmetry breaking event, attributed to polarized forces generated by the myosin motors in the cortical actin network [86], [85]. There are two mutually non-exclusive hypotheses, distinguished by the source of polarity, to explain this directional force. One is that the actin filament substrate for myosin is intrinsically polarized and the other is that asymmetry is provided by an extrinsic source of polarity, for example

asymmetric cell adhesion. The fact that the actin substrate in already migrating cells has intrinsic polarity has already been shown, but the strength of cell–substratum adhesions and cell traction is also asymmetric in cells that have initiated migration and thus the initial cause of asymmetry remains undetermined [85].

Here, GFP-actin expressing Huh 7 cells confined to  $\phi = 35\mu\text{m}$  islands are studied. Epithelial cells constrained to such an island spread covering the entire surface and can not migrate.

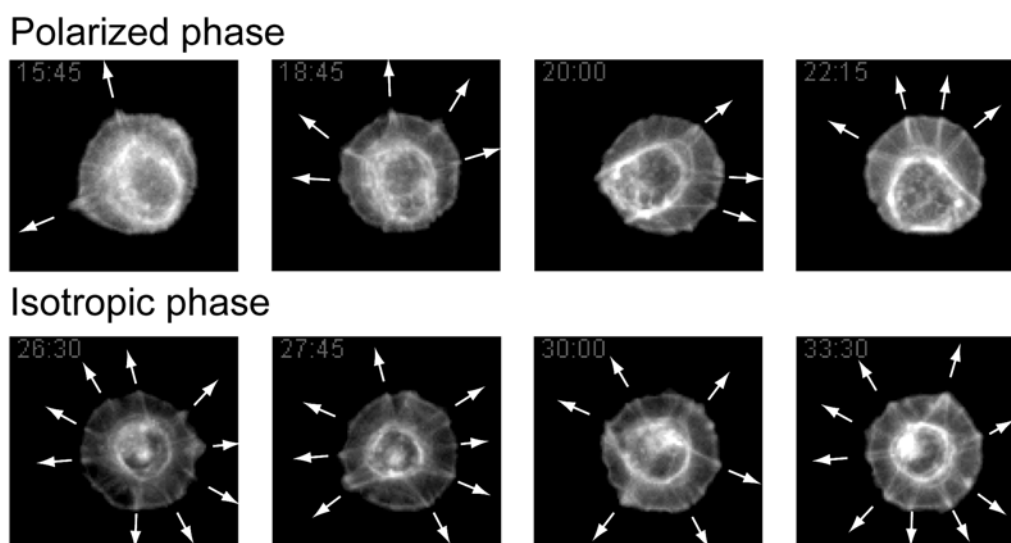


**Figure 8.5: Single cell actin polymerization on a circular adhesive island.** Cells trapped in adhesive island which are smaller than themselves can not migrate. Actin polymerization exhibits two distinct behavior phases. There is a polarized phase, where the cell body is close to one edge of the adhesive island and lamellipodia are extended in the opposite direction and an isotropic phase where lamellipodia are extended in all directions.

Time-lapse microscopy reveals two different phases of cell behavior, as depicted in Fig.8.5. A polarized phase, in which the cell body is close to one edge of the adhesive island and lamellipodia are extended only towards the opposite direction and an isotropic phase, with the cell nucleus in the middle of the cell and lamellipodia being simultaneously extended in all directions. Thus, it can be concluded, that as expected, there exists an intrinsic asymmetry in the cortical actin network.

### Directional symmetry breaking

In a second experiment, epithelial cells were constrained to  $\phi = 75\mu\text{m}$  adhesive islands, which allow single cell migration. Time-lapse microscopy reveals again two alternating phases of cell behavior, shown in Fig.8.6. In the isotropic phase, cells spread and try to cover the entire adhesive area, moving slowly in a random walk-fashion, as shown in Figure 8.7 a.

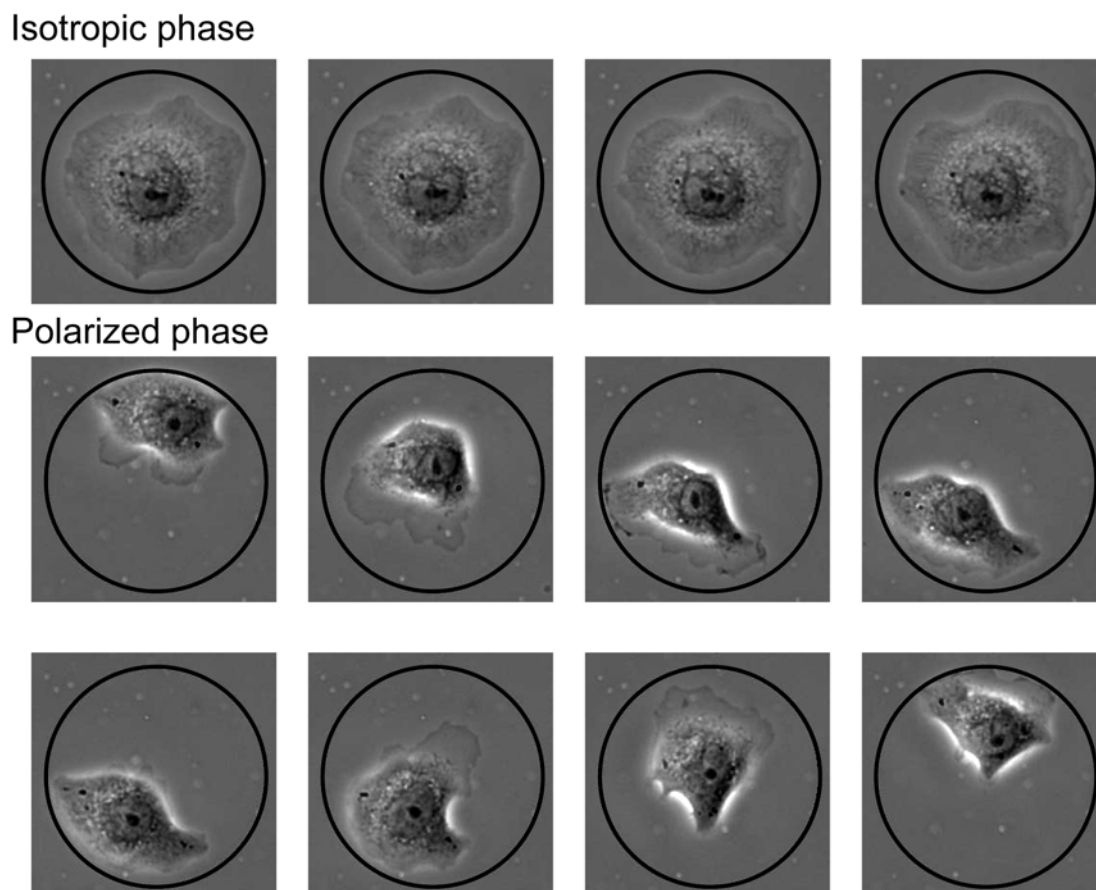


**Figure 8.6: Single cell migrational behavior on a circular adhesive island.** Time-lapse microscopy reveals two alternating phases of cell behavior. The isotropic phase is characterized by fully spread cells which move slowly in a random walk fashion. In the polarized phase, cells exhibit clearly a typical migrating cell polarity, with a front and a back, and move very fast. The barrier introduces a directionality in cell movement causing the cell to move in a loop along one diameter of the circle for long periods of time.

In the polarized phase, cells exhibit clearly a typical migrating cell polarity, with a front and a back, and move very fast. Astonishingly, the direction of polarity is inverted in less than 15 minutes after contacting the edge of the adhesive island. Cells are reflected by this “barrier”, what introduces a directionality in individual cell motion, which loses its isotropic character. The reflected cell moves in the opposite direction of the encountered barrier and becomes trapped during long periods of time in a cyclic movement along one diameter of the circle. This oscillatory behavior is captured in Fig.8.7 b. Cell velocities reach amazingly values, close to  $16 \mu\text{m}/\text{minute}$ , during this phase. For comparison, fibroblasts move at up to  $1 \mu\text{m}/\text{minute}$  [87], enhanced myoblast migration (almost 3 times faster than normal) reaches also  $1 \mu\text{m}/\text{minute}$  [88] and MDCK cells migrating at the leader edge of a wound reach maximal velocities of  $0.3 \mu\text{m}/\text{minute}$  [89]. Since the presence of an edge have been shown to be in itself a signal that causes activation of the epidermal growth factor receptor [90], which in many epithelia is a central event in induction of motility, this cell behavior could be explain as a feedback loop.

### Edge-induced symmetry breaking

In chapter 6 it was evidenced that the presence of an edge triggers cell polarisation in the plane of the epithelium. For the establishment of this polarization it is necessary that both, neighbor cells and a free side are present. This supposes a third symmetry breaking event.

### 8.2.3 Planar cell polarity, edges and collective movements

Here two possible not mutually exclusive causes for biochemical *positional sensing* are proposed. First, as already mentioned, the presence of an edge in itself generates a signal that causes activation of the epidermal growth factor receptor, EGF, [90] which in turn is a central event in induction of cell motility. *Positional sensing* could thus also be explained in terms of a gradient of epidermal growth factor that is produced by marginal cells and diffuses inside the tissue inducing cell motility in submarginal cells. Second, it has been shown that the presence of edges triggers polarization in the surface plane. This polarizing signal could be transmitted from the border cells to submarginal cells, which become accordingly polarized, in analogy to planar cell polarity signaling (PCP) (see section 2.1.7). The polarizing signal triggered by the presence of a free edge would be then responsible for *positional sensing* in submarginal cells and cell migration beginning. Theoretical modeling of PCP [31] has shown that starting from a randomly distributed PCP configuration, defects in the form of vortices remain after system equilibration. Figure 8.8 b shows the equilibrated system of polarity vectors and its striking similarity with the velocity fields of migrating cells in a wound healing assay, depicted in Fig.8.8 a. The wound induces cell polarization in the direction perpendicular to it and cells start to move outwards in this direction (parallel or antiparallel to the direction of polarization). If the tissue was initially not polarized or polarized in another direction, polarization has to be reordered to point in the direction of the new polarizing signal, and defects appear in form of vortices,

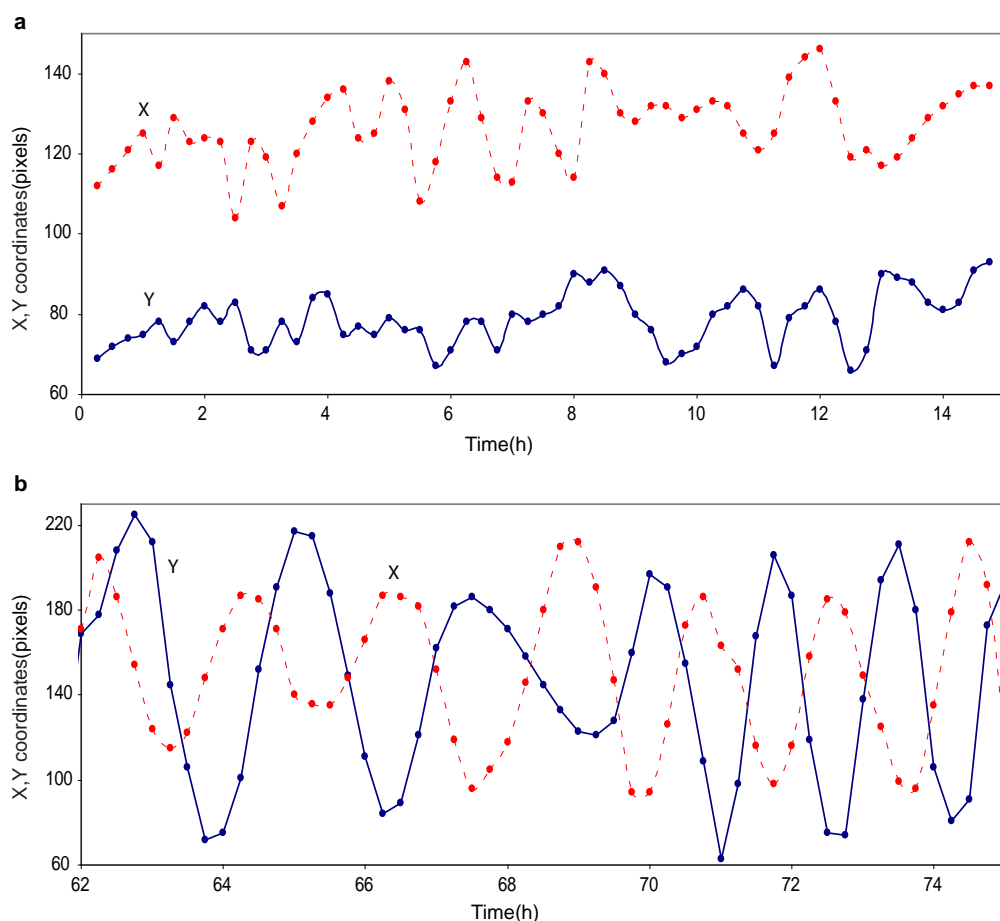


**Figure 8.7: Symmetry breaking by confinement.** Graphs representing the coordinates of cell movement versus the time. Constriction of cell migration breaks the symmetry of the cellular random walk, shown in **a** and introduces a directionality in cell migration. The cell moves in opposite direction of the encountered barrier. Being confined in a circle, cell movement becomes cyclic, with the cell moving in a loop along one perimeter of the circle during long periods of time, as shown in **b**.



in analogy to Fig.8.8 b. This vortices could explain the vortices observed in the velocity fields of migrating cells in wound closure assays. The fact that epithelial wound repair is regulated by the PCP signaling pathway [91] supports this hypothesis.

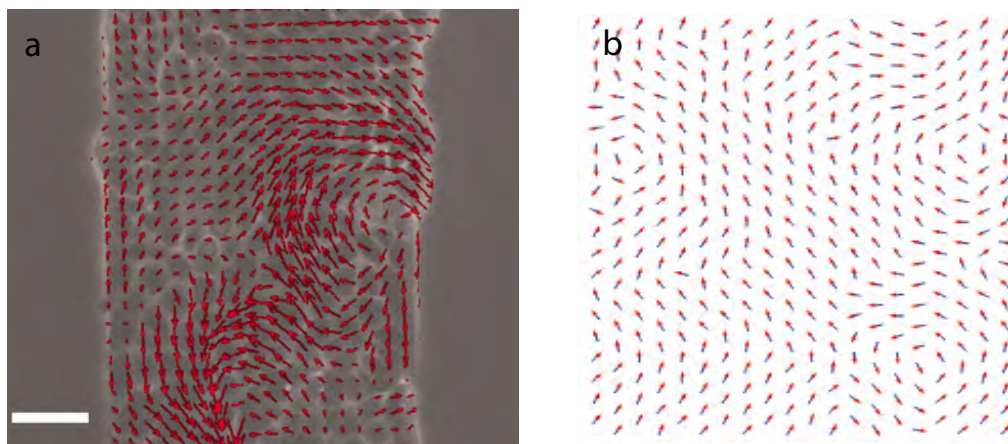


**Figure 8.8: Velocity and planar polarity vector fields in epithelia.** **a** Reproduced from [75], Copyright (2007) National Academy of Sciences, U.S.A. The experimental velocity fields obtained in wound closure assays exhibit striking similarities with the distribution of planar polarity vectors obtained from theoretical modeling of PCP starting from a randomly distributed configuration [31], shown in **b**.

This hypothesis can be used to explain the onset of rotation in circular adhesive islands and the extension of huge lamellipodia in the direction of rotation. Cells in small circular islands receive to opposite polarizing signals, the one generated by the presence of the edge and one transmitted by the neighboring cells, which points in the opposite direction, as sketched in Fig.8.9 for the case of two cells. Each cell responds to this signals trying to move in the correct position, between the edge and the neighbor cell and creates a vortice which is unstable.

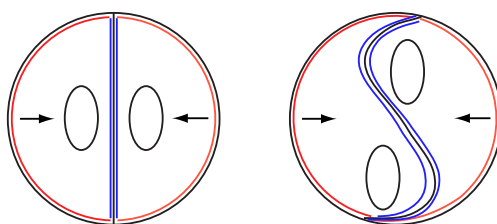


**Figure 8.9: Opposite polarizing signals could be responsible for collective rotation.** Cells in small circular islands receive to opposite polarizing signals, the one generated by the presence of the edge and one transmitted by the neighboring cells, which points in the opposite direction. Each cell responds to this signals trying to move in the correct position, between the edge and the neighbor cell and creates a vortice.

### 8.3 Conclusions

In this chapter, the collective rotation of MDCK cells in circular adhesive islands has been studied. It has been shown, that cells rotate with constant velocity which depends on the number of cells per island, decreasing with increasing number of cells. Changes in the direction of rotation occur mostly in correspondence with cell division events but can also occur spontaneously. Spontaneous changes in the direction of rotation reflect the fact that oligocellular tissues are subjected to considerable fluctuations, as it was shown in chapter 7. In this chapter, the strength of these fluctuations was captured as an "effective temperature" of the cell system.

Three symmetry breaking events have been identified: the intrinsic asymmetry the cortical network, a contact-induced persistence of cell migration and cell polarization in the plane of the epithelium, manifested by the position of the cell nucleus.

Two possible not mutually exclusive mechanisms of biochemical *positional sensing* have been proposed. In one hand, the polarizing signal generated by the edge could be transmitted from cell to cell, in analogy to PCP, giving positional information to submarginal cells in wound healing assays and being the origin of collective rotation in circular oligocellular tissues. In the other hand, a gradient of epidermal growth factor, produced by marginal cells and diffusing inside the tissue, would also give positional information to submarginal cells and could induce cell motility several rows behind the wound. The combination of this two mechanisms would assure that each cell in the tissue receives positional information but the signal inducing motility, in form of a EGF gradient, is damped far away from the wound.

In order to validate these hypothesis, further experiments and theoretical model are necessary. Theoretical modeling should take in account all possible mechanisms of *positional sensing* mentioned here. Submarginal cells may sense a lowered resistance to movement in one direction and/or biochemical signaling in form of PCP signaling or epidermal growth factor gradients could give directional information. Theoretical model of PCP already exists in the form of vertex [31] and reaction diffusion [92] models. These models are for equilibrium systems and should be adapted for dynamic systems with adequate boundary conditions. Experiments with cells expressing GFP-tagged proteins involved in polarization processes would help to discern if actually the polarizing signal triggered by the presence of edges *per se* can be transmitted from cell to cell. It would be interesting to find out the range of action of this polarizing signal. This task could be accomplished using adhesive islands of increasing size and cell expressing proper GFP-tagged proteins.

While in the last chapter, human hepatocarcinoma cells, Huh 7, relaxed into stable packing states, here, MDCK cells contradictorily exhibit collective rotation. Since theoretical modeling showed that cell-cell coupling is a minimal requirement for the establishment of collective rotation [84], the differences in the behavior of these cell lines could be explained in terms of differences in cell-cell adhesion. Cancer cells are known to exhibit less cadherin expression and thus the level of cell coupling may be insufficient to efficiently promote collective movements.

# Chapter 9

## Cellular self-organisation in single cell arrays

In this chapter, for the first time, the fascinating possibility of creating a single cell array by cellular self-organisation is explored. Cellular self-organisation on a patterned substrate requires that if well adhesive islands are preferred for permanent adhesion cells can still migrate over the repellent parts of the pattern. In chapter 6, hydrophilic/ hydrophobic patterned PDMS was proved to be an optimal substrate for this task. Here,  $\mu$ CP is applied in order to create alternative patterned substrates accomplishing these characteristics.

### 9.1 Introduction

Single cell arrays are interesting because they enable to quantify the distribution of behaviors amongst a population of individual cells under uniform conditions. This is important because parameters that are measured as averages of large populations can be misleading. For instance, an apparently linear response to a signal could, in fact, reflect an increasing number of cells in the population that have switched from “off” to “on”, rather than a graded increase in response by all the cells [93]. Gene expression, for example, involves a series of single molecule events and belies a deterministic description. As each of these molecular events is subject to significant thermal fluctuations, gene expression is best viewed as a stochastic process. Even in cases where population measurements are regular and reproducible, single-cell measurements display significant heterogeneity [4], [2]. Another advantage of single cell arrays is that automated image analysis becomes much easier, since cells are confined to predetermined positions and exhibit fixed shapes enabling high-throughput analysis of single cell behavior.

The most common approach to generate a single cell array on a previously microstructured surface is to seed cells in excess onto it. After a short incubation time, the pattern is rinsed in order to eliminate overabundant cells. The difficulty lies in adjusting the initial concentration of cells, so that after the washing process only one cell per adhesive spot is left. Due to the stochastic nature of the sedimentation process, the initial distribution

of trapped cell numbers per adhesive island is highly dependent on cell seeding density. Studies using single cell array systems have shown that the numbers of trapped cells per adhesive spot follow a Poisson distribution [94] and that not more than 40% of the adhesive spots are occupied by single cells. So, the single cell array results in a combination of adhesive islands containing a broad distribution of numbers of cells, as shown in Figure 9.1. A possible choice to the rinsing method would be positioning every single cell of the array onto the correspondent adhesive island by means of inkjet printing. Here, for the first time, substrates that promote cellular self-organisation in single cell arrays are created.

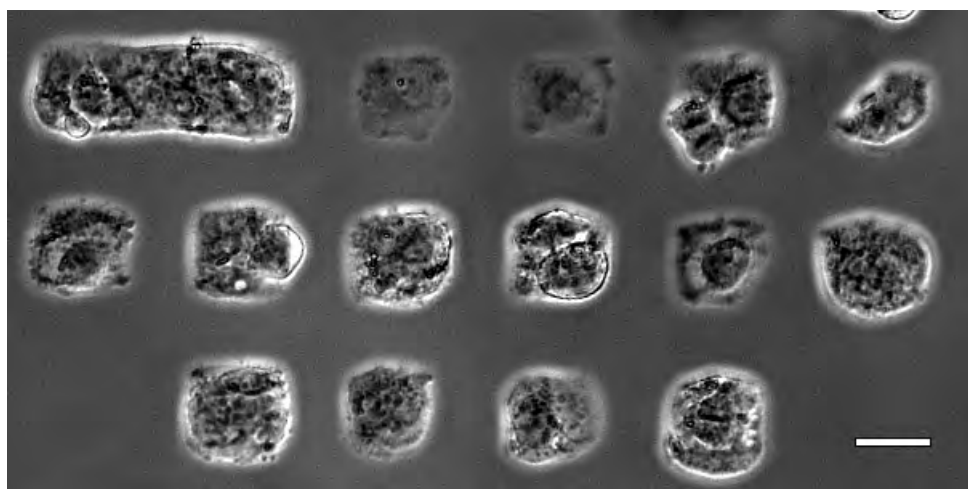


**Figure 9.1: Single cell array.** Due to the stochastic nature of the sedimentation process, seeding cells in excess onto a patterned surface leads to a broad distribution of numbers of cells per adhesive island.

## 9.2 Musical chairs: single cell arrays by cellular self-organization

In chapter 6 it was demonstrated, that cells confined to the adhesive parts of a patterned PDMS surface are able to crawl over the hydrophobic areas if they are expelled from the adhesive islands. This substrate property is rare and simultaneously charming. It is rare, because cells are not fussy and if the surface offers a minimal chance for adhesion, cells will adhere to it. It is charming because it invites to play *musical chairs* with cells and study their self-organisation on the substrate, as well as to explore novel surface modifications which support cell crawling but not permanent cell adhesion. Figure 9.2 shows a sequence of pictures illustrating self-organisation of cells on a structured PDMS substrate. Free standing “chairs” have been outlined in white and the directions of cell migration have been marked with arrows.

Obviously, there are two critical parameters when creating a single cell array by cellular self-organisation. First, the size of the adhesive islands has to be tuned so that the provide

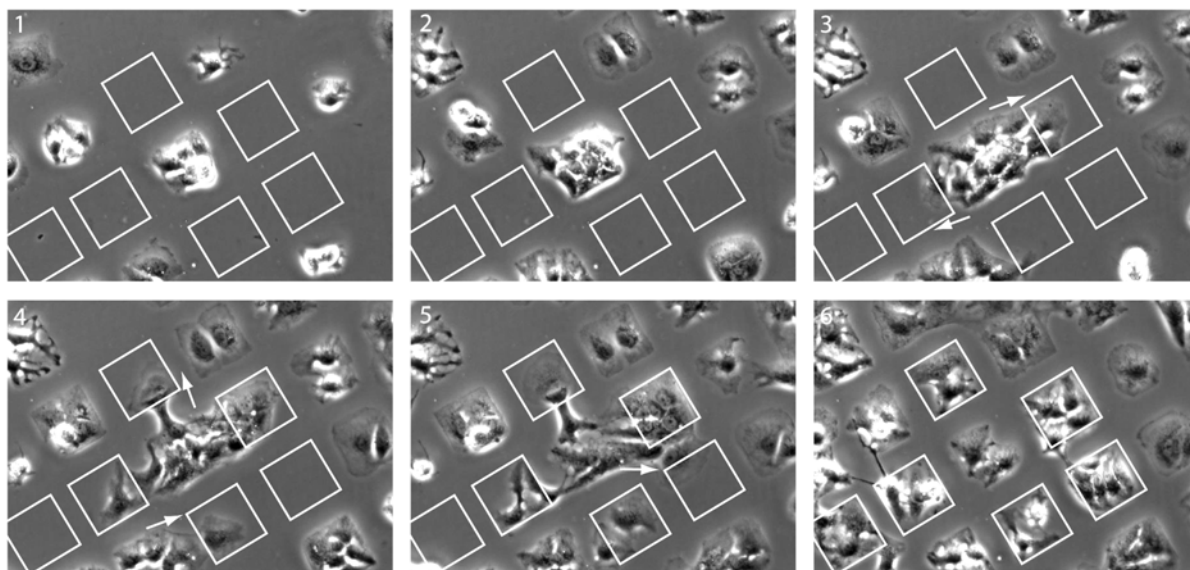


**Figure 9.2: Self-organisation of cells on a structured PDMS surface.** When adhesive islands become overpopulated, superfluous cells are expelled and migrate towards empty islands self-organizing into a more ordered array.

enough space for one cell but still superfluous cells are expelled from it. Second, as mentioned above, the non-adhesive parts of the pattern must support cell crawling but not permanent cell adhesion. Non-treated, medium-exposed hydrophobic PDMS proves to be an optimal substrate for this task. However, there are not commercial available grids which render the optimal size of the adhesive islands for single cell assays, experimentally found to be  $\approx 30\mu\text{m}$ , and  $\mu\text{CP}$  patterning techniques must be applied at this point. The problem would be immediately solved if it was possible to print fibronectin islands on a native PDMS substrate. Nevertheless, repeated experiments showed that in order to achieve reproducible good quality fibronectin patterns on a PDMS surface, this surface has to be slightly hydrophilized. This is enough to support permanent cell adhesion and destroy the cell patterns a short time following cell adhesion. For this reason, the PDMS surface has to be passivated with a backfill. A serie of experiments was carried out in order to find a backfill that supports cell migration but is rejected against fibronectin for permanent adhesion. The results of these experiments are summarized in table9.1. For example, a BSA backfill exhibited initial cell confinement to the fibronectin islands but cell spreading over the backfilled areas after 18h. With a PLL backfill, cells showed the same affinity for the fibronectin stamped and the PLL backfilled ones. A mixture of Pluronic<sup>®</sup> F-127 and fibronectin, used as backfill with the finality of introducing sparsely distributed adhesion cues all over the passivated surface in order to facilitate cell migration, displayed no differences when compared with the pure Pluronic<sup>®</sup> backfill. Finally, a mixture of Pluronic<sup>®</sup> with a 0.05% PLL rendered a backfill with the desired features.

As proof of principle, figure 9.3 shows a single cell array on such a surface, with  $30\mu\text{m}$

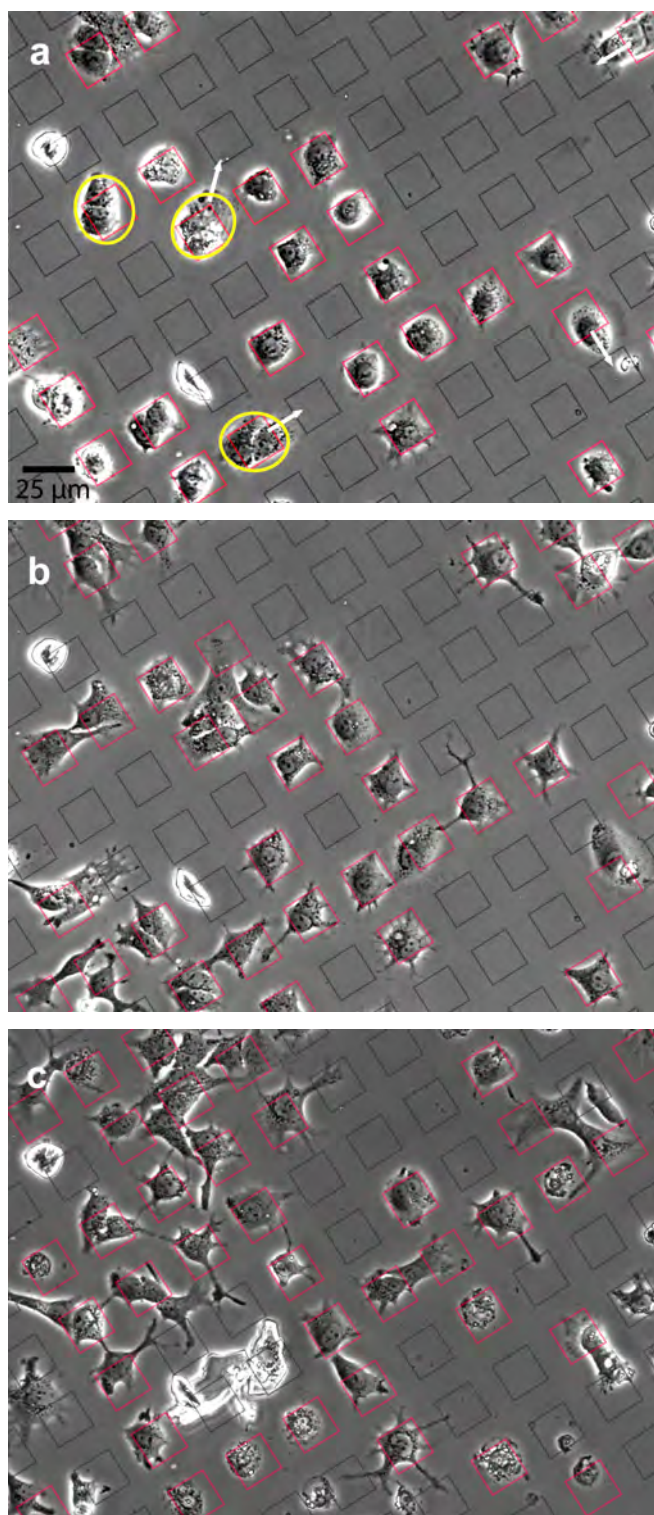


**Figure 9.3: Self-organisation of cells on a fibronectin printed surface with Pluronic®/PLL backfill.** Huh 7 cells were seeded on  $30\mu m$  printed fibronectin islands. After initial adhesion on the fibronectin islands (a), cells start to migrate and self-organize on the surface. With increasing time, the array becomes more ordered. Notice the difference between 2h, b and 24h, c

| Backfill                    | Concentration              | Adhesion | Migration |
|-----------------------------|----------------------------|----------|-----------|
| BSA                         | 0.2/2/10 mg/ml             | yes      | yes       |
| Casein                      | 10 mg/ml                   | yes      | yes       |
| PLL                         | 50 $\mu$ g/ml              | yes      | yes       |
| Plu F-127 <sup>®</sup>      | 0.5/1/2 mg/ml              | no       | no        |
| Plu F-127 <sup>®</sup> +BSA | 1/0.5 mg/ml + 10 mg/ml     | no       | no        |
| Plu F-127 <sup>®</sup> +FN  | 10 mg/ml + 2.5 $\mu$ g/ml  | no       | no        |
| Plu F-127 <sup>®</sup> +PLL | 10 mg/ml + 1.25 $\mu$ g/ml | no       | no        |
| Plu F-127 <sup>®</sup> +PLL | 10 mg/ml + 5 $\mu$ g/ml    | no       | yes       |

**Table 9.1:** Summary of the results obtained for different backfill strategies

printed square fibronectin islands and Pluronic<sup>®</sup>/PLL backfill. In Fig.9.3 a, it can be seen that cells initially adhere to the fibronectin islands. We found islands with one, two or three cells. Superfluous cells, such as those marked with yellow circles, start to migrate looking for empty islands. After two hours, there is already some degree of self-organisation, as can be observed in Fig.9.3 b. After 24h, Fig.9.3 c, the number of occupied islands is notably increased.

### 9.3 Conclusions and outlook

In this chapter, it has been demonstrated that it is possible to tune the adhesive properties of a patterned surface in order to create a single cell array by cellular self-organisation. In order to standardize the assay, further parameters, such as initial cell concentration and distance between adhesive islands must be adjusted. In future work, it would be interesting to establish the adequate magnitudes to describe such a system. For example, an order parameter,  $S$ , can be defined to characterize the degree of organization of the system. A possible definition of the order parameter is:

$$S = \frac{N_o - N_i}{N_o + N_i} \quad (9.1)$$

. being  $N_o$  the number occupied adhesion islands and  $N_i$  the number of interstitial cells.

Given that the adhesive and non adhesive surfaces have the same area, this parameter would be zero at the beginning and increase as cells seek adhesive islands and occupy them while the number of interstitial cells decreases. It is expected to reach a maximum, after which the system becomes again disordered, since the number of cells increases steadily due to cell division and the number of adhesive islands remains constant. The number of occupied adhesive islands can be captured in a occupation number, defined as  $\phi_o = N_o/N$ , being  $N$  the total number of adhesive islands. Such magnitudes would permit to apply statistical analysis in order to describe the system.





# Chapter 10

## Multifunctional spatially controlled patterning

In chapter 5,  $\mu$ PIP technique was refined rendering an easy, fast and reproducible method to achieve patterned hydrophobic/hydrophilic substrates. Major inconvenients of this method are that the features of the pattern are limited to the availability of grid masks, and that the surface modification of the adhesive island can not be controlled. In this chapter, new experimental approaches which enable better control of both, surface modification and pattern features are developed. For the first time, multifunctional patterned surfaces consisting of three different surface functionalizations are fabricated.

### 10.1 Plasma induced patterning with backfilling

In this section, the backfilling technique, usually applied after  $\mu$ CP, is utilized to improve  $\mu$ PIP. The first goal is to passivate the hydrophobic parts of the patterns and in this way gain control over the surface modification of the hydrophilic ones. The best alternative to passivate an hydrophobic background are Pluronic<sup>®</sup> block copolymers [71]. These consist of ethylene oxide (EO) and propylene oxide (PO) blocks arranged in a basic A–B–A structure: EO<sub>x</sub>–PO<sub>y</sub>–EO<sub>x</sub> [95]. Figure 10.1 depicts the working principle of this technique. The hydrophilic/hydrophobic patterned surface is incubated with a PLL solution, which adsorbs only to the hydrophilic negatively charged parts of the pattern. The hydrophobic parts of the pattern are then backfilled with Pluronic<sup>®</sup> F-127, to block unspecific attachment of proteins and cells to them. The fluorescence micrograph shows an example of selective adsorption on hydrophilic/hydrophobic patterns. In this case, the pattern is further incubated with a Cy5 labeled plasmid DNA solution, which attach only onto the PLL squares and produces the registered fluorescence signal.

This method is however not adequate to create adhesive squares modified with extracellular matrix proteins, such as fibronectin and collagen, since they preferentially adsorb to hydrophobic substrates. Thus, a backfill which adsorbs to hydrophilic surfaces is needed. A good candidate is poly-L-lysine grafted PEG (PLL-g-PEG). PLL-g-PEG is a

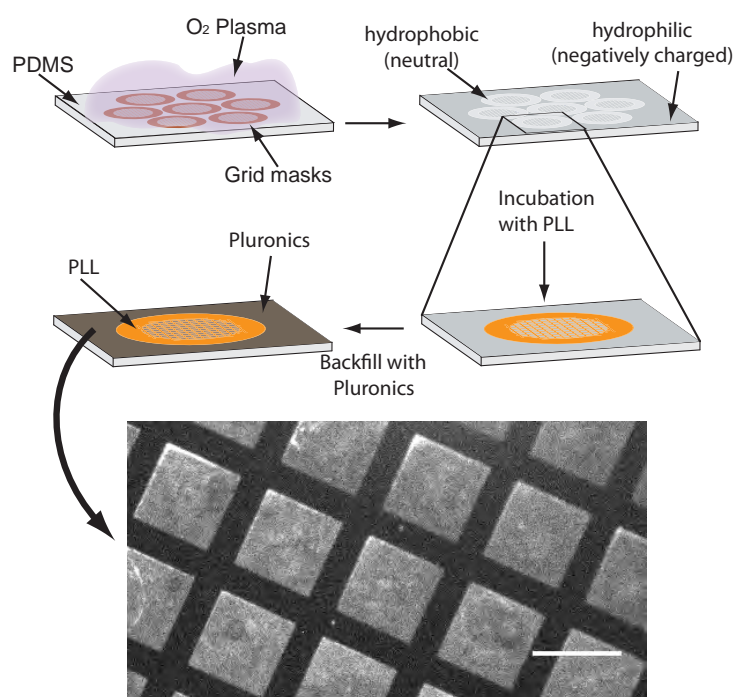


**Figure 10.1: Microscale plasma induced patterning with Pluronic<sup>®</sup> F-127 backfill.** An hydrophilic/hydrophobic patterned surface is created by  $\mu$ PIP using a TEM grid as a mask. The substrate is incubated with PLL, which selectively adsorbs onto the hydrophilic negatively charged parts of the pattern. The rest of the pattern is passivated with Pluronic<sup>®</sup> F-127. The fluorescence micrograph shows PLL adsorption confined to the hydrophilic squares, backfilling with Pluronic<sup>®</sup> and posterior adsorption of a Cy5-labeled plasmid on the PLL squares. Scale bar corresponds to 100  $\mu\text{m}$

graft copolymer composed of PEG chains grafted onto a polycationic PLL backbone. It is spontaneously attracted to negatively charged surfaces as a result of the polycationic PLL backbone, which acts as anchoring group through electrostatic interactions with the surface, while the PEG side chains stretch into the bulk aqueous solution to generate a brushlike conformation, acting a passivating agent [96]. Using PLL-g-PEG as backfill enables not only the control over the surface modification but also the control over the pattern features. To create a pattern of fibronectin squares with a PLL-g-PEG backfill we need to protect the squares from the plasma and expose the rest of the pattern to it. Obviously, this can not be achieved with a TEM grid as mask, but we can use a PDMS stamp. The squares in contact with the surface, protect it from the plasma, while the open structure enables the plasma access to the space between the squares, rendering them hydrophilic. Figure 10.2 depicts this method and shows a fluorescence micrograph as proof of principle. First the PDMS stamp is brought in contact with the substrate. After oxygen plasma exposure, the squares remain hydrophobic and the rest of the surface is rendered hydrophilic. Since it is known that PLL-g-PEG can also adsorb onto hydrophobic substrates, mainly due to the hydrophobic interaction between the PLL backbone and the surface [96], [97], the stamp is left in place during PLL-g-PEG adsorption. The PLL-g-PEG solution is micromolded, adsorbing exclusively to the hydrophilic negatively charged parts of the pattern. Then the pattern is incubated with the protein of interest, in this case Alexafluor488-Fibronectin, which adsorbs only on the hydrophobic squares, as can be seen in the fluorescence micrograph. In this case an hydrophobic Topas substrate was used instead of PDMS.

## 10.2 Multifunctional spatially controlled patterning

In the last section, improvements to the  $\mu$ PIP technique introduced by Langowski [73] which enable complete control over the characteristics of the patterned surface, such a size and shape of the adhesive islands and surface modification, have been introduced. However, the patterned substrates still present a restriction: only two different surface modifications can be produced. At this stage, one can think of taking advantage of the use of stamps as protective masks for the plasma treatment to bring an additional surface modification on the substrate, as illustrated in figure 10.3.

The hearth of this method is to combine  $\mu$ CP and  $\mu$ PIP to create substrates with three different surface modifications. For this task, stamps where only the edges of the adhesive islands have contact with the substrate, as those shown in figure 10.3 (in this case for squares), are needed. The stamp is incubated with one kind of ECM protein. When the stamp is put onto the substrate, it simultaneously performs two functions, to print the protein and to protect the inner parts of the squares from the plasma treatment. At this point, three different kinds of surfaces have already been created, the hydrophilic one, the hydrophobic one and the one coated with protein. Now, PLL-g-PEG is adsorbed to the hydrophilic parts of the pattern (as backfill) and a second protein of interest is now be adsorbed to the empty hydrophobic parts of the pattern. As proof of principle, the

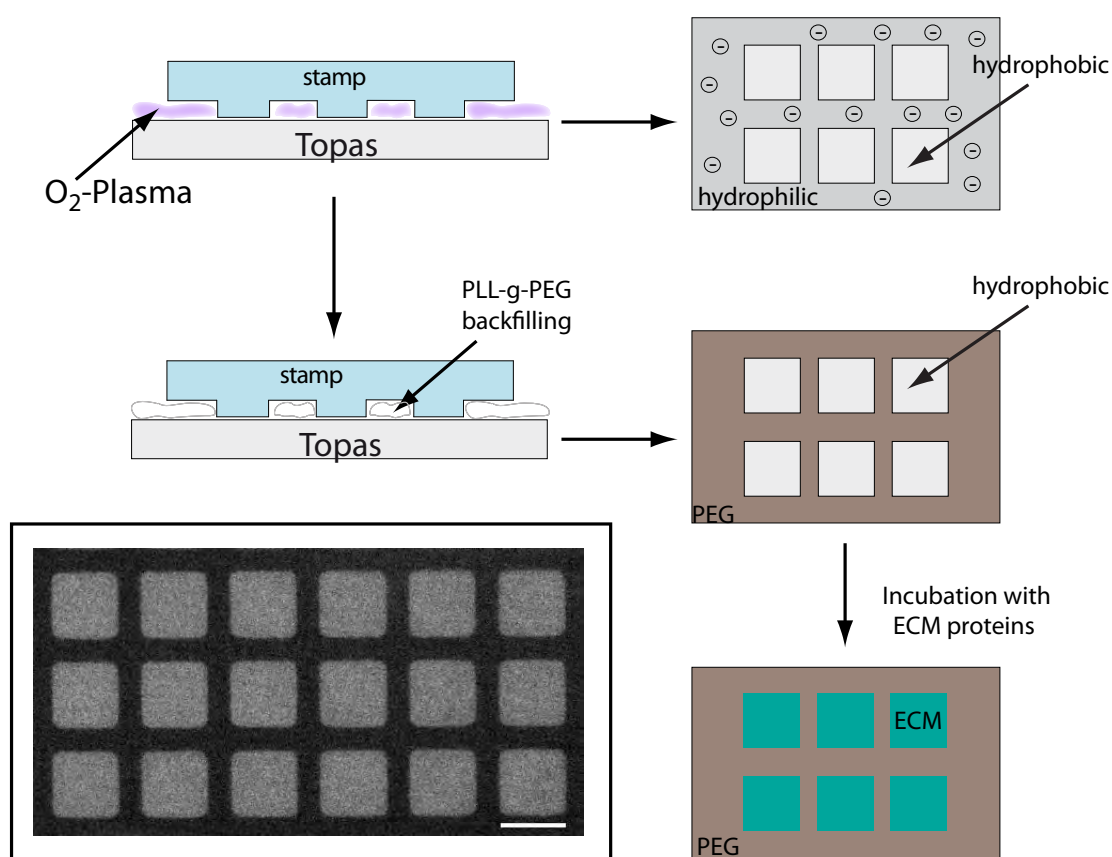


**Figure 10.2: Microscale plasma induced patterning with PEG-g-PLL backfill.** In this approach the hydrophilic parts of the pattern are passivated with PEG-g-PLL and the hydrophobic parts are functionalized with Fn for cell adhesion. A PDMS stamp is used as a mask for plasma treatment in order to create an hydrophilic/hydrophobic pattern on the surface. Leaving the stamp at place, to avoid PEG-g-PLL adsorption on the hydrophobic squares, the hydrophilic parts of the pattern are passivated with PEG-g-PLL. After stamp removal, the substrate is exposed to the protein of interest. As proof of principle, the fluorescence micrograph shows a patterned surface functionalized with Alexafluor488-Fibronectin.

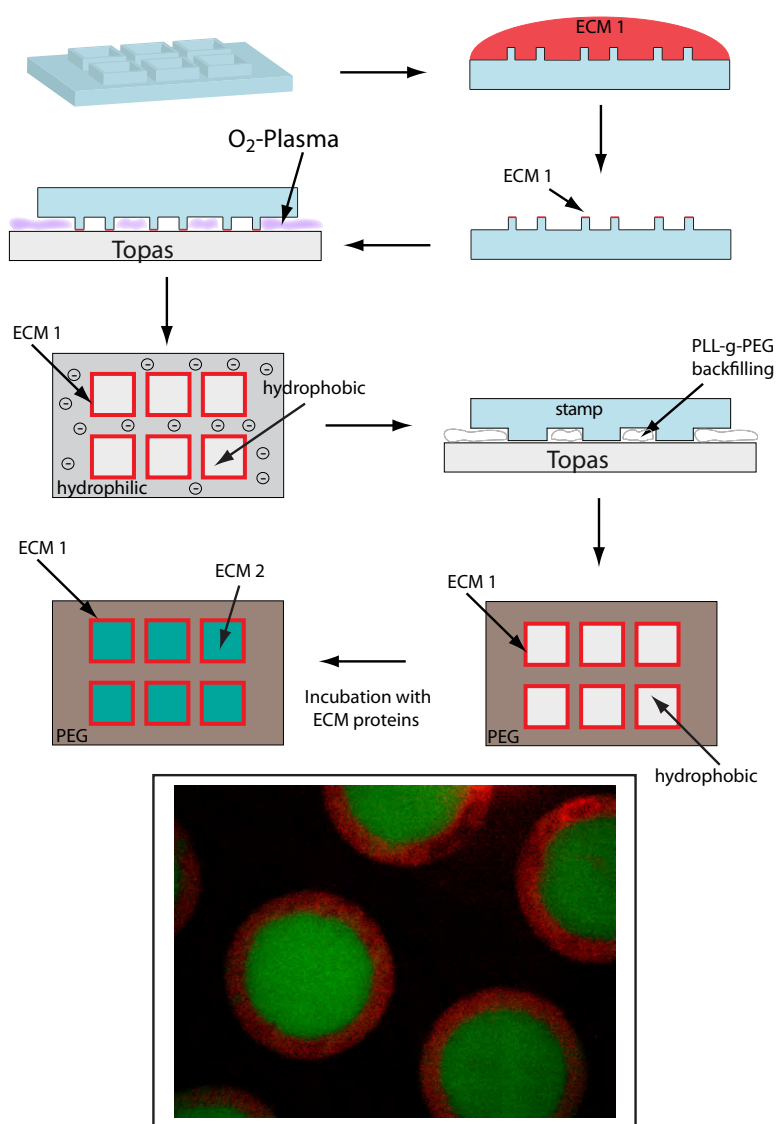


**Figure 10.3: Ternary substrates.**  $\mu$ CP and  $\mu$ PIP are combined to create a patterned substrate with a three-fold surface modification. The PDMS stamp used as protective mask is designed such that only the edges of the adhesive islands touch the substrate. This stamp is incubated with the protein of interest and deposited onto the substrate. It accomplishes two functions, simultaneously printing the protein at the edges of the adhesive spots and protecting their interior from plasma treatment. Without removing the stamp, the hydrophilic surface is passivated with PEG-g-PLL. After stamp removal, the substrate is exposed to a second protein which will adsorb only to the empty parts of the pattern. The fluorescence micrograph shows ternary substrates constituted by printed Cy5-pEGFP-N1 plasmid at the edges of adhesive circles and Alexafluor488-Fibronectin circles.

fluorescence micrograph shows a ternary substrate fabricated in this way. In this case, Cy5-pEGFP-N1 plasmid was printed at the edges of the circles and Alexafluor488-Fibronectin was adsorbed on the hydrophobic areas.

Such ternary substrates represent an important improvement of micropatterning techniques and could for example be exploit to discern the role that different distributions of ECM components have on cell shape, function and internal structure.

# Chapter 11

## Conclusions and outlook

Within this thesis, novel approaches to study several aspects of the biophysics of the cell, including particle internalisation, gene expression, cell mechanics and collective cell migration, and new strategies to engineer the cell microenvironment have been developed. It has been established that defined cellular microenvironments not only reduce experimental variability but improve the capability of quantitatively measure cellular responses. For example, taking in account the colloidal nature of NPs and separating particle preparation from cell exposure, it was possible to generate controlled distributions of particles and at the same time to establish a reference surface for to monitor NP uptake. By imposing defined boundary conditions to small groups of cells it was possible to study phenomena, such as relaxation into stable packing states and collective movements, that don't appear at the single cell level and are too complex to analyze at the full tissue level. Oligocellular arrays make theoretical modeling amenable and the knowledge gained with them can help to understand cell behavior at the full tissue level.

Oligocellular arrays also represent an important advance towards more physiological assays with reduced cell-to-cell variability and for this reason, in future experiments, the surface controlled approach and the oligocellular arrays will be combined in order to create standardized nanotoxicity assays.

Single cell arrays can also be combined with surface controlled gene delivery in order to create an experimental platform in which all cells are exposed to uniform experimental conditions and in which automated image analysis is much easier, since cells are confined to predetermined positions and exhibit fixed shapes. This may be the basis for future single cell high-throughput assays.

Ternary substrates open a new field of experimentation, because more physiological and defined substrates can be created. An intriguing possibility is to create artificial ordered tissues, with all cells in the same "state" but all in contact throughout the culture, as shown in Fig.11.1. Cadherin could be printed at the edges of fibronectin hexagons, creating a substrate that encodes information for cell packing mimicking natural packing in epithelial sheets. The seeded on this microenvironment will receive cues from the substrate that signal the possible presence of neighboring cells. It is to expect that in the presence of other cells, they respect these signals and arrange in the configurations encoded by the

substrate.

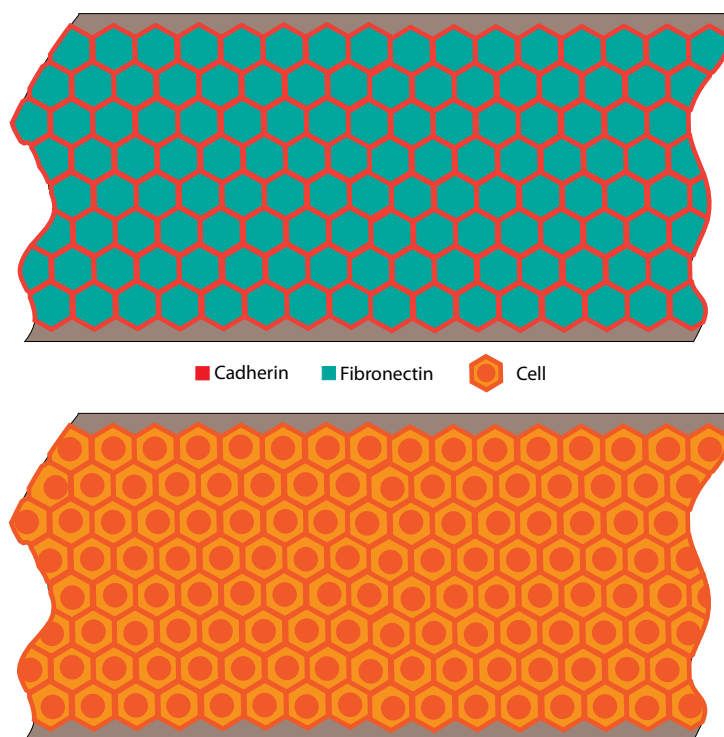


**Figure 11.1: Artificially ordered tissue.** The information needed for cell packing could be encoded in the substrate, in form of a regular pattern of cadherin and fibronectin.

Another possibility would be to discern the roles of cell-cell and cell-substrate adhesion sites play in cell shape and structure making use of engineered substrates in which cadherin/fibronectin patterns are inverted, as shown in Fig.11.2.



**Figure 11.2: Structural role of cell-cell and cell-substrate adhesions**



# Publications

## Publications during the course of this thesis

"The defined presentation of nanoparticles to cells and their surface controlled uptake." A. Piera Alberola and J. O. Rädler. *Biomaterials*, 30(22), 3766-3770, 2009.

"Oligocellular arrays unravel novel contributions to epithelial cell packing." A. Piera Alberola, K. Alim, A.-K. Marel, E. Frey and J. O. Rädler (submitted).

"Collective cell migration from oligocellular patches derived from microstructured lift-off" A.-K. Marel, A. Piera Alberola and J. O. Rädler (in preparation).

## Earlier publications

"Getting across the plasma membrane and beyond: intracellular uses of colloidal semiconductor nanocrystals" C. Luccardini, A. Yakovlev, S. Gaillard, M. van 't Hoff, A. Piera Alberola, J.M. Mallet, W. J. Parak, A. Feltz and M. Oheim. *Journal of Biomedicine and Biotechnology* 2007, Article ID 68963, 2007.

"Combined atomic force microscopy and optical microscopy measurements as a method to investigate particle uptake by cells" A. Muñoz Javier, O. Kreft, A. Piera Alberola, C. Kirchner, B. Zebli, A. S. Susa, E. Horn, S. Kempter, A. Skirtach, A. L. Rogach, J. Rädler, G. B. Sukhorukov, M. Benoit, W. J. Parak. *Small* 2, p.394-400, 2006.

"Laser-induced release of encapsulated materials inside living cells" A. G. Skirtach, A. Muñoz Javier, O. Kreft, K. Köhler, A. Piera Alberola, H. Möhwald, W. J. Parak und G. B. Sukhorukov. *Angewandte Chemie* 118, 28 , p. 4728 - 4733, 2006.



# Appendix A

## Standard procedures

### A.1 Cell culture

Cells were grown in medium supplemented medium in a humidified atmosphere, at 37° with 5%  $CO_2$  level. Cells were maintained at 85% confluence, trypsinized, washed with PBS, re-suspended in cell medium and counted using a Neubauer counting chamber.

| Cell line | Organism | Tissue | Medium      | Supplements              |
|-----------|----------|--------|-------------|--------------------------|
| Huh 7     | human    | liver  | MEM-F12     | 10%FBS, 5 mM L-Glutamine |
| MCDK      | canine   | kidney | Earle's MEM | 10%FBS, 4 mM L-Glutamine |
| Beas 2B   | human    | lung   | Earle's MEM | 10%FBS, 4 mM L-Glutamine |

**Table A.1:** Summary of cell lines used in this work

### A.2 Microscopy

NP internalization was studied using a Simple PCI (Compix) controlled motorized inverted microscope equipped with a temperature-controlled mounting frame. Illumination was generated using a mercury light source (HBO 100).

The rest of the images were acquired using a motorized Nikon Eclipse Ti microscope equipped with a temperature-controlled mounting frame, 10x, 20x, 40x and 100x Plan Fluor objectives, a CCD monochrome camera and a programmable stage. Acquisitions were controlled through  $\mu$ -Manager open source software. Fluorescence illumination was generated using an Intensilight lamp.

Fluorescent signals were detected using filter sets given in table A.2.

For living cell image acquisition, the temperature of the mounting frame temperature was set to 37°C and supplemented  $CO_2$  independent Leibovitz's L15 cell culture medium was used.

| Fluorophore | Excitation | Reflector | Emission |
|-------------|------------|-----------|----------|
| GFP         | BP470/40   | FT495     | BP525/50 |
| DAPI        | BP360/40   | 400DCLP   | BP360/50 |
| QDot        | BP435/40   | FT510     | BP655/15 |

**Table A.2:** Filter sets used in this work

### A.3 $\mu$ -slide coating

When needed,  $\mu$ -slides were pre-coated with collagen type I, PLL or fibronectin prior to use. Briefly, 30  $\mu$ l of stock solutions (Collagen, 40  $\mu$ g/ml diluted in 0.2% acetic acid, PLL 0.1 mgr/ml and fibronectin 50  $\mu$ g/ml) were added into each channel and adsorbed during one hour. Channels were then rinsed thrice with Millipore water.

### A.4 Cell nuclei staining

Cells were fixed during 20 min with 10% of formaldehyde in cell culture medium and rinsed thrice with PBS buffer. Then, they were incubated 5 min in a 2  $\mu$ g/ml 4'6-diamidino-2-phenylindole (DAPI, Sigma) in PBS and rinsed again thrice with PBS buffer.

## A.5 Experiments with NPs

### A.5.1 Nanoparticle characterization

Core size and shape were determined with TEM. NPs were adsorbed onto a Formvar/Carbon film-coated grid and observed with a Jeol 1011 TEM. NPs are monodispersed and oval, with a mean size  $r_{TEM} = (4.8 \pm 0.5)$  nm. Hydrodynamic radius and agglomeration states were studied with FCS. The confocal volume was calculated using a Rhodamine 6 G solution. The measured diffusion time was  $\tau_d = (495 \pm 12)\mu$ s, giving a hydrodynamic radius  $r_h = (14.9 \pm 0.4)$  nm for the QDs in water.

### A.5.2 Preparation of surfaces with a certain amount of well dispersed NPs

Closed channeled chambers ( $\mu$ -slides VI and I, ibidi-GmbH) are used to avoid the meniscus effect and obtain a homogeneous distribution of NPs and cells. These chambers also allow buffer interchange, drying effect elimination, and subsequent NP distribution irregularities. The surface is comparable to standard cell culture flasks and Petri dishes. To achieve a homogeneous distribution of single NPs, a very thin NP solution ( $c < 100$  pm) is needed. Starting from the initial concentration (7.4  $\mu$ m), successive NP solutions are prepared (until 1 nm) in PBS buffer without ions. A last dilution is made with PBS containing  $Ca^{++}$  and

$Mg^{++}$  ions to help NP settling. 30  $\mu\text{l}$  of this final NP solution are introduced into each channel. An incubation time of 30 min and a 15 pm solution are needed for a standard NP density of 0.5 NPs/ $\mu\text{m}^2$ . Channels are rinsed thrice with PBS prior to use. Under these conditions, the number of adsorbed NPs is proportional to the concentration of NPs (see Fig.3.4).

### A.5.3 NP exposure assay

Beas-2B cells were re-suspended in supplemented MEM to achieve a concentration of  $10^4$  cells/ml. 30  $\mu\text{l}$  (100  $\mu\text{l}$ ) of this cell suspension was added to each channel in  $\mu$ -slides VI (I). After 10 min, enough medium was added to fill the reservoirs. Cells were then incubator at 37 °C in a humidified atmosphere, 5%  $CO_2$  level until image acquisition. For time-lapse experiments, cells were placed in the incubator for 30 min to allow them to attach to the surface. Then medium was removed and  $CO_2$ -independent medium, L-15 (10% FBS), was added. Cells were immediately placed on the microscope stage at 37 °C.

### A.5.4 NP surface dependent uptake

Particles were adsorbed onto bare surfaces and surfaces pre-coated with PLL or collagen. GFP-expressing BEAS-2B cells were seeded onto the surfaces and incubated overnight at 37 °C in a humidified atmosphere, 5%  $CO_2$  level. Two channels per surface type were prepared and the number of internalized NPs was counted for five randomly-selected cells per channel. Before imaging, channels were rinsed once with PBS and fresh L-15 medium was added.

### A.5.5 NP time-dependent uptake

NPs and cells were prepared as described. Images were acquired during 24 h with a time interval of 30 min.

## A.6 Sample preparation for TEM

Cells were seeded in Transwell membranes with a concentration  $4 * 10^4$  cells/well. After cell spreading they were incubated with NPs.

### Day 1: Fixation

3x rinsing with cacodylate puffer 0,1M pH 7,2.

1x Karnovsky, samples are left overnight in cacodylate buffer at 4°C.

## Day 2

3x 15 min rinsing with cacodylate buffer pH 7,2.

Cells are left overnight in cacodylate buffer to eliminate the glutaraldehyde.

## Day 3: Contrasting

The membranes are cut in pieces and stored in labeled eppendorf tubes.

Mix 1:1 :4% Osmium tetroxid and 0,2M cacodylate buffer(store this solution at 4°C)

Make 3% Kaliumferrocyanide in 0,2M caco buffer (3 gr/ 100 ml)

Mix both solutions 1:1, it will become brown. Cells are incubated 2h in this solution.

3x 15 min rinsing with cacodylate buffer 0,1M

Cells are left overnight in cacodylate buffer at 4°C.

## Day 4: Dehydration and first embedding

At room temperature and on the shaker

30% Ethanol 20 min.

50% Ethanol 20 min.

75% Ethanol 20 min.

95% Ethanol 30 min.

3x 100% Ethanol 30 min.

2X Propylene oxide 15 min.

2:1 Propylene oxide/resin, 60 min.

1:1 Propylene oxide/resin, overnight.

## Day 5: Embedding

At room temperature and on the shaker:

Warm the resin 5 min at 60-70°C.

100% resin, 60 min.

Samples into embedding forms with resin. Bake two days in the oven at 60°C .

## A.7 Patterning Protocols

### A.7.1 Plasma initiated patterning

We use the patterning technique reported by Hsieh et al.[74] with some modifications. PDMS (Sylgard 184, Dow Corning, Midland, MI, U.S.A.) was prepared in a 10/1 w/w ratio. The mixture was stirred and degassed for ten minutes. This mixture was spin coated on an Ibidi  $\mu$ -slide (Ibidi-GmbH, München, Germany) at 2000 rpm for 10 s followed by 4000 rpm for 30 s. The coated slides were degassed again and the PDMS was cured in the oven overnight at 50°C. The copper TEM grids were pre-exposed to water vapor

for 30 s, to create a water bridge between the grid and the PDMS surface as described by Andruzzi[98], and immediately placed onto the PDMS surface. The samples were exposed to low pressure oxygen plasma for 2 min (40W 5 cm<sup>3</sup>/min at 25°C and 2 bar, Femto, Diener) and, afterwards, sonicated 1 min in 80% ethanol to remove the copper grids and 3 min in water to clean them. Samples were sterilized in 80% ethanol, submerged 15 min in sterile Millipore water to remove ethanol residues and used immediately. In contrast with the results obtained in [74], the sample regions that were protected from the plasma remained hydrophobic while the rest of the sample became hydrophilic, as we expected.

### A.7.2 PDMS stamp preparation

PDMS is prepared in a 10/1 w/w ratio. This mixture is stirred, poured onto the silicon master and degassed for ten minutes. Then, it is baked during 45 minutes at 80°C or overnight at 50°C.

### A.7.3 Microcontact printing

#### Fibronectin printing on PDMS

First the PDMS stamps are sonicated in ethanol during 20 min and then dried with N<sub>2</sub>. The clean stamps are then hydrophilized by 15 min exposure to UV/Ozone or alternatively 30 sec exposure to oxygen plasma (40 W). A drop of fibronectin solution, 25 μgr/ml in H<sub>2</sub>O is placed onto the stamp and incubated during 1h. The fibronectin solution is then aspirated and the stamp dried with N<sub>2</sub>. The spin coated PDMS substrate is slightly hydrophilized by 8 min exposure to UV/Ozone. The stamp is then carefully placed onto this substrate and the edges of the stamp are lightly pressed with the tweezers. After two or three minutes the stamp is carefully removed avoiding further contacts with the substrate.

#### Fibronectin printing on uncoated μ-dishes

Prior to use the PDMS stamp is silanized with perfluorooctyltrichlorosilane. The silanized stamp is sonicated in ethanol during 15 min and then dried with N<sub>2</sub>. Then it is incubated during one hour in a fibronectin solution (25 μgr/ml in H<sub>2</sub>O), washed once with PBS and let dry. The coated stamp is carefully placed on the μ-dish and the edges of the stamp are slightly pressed with the tweezers. After two or three minutes the stamp is carefully removed avoiding further contacts with the substrate.

### A.7.4 Backfill with Pluronic<sup>®</sup> F-127

For the backfill the printed substrate is incubated with a Pluronic F-127 solution (10 mg/ml in H<sub>2</sub>O). The substrate is then washed three times with PBS.

### A.7.5 Plasma induced patterning with PEG-g-PLL backfill

A PDMS stamp is placed on a  $\mu$ -dish and exposed to low pressure oxygen plasma for 2 min (40W 5 cm<sup>3</sup>/min at 25°C and 2 bar, Femto, Diener). Prior to stamp removal, the hydrophilic parts of the pattern are passivated with a PEG-g-PLL (1 mgr/ml in 10mM HEPES + 150mM NaCl buffer, pH 7,4) solution during 30 min. The  $\mu$ -dish is rinsed throughly three times with H<sub>2</sub>O and then the stamp is removed. The hydrophobic parts of the patterns are then functionalized by incubation with a fibronectin solution (50  $\mu$ gr/ml in H<sub>2</sub>O) during 1 hour. The  $\mu$ -dish is then rinsed twice with PBS.

### A.7.6 Cell patterning

Cells were re-suspended in supplemented culture medium, seeded on the microstructured surfaces and incubated at 37°C in a humidified atmosphere, 5% CO<sub>2</sub> level. After 20 min, chambers were rinsed with cell medium in order to remove non-attached cells.

## A.8 Transfection protocols

### A.8.1 Complex preparation

Prior to complex preparation all media and buffers were tempered at 37°C.

#### **FuGENE®**

The desired amount of plasmid is diluted in 100  $\mu$ l of growth medium (or water) and mixed throughly. Then FuGENE® in the desired ratio is carefully added, taking care of not touching the eppendorf walls with it. The solution is vortexed and incubated 25 min.

#### **l-PEI**

The desired amount of plasmid is diluted in 50  $\mu$ l of HBS buffer and and mixed throughly. The amount of l-PEI necessary to obtain the desired N/P ratio is is diluted in 50  $\mu$ l of HBS buffer. The l-PEI solution is then carefully added to the plasmid solution. The final solution is mixed throughly and incubated 20 min at room temperature.

### A.8.2 Reverse transfection in $\mu$ -slides

When necessary  $\mu$ -slides were precoated as described in A.3. Then, 30  $\mu$ l of complex solution were introduced in each channel. After 1 hour of incubation at at 37° with 5% CO<sub>2</sub>, channels were rinsed trice with the adequate buffer and cells were seeded onto the prepared surface. Transfection efficiency was monitored after at least 24h.



### A.8.3 Transfection efficiency assessment

Fluorescence micrographs and their corresponding phase contrast micrographs were acquired in ten randomly selected positions per  $\mu$ -channel. The number of GFP-expressing cells and the total number of cells were manually counted. Two  $\mu$ -channels per sample were analyzed.



# Appendix B

## Calculation of cell packing states

These calculations were made by Karen Alim from the group of Erwin Frey, LMU, Munich.

Describing cells as two dimensional polygons, the geometric properties of cell packing states for  $N=2,3,4$  cells per square adhesion patch of side length  $\ell$  are calculated according to the vertex positions of individual cells given in Figures B.1 and B.2. Note that the vertex model neglects cell shape undulations and discusses cell states with straight cell boundaries only; fluctuations in cell boundaries are incorporated in  $\alpha$  and  $\kappa$  as effective parameters. States within a packing class vary with respect to the angle  $\vartheta$  enclosed between the cell-cell contact lines and the confining patch as depicted for each class in Figures B.1 and B.2. Due to the fourfold rotational symmetry of the square only angles  $0^\circ \leq \vartheta \leq 45^\circ$  denote mutually different states. Given all  $n$  vertices  $\{x_i, y_i\}$  of a cell, its corresponding perimeter  $P$  is given by

$$P = \sum_{i=1}^n \sqrt{(x_i - x_{i-1})^2 + (y_i - y_{i-1})^2} \quad (\text{B.1})$$

the contact length  $L$  forms the according subset. The model presented in Equation 7.1 is extended with an additional energy term to account for cell anisotropy. The size-independent anisotropy of an individual cell is defined as the normalized variance of the eigenvalues  $\lambda_{1,2}$  of the second moment of area.

$$\Delta = \frac{\text{var}(\lambda)}{\langle \lambda \rangle^2} = \left( \frac{\lambda_1 - \lambda_2}{\lambda_1 + \lambda_2} \right)^2 \quad (\text{B.2})$$

The normalization by the mean of the eigenvalues ensures that the anisotropy measure is independent of the total cell area.

The second moments of area,  $M$ , for a simple polygon in the XY plane can be computed in a generic way by summing contributions from each segment of a polygon. Each segment is defined by two consecutive points of the polygon and a triangle with two corners at these points and the third corner at the origin of the coordinates is considered. Integration by the area of that triangle and summing by the polygon segments yields:

$$M = \begin{pmatrix} m_{xx} & m_{xy} \\ m_{xy} & m_{yy} \end{pmatrix} \quad (\text{B.3})$$

$$m_{xx} = \frac{1}{12} \sum_{i=1}^n (y_i^2 + y_i y_{i+1} + y_{i+1}^2) (x_i y_{i+1} - x_{i+1} y_i) \quad (\text{B.4})$$

$$m_{xy} = \frac{1}{24} \sum_{i=1}^n (x_i y_{i+1} + 2x_i y_i + 2x_{i+1} y_{i+1} + x_{i+1} y_i) (x_i y_{i+1} - x_{i+1} y_i) \quad (\text{B.5})$$

$$m_{yy} = \frac{1}{12} \sum_{i=1}^n (x_i^2 + x_i x_{i+1} + x_{i+1}^2) (x_i y_{i+1} - x_{i+1} y_i) \quad (\text{B.6})$$

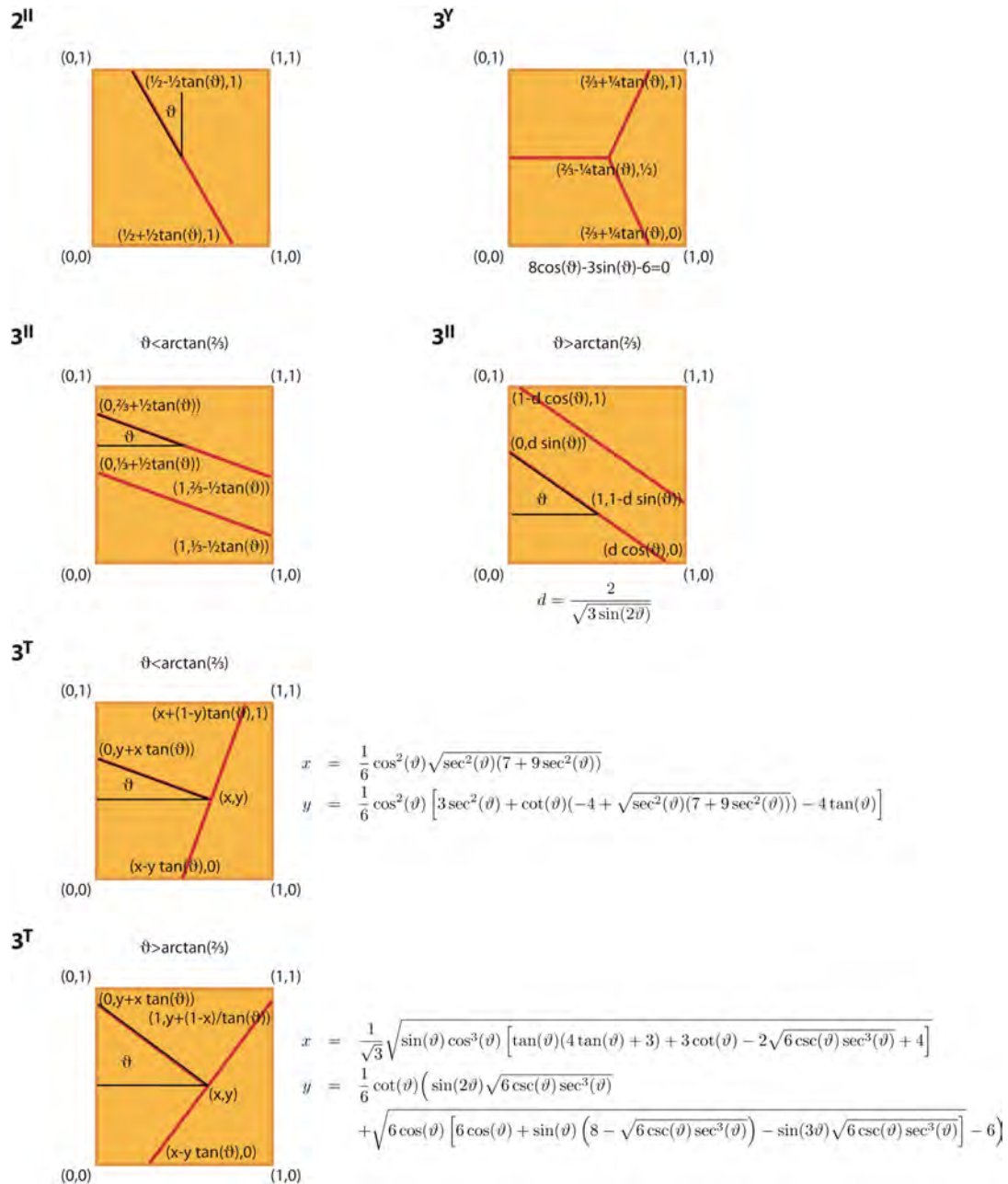
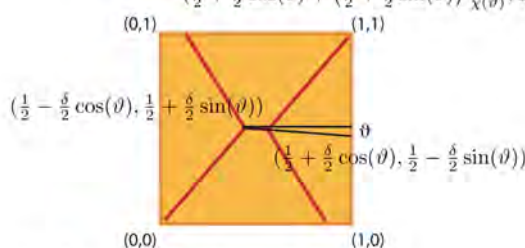
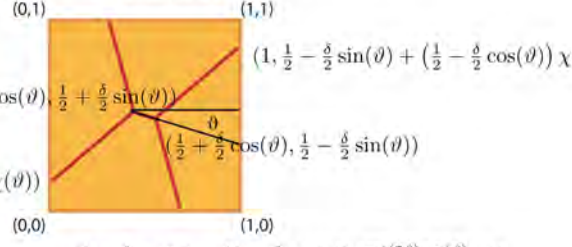


**Figure B.1: Calculation of cell packing states for  $N=2,3$ .** In a square normalized to side length the formula for the coordinates are indicated next to the corresponding vertex for the packing classes  $2^T$ ,  $3^Y$ ,  $3^{II}$ , and  $3^T$ .

$4_{\delta}^X$ 



$$\chi(\vartheta) = \frac{2 \left( \delta^2 \cos(2\vartheta) \tan(\vartheta) + \sqrt{-\delta^4 + (\delta^2 + 1)^2 \sec^2(\vartheta) - 8\delta \sec(\vartheta) + \csc^2(\vartheta) + 4 + 2 \cot(2\vartheta) - 2} \right) + 8\delta \cos(\vartheta)}{4 \left( \delta^2 \sin^2(\vartheta) - 2\delta \cos(\vartheta) \cot(\vartheta) - \tan(\vartheta) + \cot(\vartheta) + 1 \right)}$$



$$\chi(\vartheta) = \frac{\delta \sec(2\vartheta) [-2\delta \sin(\vartheta) \cos^3(\vartheta) + \sin(3\vartheta) + \cos(\vartheta)]}{(\delta \cos(\vartheta) - 1)^2} + \frac{\tan(2\vartheta) \sqrt{2 \csc(2\vartheta) [\csc(2\vartheta) (-\delta^4 \cos(4\vartheta) + \delta^4 + 4\delta^3 \cos(3\vartheta) - 4(\delta^2 + 4)\delta \cos(\vartheta) + 16\delta^2]}}{4(\delta \cos(\vartheta) - 1)^2} + \frac{\tan(2\vartheta) \left( \sqrt{2 \csc(2\vartheta) [\csc(2\vartheta) (-16\delta \sin(\vartheta) + 8) - 8\delta^2(\delta \cos(\vartheta) - 1)]} - 4 \right)}{4(\delta \cos(\vartheta) - 1)^2}$$

**Figure B.2: Calculation of cell packing states for N=4** In a square normalized to side length the formula for the coordinates are indicated next to the corresponding vertex for the packing class  $4_{\delta}^X$ .

# Bibliography

- [1] Dennis Bray. *Cell movements: From molecules to motility*. Garland Publishing, New York, 2001.
- [2] G. Schwake, S. Youssef, J. T. Kuhr, S. Gude, M. P. David, E. Mendoza, E. Frey, and J. O. Rädler. Predictive modeling of non-viral gene transfer. *Biotechnology and Bioengineering*, 105(4):805–813, 2010.
- [3] M. L. Yarmush and K. R. King. Living-cell microarrays. *Annual Review of Biomedical Engineering*, 11:235–257, 2009.
- [4] C. V. Rao, D. M. Wolf, and A. P. Arkin. Control, exploitation and tolerance of intracellular noise. *Nature*, 420(6912):231–237, 2002.
- [5] R. Singhvi, A. Kumar, G. P. Lopez, G. N. Stephanopoulos, D. I. C. Wang, G. M. Whitesides, and D. E. Ingber. Engineering cell-shape and function. *Science*, 264(5159):696–698, 1994.
- [6] M. Théry, V. Racine, A. Pepin, M. Piel, Y. Chen, J. B. Sibarita, and M. Bornens. The extracellular matrix guides the orientation of the cell division axis. *Nat. Cell Biol.*, 7(10):947–U29, 2005.
- [7] C. S. Chen, M. Mrksich, S. Huang, G. M. Whitesides, and D. E. Ingber. Geometric control of cell life and death. *Science*, 276(5317):1425–1428, 1997.
- [8] X. Y. Jiang, D. A. Bruzewicz, A. P. Wong, M. Piel, and G. M. Whitesides. Directing cell migration with asymmetric micropatterns. *Proc. Natl. Acad. Sci. U.S.A.*, 102(4):975–978, 2005.
- [9] T. Hayashi and R. W. Carthew. Surface mechanics mediate pattern formation in the developing retina. *Nature*, 431(7009):647–652, 2004.
- [10] R. Zaidel-Bar, M. Cohen, L. Addadi, and B. Geiger. Hierarchical assembly of cell-matrix adhesion complexes. *Biochemical Society Transactions*, 32:416–420, 2004.
- [11] B. Kasemo. Biological surface science. *Surf. Sci.*, 500(1-3):656–677, 2002.

- [12] A. J. Ridley, M. A. Schwartz, K. Burridge, R. A. Firtel, M. H. Ginsberg, G. Borisy, J. T. Parsons, and A. R. Horwitz. Cell migration: Integrating signals from front to back. *Science*, 302(5651):1704–1709, 2003.
- [13] C. H. Streuli and N. Akhtar. Signal co-operation between integrins and other receptor systems. *Biochemical Journal*, 418:491–506, 2009.
- [14] Matthieu Cavey and Thomas Lecuit. Molecular bases of cell-cell junctions stability and dynamics. *Cold Spring Harb. Perspec. Biol.*, 1(a002998), 2009.
- [15] T. J. Mitchison, G. T. Charras, and L. Mahadevan. Implications of a poroelastic cytoplasm for the dynamics of animal cell shape. *Seminars in Cell and Developmental Biology*, 19(3):215–223, 2008.
- [16] D. E. Ingber. Tensegrity-based mechanosensing from macro to micro. *Progress in Biophysics and Molecular Biology*, 97(2-3):163–179, 2008.
- [17] D. E. Ingber. Mechanical control of tissue morphogenesis during embryological development. *International Journal of Developmental Biology*, 50(2-3):255–266, 2006.
- [18] N. Wang, K. Naruse, D. Stamenovic, J. J. Fredberg, S. M. Mijailovich, I. M. Toric-Norrelykke, T. Polte, R. Mannix, and D. E. Ingber. Mechanical behavior in living cells consistent with the tensegrity model. *Proc. Natl. Acad. Sci. U.S.A.*, 98(14):7765–7770, 2001.
- [19] D. E. Ingber. Cellular tensegrity - defining new rules of biological design that govern the cytoskeleton. *J. Cell Sci.*, 104:613–627, 1993.
- [20] Sean D. Conner and Sandra L. Schmid. Regulated portals of entry into the cell. *Nature*, 422(6927):37–44, 2003.
- [21] C. Luccardini, A. Yakovlev, S. Gaillard, M. Van't Hoff, A. Piera Alberola, J.M. Mallet, W. J. Parak, A. Feltz, and M. Oheim. Getting across the plasma membrane and beyond: Intracellular uses of colloidal semiconductor nanocrystals. *Journal of Biomedicine and Biotechnology*, 2007:Article ID 68963, 2007.
- [22] D. E. Ingber. Mechanical control of tissue growth: Function follows form. *Proc. Natl. Acad. Sci. U.S.A.*, 102(33):11571–11572, 2005.
- [23] Bruce Alberts, Dennis Bray, Alexander Johnson, Julian Lewis, Martin Raff, Keith Roberts, and Pete Walter. *Essential cell biology*. Garland Science, 1998.
- [24] H. Gray. *Gray's anatomy: The anatomical basis of medicine and surgery*. Churchill-Livingstone, New York, 2004.
- [25] S. Eaton. Planar polarization of *Drosophila* and vertebrate epithelia. *Current Opinion in Cell Biology*, 9(6):860–866, 1997.



- [26] E. Rodriguez-Boulan and W. J. Nelson. Morphogenesis of the polarized epithelial-cell phenotype. *Science*, 245(4919):718–725, 1989.
- [27] W. J. Nelson. Epithelial cell polarity from the outside looking in. *News in Physiological Sciences*, 18:143–146, 2003.
- [28] T. Xia, M. Kovochich, J. Brant, M. Hotze, J. Sempf, T. Oberley, C. Sioutas, J. I. Yeh, M. R. Wiesner, and A. E. Nel. Comparison of the abilities of ambient and manufactured nanoparticles to induce cellular toxicity according to an oxidative stress paradigm. *Nano Lett.*, 6(8):1794–1807, 2006.
- [29] J. A. Zallen. Planar polarity and tissue morphogenesis. *Cell*, 129(6):1051–1063, 2007.
- [30] E. K. Vladar, D. Antic, and J. D. Axelrod. Planar cell polarity signaling: The developing cell’s compass. *Cold Spring Harbor Perspectives in Biology*, 1(3):–, 2009.
- [31] R. Farhadifar. *Dynamics of cell packing and polar order in developing epithelia*. PhD thesis, Technische Universität Dresden, 2009.
- [32] P. L. Townes and J. Holtfreter. Directed movements and selective adhesion of embryonic amphibian cells. *Journal of Experimental Zoology*, 128(1):53–120, 1955.
- [33] D’A.W. Thompson. *On growth and form*. Cambridge University Press, 1942.
- [34] R. A. Foty and M. S. Steinberg. The differential adhesion hypothesis: A direct evaluation. *Developmental Biology*, 278(1):255–263, 2005.
- [35] M. S. Steinberg. Reconstruction of tissues by dissociated cells. *Science*, 141(357):401–408, 1963.
- [36] D. Duguay, R. A. Foty, and M. S. Steinberg. Cadherin-mediated cell adhesion and tissue segregation: Qualitative and quantitative determinants. *Developmental Biology*, 253(2):309–323, 2003.
- [37] J. Käfer, T. Hayashi, A.F.M. Marée, R. W. Carthew, and F. Graner. Cell adhesion and cortex contractility determine cell patterning in the *Drosophila* retina. *Proc. Natl. Acad. Sci. U.S.A.*, 104(47):18549–18554, 2007.
- [38] T. Lecuit and P. F. Lenne. Cell surface mechanics and the control of cell shape, tissue patterns and morphogenesis. *Nat. Rev. Mol. Cell Biol.*, 8(8):633–644, 2007.
- [39] L. Hufnagel, A. A. Teleman, H. Rouault, S. M. Cohen, and B. I. Shraiman. On the mechanism of wing size determination in fly development. *Proc. Natl. Acad. Sci. U.S.A.*, 104(10):3835–3840, 2007.
- [40] R. Farhadifar, J. C. Roper, B. Algouy, S. Eaton, and F. Jülicher. The influence of cell mechanics, cell-cell interactions, and proliferation on epithelial packing. *Curr. Biol.*, 17(24):2095–2104, 2007.

- [41] S. Hilgenfeldt, S. Eriskin, and R. W. Carthew. Physical modeling of cell geometric order in an epithelial tissue. *Proc. Natl. Acad. Sci. U.S.A.*, 105(3):907–911, 2008.
- [42] M. Rauzi, P. Verant, T. Lecuit, and P. F. Lenne. Nature and anisotropy of cortical forces orienting *Drosophila* tissue morphogenesis. *Nat. Cell Biol.*, 10(12):1401–U57, 2008.
- [43] A. Piera Alberola and J. O. Rädler. The defined presentation of nanoparticles to cells and their surface controlled uptake. *Biomaterials*, 30(22):3766–3770, 2009.
- [44] K. von Gersdorff, N. N. Sanders, R. Vandenbroucke, S. C. De Smedt, E. Wagner, and M. Ogris. The internalization route resulting in successful gene expression depends on polyethylenimine both cell line and polyplex type. *Molecular Therapy*, 14(5):745–753, 2006.
- [45] A. P. Alivisatos. Nanocrystals: Building blocks for modern materials design. *Endeavour*, 21(2):56–60, 1997.
- [46] C. Buzea, I. I. Pacheco, and K. Robbie. Nanomaterials and nanoparticles: Sources and toxicity. *Biointerphases*, 2(4):Mr17–Mr71, 2007.
- [47] A. Nel, T. Xia, L. Madler, and N. Li. Toxic potential of materials at the nanolevel. *Science*, 311(5761):622–627, 2006.
- [48] V. L. Colvin. The potential environmental impact of engineered nanomaterials. *Nature Biotechnology*, 21(10):1166–1170, 2003.
- [49] T.C. Long, N. Saleh, R.D. Tilton, G.V. Lowry, and B. Veronesi. Titanium dioxide (p25) produces reactive oxygen species in immortalized brain microglia (bv2): Implications for nanoparticle neurotoxicity. *Environmental Science and Technology*, 40(14):4346–4351, 2006.
- [50] C.M. Sayes, A.M. Gobin, K.D. Ausman, J. Mendez, J.L. West, and V.L. Colvin. Nano-c60 cytotoxicity is due to lipid peroxidation. *Biomaterials*, 26:7587–7595, 2005.
- [51] A. M. Derfus, W. C. W. Chan, and S. N. Bhatia. Probing the cytotoxicity of semiconductor quantum dots. *Nano Lett.*, 4(1):11–18, 2004.
- [52] H. Dumortier, S. Lacotte, G. Pastorin, R. Marega, W. Wu, D. Bonifazi, J. P. Briand, M. Prato, S. Muller, and A. Bianco. Functionalized carbon nanotubes are non-cytotoxic and preserve the functionality of primary immune cells. *Nano Lett.*, 6(7):1522–1528, 2006.
- [53] E. E. Connor, J. Mwamuka, A. Gole, C. J. Murphy, and M. D. Wyatt. Gold nanoparticles are taken up by human cells but do not cause acute cytotoxicity. *Small*, 1(3):325–327, 2005.

- [54] C. M. Goodman, C. D. McCusker, T. Yilmaz, and V. M. Rotello. Toxicity of gold nanoparticles functionalized with cationic and anionic side chains. *Bioconjugate Chemistry*, 15(4):897–900, 2004.
- [55] M. Tsoli, H. Kuhn, W. Brandau, H. Esche, and G. Schmid. Cellular uptake and toxicity of au(55) clusters. *Small*, 1(8-9):841–844, 2005.
- [56] W. Jiang, B. Y. S. Kim, J. T. Rutka, and W. C. W. Chan. Nanoparticle-mediated cellular response is size-dependent. *Nature Nanotechnology*, 3(3):145–150, 2008.
- [57] B. D. Chithrani, A. A. Ghazani, and W. C. W. Chan. Determining the size and shape dependence of gold nanoparticle uptake into mammalian cells. *Nano Lett.*, 6(4):662–668, 2006.
- [58] H. J. Gao, W. D. Shi, and L. B. Freund. Mechanics of receptor-mediated endocytosis. *Proc. Natl. Acad. Sci. U.S.A.*, 102(27):9469–9474, 2005.
- [59] B. D. Chithrani and W. C. W. Chan. Elucidating the mechanism of cellular uptake and removal of protein-coated gold nanoparticles of different sizes and shapes. *Nano Lett.*, 7(6):1542–1550, 2007.
- [60] T. Cedervall, I. Lynch, S. Lindman, T. Berggard, E. Thulin, H. Nilsson, K. A. Dawson, and S. Linse. Understanding the nanoparticle-protein corona using methods to quantify exchange rates and affinities of proteins for nanoparticles. *Proc. Natl. Acad. Sci. U.S.A.*, 104(7):2050–2055, 2007.
- [61] SCENIHR. The appropriateness of existing methodologies to assess the potential risks associated with engineered and adventitious products of nanotechnologies, 2005.
- [62] I. Lynch, T. Cedervall, M. Lundqvist, C. Cabaleiro-Lago, S. Linse, and K. A. Dawson. The nanoparticle - protein complex as a biological entity; a complex fluids and surface science challenge for the 21st century. *Advances in Colloid and Interface Science*, 134-35:167–174, 2007.
- [63] D. B. Warheit. How meaningful are the results of nanotoxicity studies in the absence of adequate material characterization? *Toxicological Sciences*, 101(2):183–185, 2008.
- [64] T. Pellegrino, S. Kudera, T. Liedl, A. M. Javier, L. Manna, and W. J. Parak. On the development of colloidal nanoparticles towards multifunctional structures and their possible use for biological applications. *Small*, 1(1):48–63, 2005.
- [65] M. Nirmal, B. O. Dabbousi, M. G. Bawendi, J. J. Macklin, J. K. Trautman, T. D. Harris, and L. E. Brus. Fluorescence intermittency in single cadmium selenide nanocrystals. *Nature*, 383(6603):802–804, 1996.

- [66] K. A. Lidke, B. Rieger, T. M. Jovin, and R. Heintzmann. Superresolution by localization of quantum dots using blinking statistics. *Optics Express*, 13(18):7052–7062, 2005.
- [67] T. Dertinger, R. Colyer, G. Iyer, S. Weiss, and J. Enderlein. Fast, background-free, 3d superresolution optical fluctuation imaging (sofi). *Proc. Natl. Acad. Sci. U.S.A.*, in press, 2009.
- [68] J. M. Raser and E. K. O’Shea. Noise in gene expression: Origins, consequences, and control. *Science*, 309(5743):2010–2013, 2005.
- [69] J. Ziauddin and D. M. Sabatini. Microarrays of cells expressing defined cdnas. *Nature*, 411(6833):107–110, 2001.
- [70] A. Kumar and G. M. Whitesides. Features of gold having micrometer to centimeter dimensions can be formed through a combination of stamping with an elastomeric stamp and an alkanethiol ink followed by chemical etching. *Applied Physics Letters*, 63(14):2002–2004, 1993.
- [71] D. Falconnet, G. Csucs, H. M. Grandin, and M. Textor. Surface engineering approaches to micropattern surfaces for cell-based assays. *Biomaterials*, 27(16):3044–3063, 2006.
- [72] Andrew L. Hook, Helmut Thissen, and Nicolas H. Voelcker. Surface manipulation of biomolecules for cell microarray applications. *Trends Biotechnol.*, 24(10):471–477, 2006.
- [73] B. A. Langowski and K. E. Uhrich. Microscale plasma-initiated patterning ( $\mu$  pip). *Langmuir*, 21(23):10509–10514, 2005.
- [74] S. Hsieh, Y. A. Cheng, C. W. Hsieh, and Y. Liu. Plasma induced patterning of polydimethylsiloxane surfaces. *Mater. Sci. Eng. B*, 156(1-3):18–23, 2009.
- [75] M. Poujade, E. Grasland-Mongrain, A. Hertzog, J. Jouanneau, P. Chavrier, B. Ladoux, A. Buguin, and P. Silberzan. Collective migration of an epithelial monolayer in response to a model wound. *Proc. Natl. Acad. Sci. U.S.A.*, 104(41):15988–15993, 2007.
- [76] R. A. Desai, L. Gao, S. Raghavan, W. F. Liu, and C. S. Chen. Cell polarity triggered by cell-cell adhesion via e-cadherin. *J. Cell Sci.*, 122(7):905–911, 2009.
- [77] I. Dupin, E. Camand, and S. Etienne-Manneville. Classical cadherins control nucleus and centrosome position and cell polarity. *J. Cell Biol.*, 185(5):779–786, 2009.
- [78] M. Théry, V. Racine, M. Piel, A. Pepin, A. Dimitrov, Y. Chen, J. B. Sibarita, and M. Bornens. Anisotropy of cell adhesive microenvironment governs cell internal organization and orientation of polarity. *Proc. Natl. Acad. Sci. U.S.A.*, 103(52):19771–19776, 2006.

- [79] Antoine A. Khalil and Peter Friedl. Determinants of leader cells in collective cell migration. *Integrative Biology*, 2010.
- [80] H. W. Rand. Wound closure in actinian tentacles with to reference to the problem of organization. *Archiv für Entwicklungsmechanik der Organismen*, 41(1):159–214, 1915.
- [81] G. Fenteany, P. A. Janmey, and T. P. Stossel. Signaling pathways and cell mechanics involved in wound closure by epithelial cell sheets. *Curr. Biol.*, 10(14):831–838, 2000.
- [82] B. Ladoux. Cells guided on their journey. *Nat. Phys.*, 5(6):377–378, 2009.
- [83] R. Farooqui and G. Fenteany. Multiple rows of cells behind an epithelial wound edge extend cryptic lamellipodia to collectively drive cell-sheet movement. *J. Cell Sci.*, 118(1):51–63, 2005.
- [84] S. Huang, C. P. Brangwynne, K. K. Parker, and D. E. Ingber. Symmetry-breaking in mammalian cell cohort migration during tissue pattern formation: Role of random-walk persistence. *Cell Motility and the Cytoskeleton*, 61(4):201–213, 2005.
- [85] L. P. Cramer. Forming the cell rear first: Breaking cell symmetry to trigger directed cell migration. *Nat. Cell Biol.*, 12(7):628–632, 2010.
- [86] J. van der Gucht and C. Sykes. Physical model of cellular symmetry breaking. *Cold Spring Harbor Perspectives in Biology*, 1(1):–, 2009.
- [87] R. R. Kay, P. Langridge, D. Traynor, and O. Hoeller. Changing directions in the study of chemotaxis. *Nat. Rev. Mol. Cell Biol.*, 9(6):455–463, 2008.
- [88] S. R. Chowdhury, Y. Muneyuki, Y. Takezawa, M. Kino-oka, A. Saito, Y. Sawa, and M. Taya. Synergic stimulation of laminin and epidermal growth factor facilitates the myoblast growth through promoting migration. *Journal of Bioscience and Bioengineering*, 108(2):174–177, 2009.
- [89] L. Petitjean, M. Reffay, E. Grasland-Mongrain, M. Poujade, B. Ladoux, A. Buguin, and P. Silberzan. Velocity fields in a collectively migrating epithelium. *Biophys. J.*, 98(9):1790–1800, 2010.
- [90] E. R. Block, M. A. Tolino, J. S. Lozano, K. L. Lathrop, R. S. Sullenberger, A. R. Mazie, and J. K. Klarlund. Free edges in epithelial cell sheets stimulate epidermal growth factor receptor signaling. *Molecular Biology of the Cell*, 21(13):2172–2181, 2010.
- [91] J. Caddy, T. Wilanowski, C. Darido, S. Dworkin, S. B. Ting, Q. Zhao, G. Rank, A. Auden, S. Srivastava, T. A. Papenfuss, J. N. Murdoch, P. O. Humbert, N. Boulos, T. Weber, J. A. Zuo, J. M. Cunningham, and S. M. Jane. Epidermal wound repair is regulated by the planar cell polarity signaling pathway. *Developmental Cell*, 19(1):138–147, 2010.

- 
- [92] K. Amonlirdviman, N. A. Khare, D. R. P. Tree, W. S. Chen, J. D. Axelrod, and C. J. Tomlin. Mathematical modeling of planar cell polarity to understand domineering nonautonomy. *Science*, 307(5708):423–426, 2005.
- [93] M. E. Lidstrom and D. R. Meldrum. Life-on-a-chip. *Nature Reviews Microbiology*, 1(2):158–164, 2003.
- [94] K. Ino, M. Okochi, N. Konishi, M. Nakatochi, R. Imai, M. Shikida, A. Ito, and H. Honda. Cell culture arrays using magnetic force-based cell patterning for dynamic single cell analysis. *Lab on a Chip*, 8(1):134–142, 2008.
- [95] A. V. Kabanov, E. V. Batrakova, and V. Y. Alakhov. Pluronic block copolymers as novel polymer therapeutics for drug and gene delivery. *Abstracts of Papers of the American Chemical Society*, 223:U438–U438, 2002.
- [96] S. Lee and J. Voros. An aqueous-based surface modification of poly(dimethylsiloxane) with poly(ethylene glycol) to prevent biofouling. *Langmuir*, 21(25):11957–11962, 2005.
- [97] S. Lee and N. D. Spencer. Adsorption properties of poly(l-lysine)-graft-poly(ethylene glycol) (pll-g-peg) at a hydrophobic interface: Influence of tribological stress, ph, salt concentration, and polymer molecular weight. *Langmuir*, 24(17):9479–9488, 2008.
- [98] L. Andruzzi, B. Nickel, G. Schwake, J. O. Rädler, K. E. Sohn, T.E. Mates, and E. J. Kramer. Bio-selective surfaces by chemically amplified constructive microlithography. *Surf. Sci.*, 601:4984–4992, 2007.

Este trabajo no se habría podido realizar sin la colaboración de muchas personas que me han brindado su ayuda, sus conocimientos y su apoyo. Por ello

## muchas gracias

a mi director de tesis, Joachim O. Rädler, por brindarme esta estupenda oportunidad y sobre todo por su generosidad, su franqueza, constante apoyo e incontables ideas.

a Erwin Frey por su sinceridad, su llaneza y por supuesto por su insustituible contribución científica a este trabajo.

a Karen Alim por el valioso trabajo y la motivación invertidos, sin los cuales los “oligo-cellular arrays” no hubieran sido posibles.

a todos los Rädlers, por crear un ambiente de trabajo estupendo, las incontables comidas juntos, las muchas barbacoas y unas cuantas partidas de fútbol. Especialmente quiero dar las gracias a

Susi Kempter por compartir su experiencia en el laboratorio  
y ayudarme siempre que lo necesité.

Gerlinde por su valiosa ayuda y los buenos consejos en todo lo relacionado con células.

Susi Rappl por las horas pasadas en la “habitación limpia” y su eterna sonrisa.

Luisa Andruzzi por su excelente calidad tanto humana  
como científica, su apoyo y su amistad.

Felix por experimentos exitosos, tediosos análisis de datos  
y por su insustituible “mal humor”.

Peter por incontables experimentos y su inagotable dedicación,  
pero sobre todo por estar siempre de buen humor.

mis compañeras de despacho Verena, Van, Samira, Madeleine, Kirstin y Claudia  
por el buen ambiente en la oficina, animadas charlas y la paciencia mostrada  
ante mis constantes preguntas sobre ortografía y gramática alemana.

Tina por su amistad, su apoyo y muchas recetas.

a Jose, Magdalena y Almudena por la amistad y las risas compartidas.

a Naty y Esme por su amistad incondicional.

a mis padres sin los cuales yo no sería yo.

a Mari, Rodri, Oli y el enano por haber estado toda la vida a mi lado, por su amor incondicional, su amistad inquebrantable y por querer y aceptar todo lo bueno y lo malo que hay en mí.

a Carlota, Gonzi y Rodri por llenar mi vida de risas y enseñarme a ser niña otra vez.

a Xaver por quererme simplemente como soy y hacerme reír cada día.

y a mis chiquitujos por esperar pacientemente al otro lado del hilo rojo.

## Danke!





# Alicia Piera Alberola

geboren am 21. Oktober 1976 in Jerez de la Frontera

- |                 |   |
|-----------------|---|
| 01/2005-heute   | wissenschaftliche Angestellte im Exzellenzcluster<br>"Nanosystems Initiative Munich" an der Ludwig<br>Maximilians Universität München.  |
| 01/2005-03/2006 | Zulassungsarbeit zur Promotion zum Thema "Cytotoxicity<br>of nanocrystals" bei Prof. W. Parak am Lehrstuhl für<br>Angewandte Physik und Biophysik an der Ludwig<br>Maximilians Universität München. |
| 10/2003-06/2004 | Erasmus Studentin an der Ludwig Maximilians Universität München.  |
| 06/2004         | Licenciada en Física an der Universidad de Sevilla.   |